

INVESTIGATION OF NANOSTRUCTURED SURFACES FOR
THERMOPHOTOVOLTAIC APPLICATIONS

A THESIS SUBMITTED TO
THE GRADUATE SCHOOL OF NATURAL AND APPLIED SCIENCES
OF
MIDDLE EAST TECHNICAL UNIVERSITY

BY

ESLEM ENİS ATAĞ

IN PARTIAL FULFILLMENT OF THE REQUIREMENTS
FOR
THE DEGREE OF MASTER OF SCIENCE
IN
MECHANICAL ENGINEERING

SEPTEMBER 2021

Approval of the thesis:

**INVESTIGATION OF NANOSTRUCTURED SURFACES FOR
THERMOPHOTOVOLTAIC APPLICATIONS**

submitted by **ESLEM ENİS ATAK** in partial fulfillment of the requirements for the degree of **Master of Science in Mechanical Engineering, Middle East Technical University** by,

Prof. Dr. Halil Kalıpçılar
Dean, Graduate School of **Natural and Applied Sciences**

Prof. Dr. M. A. Sahir Arıkan
Head of Department, **Mechanical Engineering**

Prof. Dr. Derek K. Baker
Supervisor, **Mechanical Engineering, METU**

Prof. Dr. Tuba Okutucu Özyurt
Co-Supervisor, **Energy Institute, ITU**

Examining Committee Members:

Prof. Dr. Hakan I. Tarman
Mechanical Engineering, METU

Prof. Dr. Derek K. Baker
Mechanical Engineering, METU

Prof. Dr. Tuba Okutucu Özyurt
Energy Institute, ITU

Assoc. Prof. Dr. Özgür Bayer
Mechanical Engineering, METU

Asst. Prof. Dr. Elif Begüm Elçioğlu
Mechanical Engineering, Eskişehir Technical University

Date: 10.09.2021

I hereby declare that all information in this document has been obtained and presented in accordance with academic rules and ethical conduct. I also declare that, as required by these rules and conduct, I have fully cited and referenced all material and results that are not original to this work.

Name, Surname : Eslem Enis Atak

Signature:

ABSTRACT

INVESTIGATION OF NANOSTRUCTURED SURFACES FOR THERMOPHOTOVOLTAIC APPLICATIONS

Atak, Eslem Enis
Master of Science, Mechanical Engineering
Supervisor: Prof. Dr. Derek K. Baker
Co-Supervisor: Prof. Dr. Tuba Okutucu Özyurt

September 2021, 102 pages

Thermophotovoltaic (TPV) devices convert thermal radiation into electricity by using a thermal emitter and a photovoltaic (PV) cell. TPV systems can utilize variety of heat sources, which makes them suitable for harvesting waste heat. The downside of current TPV technology is its low efficiency due to the spectral mismatch between thermal emission of the emitter and the bandgap of the cell. In this thesis, the effect of nanostructures on radiative properties is studied in order to develop efficient TPV emitters and cells. Accordingly, metal-insulator-metal (MIM) nanostructured TPV emitters to match GaSb and Si cells were designed and optimized in order to achieve high power output and efficiency, by using finite-difference time-domain (FDTD) and particle swarm optimization (PSO) methods. In addition, nanostructured Si cells were developed to increase useful absorption without cell heating, by FDTD and parameter sweep methods. At 1700 K, W-SiO₂-W emitter showed an efficiency of 22.73% and power output of 3.622 W·cm⁻², which is 177% more efficient and produces 9.7% more power than SiC emitter paired with GaSb. At 2000 K, Ta-HfO₂-Ta emitter demonstrated an efficiency of 27.91% and power output of 4.755 W·cm⁻², which is 53.3% more efficient while producing 87.4% more power than Yb₂O₃ emitter paired with Si. In nanostructured Si cells, useful radiation increased by 30.4% while limiting thermalization increase to 24.4%, compared to flat Si cell, when illuminated by a blackbody at 2000 K. The results of this work are expected to shed a light onto the potential of developing high efficiency TPV systems.

Keywords: Thermophotovoltaics, Nanostructures, Metal-Insulator-Metal, Plasmon, Polariton

ÖZ

NANOYAPILI YÜZEYLERİN TERMOFOTOVOLTAİK UYGULAMALAR AÇISINDAN İNCELENMESİ

Atak, Eslem Enis
Yüksek Lisans, Makina Mühendisliği
Tez Yöneticisi: Prof. Dr. Derek K. Baker
Ortak Tez Yöneticisi: Prof. Dr. Tuba Okutucu Özyurt

Eylül 2021, 102 sayfa

Termofotovoltaik (TPV) cihazlar, bir ısı yayıcı ve fotovoltaik (PV) hücre sayesinde ısı ışınımı elektriğe dönüştürür. TPV sistemler, çeşitli ısı kaynaklarını kullanabildiği için atık ısının geri kazanımına uygundur. Mevcut TPV sistemlerin dezavantajı, yayıcının ısı ışınımı ve TPV hücrenin bant aralığı arasındaki uyumsuzluktan kaynaklanan yetersiz verimdir. Bu tezde, verimli TPV yayıcı ve hücreler geliştirmek amacıyla, nanoyapıların ışınımsal özelliklere etkisi incelenmiştir. Buna göre, GaSb ve Si hücrelerle eşleştğinde yüksek verim ve güç çıktısı oluşturması amacıyla, metal-yalıtkan-metal (MIM) nanoyapılı TPV yayıcılar, zamanda sonlu farklar yöntemi (FDTD) ve parçacık sürü optimizasyonu (PSO) kullanılarak tasarlanmış ve optimize edilmiştir. Ayrıca, FDTD ve parametre tarama yöntemleri kullanılarak, hücre ısınmasını artırmadan kullanışlı ışınımın soğurumunu artırma amacıyla nanoyapılı Si hücreler optimize edilmiştir. 1700 K'deki W-SiO₂-W yayıcının, GaSb hücreyle eşleştğinde %22,73 verim ve 3,622 W·cm⁻² güç çıktısı vereceği hesaplanmıştır. W-SiO₂-W yayıcı, SiC yayıcıya göre %177 daha verimli çalışırken %9,7 daha yüksek güç sağlamıştır. 2000 K'deki Ta-HfO₂-Ta yayıcının, Si hücreyle eşleştğinde %27,91 verim ve 4,755 W·cm⁻² güç çıktısı vereceği hesaplanmıştır. Ta-HfO₂-Ta yayıcı, Yb₂O₃ yayıcıya göre %53,3 daha verimli çalışırken %87,4 daha yüksek güç sağlamıştır. Ayrıca, 2000 K'de bir siyah cisim karşısında, nanoyapılı Si hücrede, kullanışlı ışınımın soğurulması düz Si hücreye göre 30,4% artarken, termalizasyon artışının %24,4'te tutulabileceği gösterilmiştir. Bu çalışmanın sonuçlarının, yüksek verimli TPV sistemlerin geliştirilmesine katkı sunması beklenmektedir.

Anahtar Kelimeler: Thermofotovoltaik, Nanoyapılar, Metal-Yalıtkan-Metal, Plazmon, Polariton

To my family

ACKNOWLEDGMENTS

I would like to express my sincere gratitude towards my advisors Prof. Dr. Derek K. Baker and Prof. Dr. Tuba Okutucu Özyurt for their support and guidance throughout this thesis. I would specifically like to thank Prof. Dr. Tuba Okutucu Özyurt for introducing me to the interesting world of nanoscience. Her knowledge, insight and encouragement were invaluable to the writing of this thesis. I would like to express my gratitude towards Asst. Prof. Dr. Elif Begüm Elçiođlu for providing insight and criticism in our countless discussion sessions. The financial support of TÜBİTAK under 2210-C National MSc/MA Scholarship Program in the Priority Fields in Science and Technology is greatly appreciated. Finally, I would like to thank my family for their endless support and encouragement.

TABLE OF CONTENTS

ABSTRACT	v
ÖZ	vii
ACKNOWLEDGMENTS	x
TABLE OF CONTENTS	xi
LIST OF TABLES	xiv
LIST OF FIGURES	xv
LIST OF ABBREVIATIONS	xviii
CHAPTERS	
1. INTRODUCTION	1
1.1. Motivation	1
1.2. Theoretical Background	2
1.2.1. Thermal Radiation.....	2
1.2.2. Maxwell's Equations.....	5
1.2.3. Optical Response of Materials	6
1.2.4. Permittivity Models.....	8
1.2.5. Quasiparticles	9
1.2.5.1. The Electron Hole.....	9
1.2.5.2. Phonons and Plasmons.....	10
1.2.5.3. Polaritons and Surface Waves	10
1.2.6. Thermophotovoltaics.....	12
1.2.7. Nanostructures.....	15
1.2.7.1. Short Wavelength Limit ($\Lambda \gg \lambda$)	15
1.2.7.2. Long Wavelength Limit ($\Lambda \ll \lambda$).....	15
1.2.7.3. Nanostructures with Size Comparable to Wavelength ($\Lambda \sim \lambda$)..	16

1.3.	Literature Review: Control of Radiative Properties by Nanostructures	16
1.3.1.	Nanostructured Surfaces.....	16
1.3.2.	Metal-Insulator-Metal Structures	21
1.4.	Objective and Outline of the Thesis	26
2.	METHODS.....	27
2.1.	Problem Statement.....	27
2.2.	The Finite-Difference Time-Domain (FDTD) Method	29
2.2.1.	ANSYS Lumerical	31
2.2.2.	Validation Studies	31
2.2.2.1.	Comparison with Analytical Calculations	32
2.2.2.2.	Comparison with Previous Numerical Studies	34
2.2.2.3.	Comparison with Previous Experimental Studies.....	36
2.3.	Derivative-free Optimization Methods.....	37
2.3.1.	Parameter Sweep	37
2.3.2.	Particle Swarm Optimization	38
2.4.	TPV Performance Evaluations	38
2.4.1.	In-band Radiation and Emitter Efficiency.....	39
2.4.2.	Maximum Theoretical Power Output and Efficiency	39
2.4.3.	Realistic Power Output and Efficiency	41
3.	DESIGN AND OPTIMIZATION OF METAL-INSULATOR-METAL SELECTIVE THERMOPHOTOVOLTAIC EMITTERS	45
3.1.	Design and Optimization of Tungsten-Silicon Dioxide-Tungsten (W-SiO ₂ - W) Emitter Matching GaSb Cell.....	46
3.1.1.	Material	46
3.1.2.	Method.....	47
3.1.3.	Optimization.....	50

3.1.4.	Results and Discussion.....	51
3.1.5.	Performance Evaluations	56
3.1.5.1.	High Temperature Adjustments on Emissivity.....	58
3.2.	Design and Optimization of Tantalum-Hafnia-Tantalum (Ta-HfO ₂ -Ta) Emitter Matching Silicon Cell	60
3.2.1.	Material	60
3.2.2.	Method	62
3.2.3.	Optimization.....	63
3.2.4.	Results and Discussion.....	64
3.2.5.	Performance Evaluations	66
4.	DESIGN AND OPTIMIZATION OF NANOSTRUCTURED SILICON THERMOPHOTOVOLTAIC CELLS.....	69
4.1.	Modeling of a Silicon Cell	71
4.2.	Optimization of Two-Dimensional Nanostructures	73
4.3.	Optimization of Three-Dimensional Nanostructures	77
4.4.	Performance Evaluations.....	79
5.	CONCLUSIONS AND FUTURE WORK.....	83
5.1.	Summary	83
5.2.	Conclusions	84
5.3.	Future Work	85
	REFERENCES.....	87
	APPENDICES	
A.	Optical Constants of Tungsten (W) at Elevated Temperatures.....	101
B.	Spectral Emissivity of Ytterbia (Yb ₂ O ₃)	102

LIST OF TABLES

TABLES

Table 2.1. The blackbody emissive power, in-band radiation, maximum power output, maximum blackbody efficiency and ideal emitter efficiency of a TPV system with 1700 K emitter paired with a GaSb cell	41
Table 2.2. The predicted and measured values of J_{sc} , V_{oc} and FF of UNSW silicon solar cell under AM1.5 solar spectrum	44
Table 3.1. Optimized nanostructure parameters and corresponding FOM values ...	52
Table 3.2. The emitter efficiency, TPV efficiency and power output for emitters at 1700 K paired with GaSb cells	56
Table 3.3. The efficiency and power output of the square W-SiO ₂ -W emitter of period 0.6 μm , constant emissivity vs emissivity adjusted to high temperatures.....	60
Table 3.4. Emitter efficiency, power output and TPV system efficiency of the MIM emitter, HfO ₂ coated MIM emitter, Yb ₂ O ₃ and ideal emitter.....	66
Table 3.5. Electrical power outputs from TPV systems with Si cells paired with selective emitters, Yb ₂ O ₃ and blackbody	68
Table 4.1. FOM values with varying height and width of triangular gratings	75
Table 4.2. FOM values with varying depth and width of v-groove gratings	75
Table 4.3. FOM values with varying height and width of rectangular gratings.....	75
Table 4.4. Optimum parameters of three simple gratings	76
Table 4.5. FOM values with varying pyramid height and width	78
Table 4.6. FOM values with varying square height and width	78
Table 4.7. Optimum parameters of the pyramid and square nanostructures	78
Table 4.8. Comparison of the absorbed radiation, useful radiation, and thermalization loss for Si cells matched with a blackbody emitter at 2000 K	80
Table A.1. The parameters used in Eq. (62) to estimate dielectric constants at elevated temperatures	101

LIST OF FIGURES

FIGURES

Figure 1.1. Spectral blackbody emissive power at different temperatures	4
Figure 1.2. Illustration of an electromagnetic wave [5]	5
Figure 1.3. Creation of an electron-hole pair	9
Figure 1.4. Propagation of SPPs	10
Figure 1.5. Dispersion relations of light and surface plasmons	11
Figure 1.6. The out-coupling of surface waves via gratings [10]	12
Figure 1.7. Schematic of a TPV System	13
Figure 1.8. Ideal spectral nature of the emitter and TPV cell.	14
Figure 2.1. (a) 2D nanostructures from Nguyen-Huu et al. [26] (b) 3D nanostructures from Arnold et al. [27]	27
Figure 2.2. Flowchart of the methodology	28
Figure 2.3. Yee lattice [52]	29
Figure 2.4. Lumerical FDTD layout with simulation components	31
Figure 2.5. Reflectivity of silicon at $\lambda = 0.5 \mu\text{m}$, analytical (exact) results vs. FDTD simulations with various mesh size.....	33
Figure 2.6. The reflectivity of silicon, analytical results and FDTD simulations....	33
Figure 2.7. The reflectivity spectra of Tantalum (Ta) and Tungsten (W), analytical results and FDTD simulations.....	34
Figure 2.8. The RCWA results of Sai [21] for flat Si is and nanostructured Si, compared to analytical and FDTD results.....	35
Figure 2.9. The emissivity spectrum of W-SiO ₂ -W emitter, FDTD results of Sakurai [46] and current FDTD simulation.....	35
Figure 2.10. (a) The schematic of absorber design by Han [42], with $d=300 \text{ nm}$, $a=500 \text{ nm}$, $h=100 \text{ nm}$, and $t=60\text{nm}$. (b) SEM image of the fabricated absorber	36
Figure 2.11. The spectral absorptivity of the emitter design by Han [42], measured values vs FDTD simulations.	36
Figure 2.12. Efficiency of a TPV system with GaSb cell and blackbody emitter ...	43
Figure 3.1. The EQE of JXC standard GaSb cell [70]	48

Figure 3.2. Four MIM designs and the computational area of a disk MIM structure.	49
Figure 3.3. The absorptivity at $\lambda=0.5 \mu\text{m}$ of metamaterial solar absorber design of Han [42], simulated again with FDTD with varying mesh sizes.	50
Figure 3.4. FOM vs generation number for disk resonator of period $0.4 \mu\text{m}$	52
Figure 3.5. The spectral emissivity of MIM emitters with periods $0.4\text{-}0.6 \mu\text{m}$. (a) Disk (b) Square (c) Cone and (d) Pyramid resonators.	54
Figure 3.6. Comparison of the emissivity spectra of MIM emitters with different shapes for periods (a) $0.4 \mu\text{m}$ (b) $0.6 \mu\text{m}$, and (c) $0.8 \mu\text{m}$	55
Figure 3.7. TPV system efficiencies for the MIM emitter, the ideal emitter and the blackbody emitter in the range $1000\text{-}1800 \text{K}$	57
Figure 3.8. The power outputs from TPV systems with the selective emitter and blackbody at different temperatures	58
Figure 3.9. The emissivity spectra of square $\text{W-SiO}_2\text{-W}$ emitter of period $0.6 \mu\text{m}$, at different temperatures.....	59
Figure 3.10. The schematic and design parameters of the proposed MIM emitter ..	62
Figure 3.11. External quantum efficiency of the UNSW c-Si cell.....	63
Figure 3.12. FOM vs generation number in PSO algorithm	64
Figure 3.13. Emissivity spectra of the plain Ta, Ta with 37nm HfO_2 coating and the MIM emitter	65
Figure 3.14. The schematic of coated MIM emitter, and the emissivity spectra of MIM emitter, coated MIM emitter and ideal emitter	66
Figure 3.15. Efficiency of TPV systems with Si cell paired with MIM emitters, Yb_2O_3 and blackbody.....	67
Figure 4.1. (a) Broadband low reflectivity (b) Narrowband low reflectivity.....	70
Figure 4.2. Reflection of light from a simple silicon cell.....	71
Figure 4.3. The reflectivity and absorptivity of $300 \mu\text{m}$ thick Si cell with Ag back reflector	72
Figure 4.4. 2D silicon nanostructures and a sample unit cell.....	74
Figure 4.5. Reflectivity of Si with three optimized gratings	76
Figure 4.6. Absorptivity spectra of nanostructured Si cells compared to flat Si.....	77
Figure 4.7. Unit cells of 3D Si nanostructures	77

Figure 4.8. Reflectivity spectra of optimized square and pyramid structures.....	79
Figure 4.9. Absorptivity of Si cells with square and pyramid structures.....	79
Figure B.1. Spectral emissivity of Yb ₂ O ₃ mantle	102

LIST OF ABBREVIATIONS

ABBREVIATIONS

AR	: Antireflective
EMT	: Effective medium theory
EQE	: External quantum efficiency
FDTD	: Finite-difference time-domain
FF	: Fill factor
FOM	: Figure of merit
IQE	: Internal quantum efficiency
MIM	: Metal-insulator-metal
MP	: Magnetic polariton
PML	: Perfectly matched layer
PSO	: Particle swarm optimization
PV	: Photovoltaic
RCWA	: Rigorous coupled-wave analysis
SEM	: Scanning electron microscopy
SP	: Surface plasmon
SPP	: Surface plasmon polariton
SPhP	: Surface phonon polariton
TE	: Transverse electric
TM	: Transverse magnetic
TPV	: Thermophotovoltaic
UNSW	: The University of New South Wales

LIST OF SYMBOLS

SYMBOLS

B	: Magnetic flux density (Wb m^{-2})
D	: Electric flux density (C m^{-2})
E	: Electric field intensity (V m^{-1})
E_g	: Bandgap energy (eV)
E_λ	: Spectral emissive power ($\text{W m}^{-2} \mu\text{m}^{-1}$)
E_{in}	: In-band radiation (W m^{-2})
E_{total}	: Total emissive power (W m^{-2})
H	: Magnetic field intensity (A m^{-1})
I	: Intensity of light
J	: Current density (A m^{-2})
J_0	: Reverse saturation current density (A cm^{-2})
J_{sc}	: Short circuit current density (A cm^{-2})
P_{el}	: Electrical power output (W cm^{-2})
S	: Poynting vector (W m^{-2})
T_E	: TPV emitter temperature (K)
T_C	: TPV cell temperature (K)
V_{oc}	: Open circuit voltage
c	: Speed of light in vacuum ($2.998 \times 10^8 \text{ m s}^{-1}$)
d	: Diameter or base width of the resonator (nm)
e	: Charge of an electron ($1.602 \times 10^{-19} \text{ C}$)
h	: Height of the resonator (nm), Planck's constant ($6.626 \times 10^{-34} \text{ m}^2 \text{ kg s}^{-1}$)
k	: Wave vector (m^{-1}), extinction coefficient

k_b : Boltzmann constant ($8.617 \times 10^{-5} \text{ eV K}^{-1}$)
 n : Refractive index, ideality factor
 t : Thickness of the dielectric layer (nm)
 x : Position of the particle
 v : Velocity of the particle, velocity of light in a medium
 w : Width of the nanostructure (nm)
 Λ : Period of the nanostructure (μm)
 α : Absorptivity, coefficient of thermal expansion
 β : Amendment factor
 γ : Damping coefficient
 ϵ : Relative permittivity
 ϵ_0 : Permittivity of vacuum ($8.854 \times 10^{-12} \text{ F m}^{-1}$)
 ε : Emissivity
 η_E : Emitter efficiency
 η_{TPV} : Thermophotovoltaic system efficiency
 λ : Wavelength of light (μm)
 λ_g : Wavelength corresponding to the bandgap energy of the cell (μm)
 μ : Relative permeability
 μ_0 : Permeability of vacuum ($1.257 \times 10^{-6} \text{ H m}^{-1}$)
 ν : Frequency, normalized open circuit voltage
 ρ_v : Volumetric charge density (C m^{-3})
 ρ : Reflectivity
 σ : Stefan-Boltzmann constant ($5.67 \times 10^{-8} \text{ W} \cdot \text{m}^{-2} \cdot \text{K}^{-4}$)
 τ : Transmissivity
 ω : Angular frequency (rad/s)

CHAPTER 1

INTRODUCTION

1.1. Motivation

The unlimited growth of energy needs in the world and the limited nature of fossil fuel sources direct researchers to look for alternative ways to convert energy. Photovoltaic (PV) and thermophotovoltaic (TPV) conversion systems are promising candidates in this manner. A classical PV (solar PV) system converts radiation emitted from the sun to electrical energy. Similarly, a TPV system converts thermal radiation into electrical energy by means of the photovoltaic effect. A simple TPV system has two essential components, a thermal emitter and a PV cell. When the emitter is heated by any external heat source, the irradiated photons excite the electrons in the PV cell and generates electrical current. A TPV system can utilize any heat source such as combustion, nuclear decay or the sun. This versatility of TPV systems makes them suitable for waste heat recovery. When combined with a solar absorber, a TPV system can be used to convert sunlight into electrical energy. The theoretical limit of solar to electricity efficiency of solar TPV systems exceeds Shockley-Queisser limit, i.e., the maximum efficiency of a classical solar PV system [1]. Unlike classical PV, a TPV system can utilize other heat sources in the absence of sunlight, e.g., combustion of biofuels. This paves the way of reliable renewable energy generation with low carbon emission. Contrary to other heat to electricity conversion systems, TPVs do not have moving parts, hence they do not make noise and require minimal maintenance.

The current use of TPV systems is limited due to the absence of highly efficient TPV systems. The biggest obstacle to creating efficient TPV systems is the mismatch between the emission of the thermal emitter and the bandgap energy of the cell. For TPV conversion to be efficient, the thermal emitter should only emit photons with

energies higher than the bandgap, and the cell should reflect low energy photons. One way to overcome this problem is employing optical filters, however additional layers between emitter and the receiver can absorb or scatter the radiation, which heats up the system. Additionally, finding materials that are both good optical filters and resistant to high temperatures is challenging. Another way of controlling the optical properties of the emitter or the cell is imprinting nanostructures on their surfaces. Optical properties such as emissivity and reflectivity can be tailored by adjusting the nanostructure parameters.

This thesis aims at designing and optimizing complex periodic nanostructures on TPV emitters and cells in order to overcome the spectral mismatch between the emitter and the cell. Development of TPV components with high performance and efficiency is an important step in the utilization of TPV systems in practical applications.

1.2. Theoretical Background

1.2.1. Thermal Radiation

All matter whose temperature is above the absolute zero dissipates heat via radiation. The mechanism behind this phenomenon is well-known. When matter is heated, the charges inside start to oscillate. These oscillations create electromagnetic radiation that propagates towards all directions. This emission of radiation due to the finite temperature of materials is called thermal radiation. Unlike the other two modes of heat transfer, i.e., conduction and convection, radiation does not need any medium to propagate.

The rate at which radiative power is emitted per unit area of the emitting surface, the emissive power, is determined by the Stefan-Boltzmann law [2]:

$$E = \varepsilon\sigma T^4 \quad (1)$$

In Eq. (1), T is the temperature in K, σ is the Stefan-Boltzmann constant, and ε is the emissivity, which is a real number between 0 and 1. Emissivity is a measure of how efficiently a body emits thermal radiation. If $\varepsilon = 1$, the material is termed as blackbody. A blackbody is a perfect absorber and emitter of radiation. Despite its name, a blackbody is not actually black. In fact, it is glowing, as it emits radiation at

all wavelengths. The intensity of thermal radiation depends on the wavelength. Based on classical thermodynamics, Wilhelm Wien derived an expression for blackbody emissive power as a function of wavelength and temperature (spectral emissive power) in the form [3]:

$$E_{\lambda,b}(\lambda T) = \frac{f(\lambda T)}{\lambda^5} \quad (2)$$

Wien also discovered that, the spectral emissive power is maximum at a certain wavelength, which is known as Wien's displacement law;

$$\lambda_{max} = \frac{2898 \mu m K}{T} \quad (3)$$

Based on classical electrodynamics, Rayleigh, together with his colleague Jeans, developed an expression for the blackbody distribution which is known as the Rayleigh-Jeans distribution [4]:

$$E_{\lambda,b}(\lambda, T) = \frac{2\pi c k_b T}{\lambda^4} \quad (4)$$

In Eq. (4), c is the speed of light and k_b is Boltzmann constant. Eq. (4) gives the radiation intensity, at a given temperature and wavelength, integrated over all solid angles. Rayleigh-Jeans approximation fits experimental data at very long wavelengths; however, it does not hold for all wavelengths because radiative power approaches infinity as the wavelength approaches zero. The failure of Rayleigh-Jeans distribution at high energies is called the ultraviolet catastrophe. In 1900, Max Planck developed an equation which fits experimental data at all wavelengths. In his formulation, Planck introduced an idea that was not present in classical physics; the quanta of light. Planck assumed, the absorption and emission of radiation at a given frequency could only occur as an integer multiple of the energy quanta, $h\nu$, where h is Planck's constant and ν is the frequency. The spectral distribution of blackbody radiation is successfully described by Planck's law [2]:

$$E_{\lambda,b}(\lambda, T) = \frac{C_1}{\lambda^5 [\exp(C_2/\lambda T) - 1]} \quad (5)$$

In Eq. (5), $C_1 = 3.742 \times 10^8 \text{ W}\cdot\mu\text{m}^4\cdot\text{m}^{-2}$ and $C_2 = 1.439 \times 10^4 \text{ W}\cdot\mu\text{m}\cdot\text{K}$. The total emissive power of a blackbody can be determined by integrating this equation over

all wavelengths. Planck's blackbody distribution at 1000 K - 5000 K range is given in Figure 1.1.

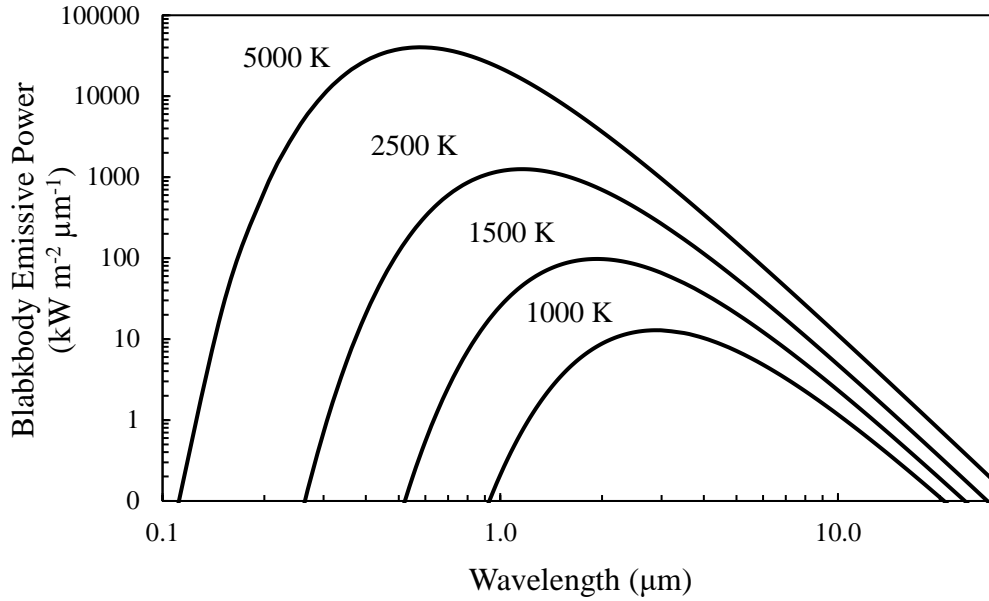


Figure 1.1. Spectral blackbody emissive power at different temperatures

For real materials the emissivity is not unity, hence they radiate less than an ideal blackbody. The emissivity of a surface depends on the material, temperature, surface conditions, the wavelength and direction of the radiation being emitted. When the emissivity is independent of the emission angle, the material is called a *diffuse emitter*. If the emissivity of a surface does not depend on the wavelength, it is called a *gray surface* or a *graybody emitter*.

For most engineering applications, surface properties are defined as directional averages. Therefore, a spectral, hemispherical emissivity is given as [2]:

$$\varepsilon_{\lambda}(\lambda, T) = \frac{E_{\lambda}(\lambda, T)}{E_{\lambda,b}(\lambda, T)} \quad (6)$$

When radiation is incident on a semitransparent medium, portions of this radiation are reflected, absorbed, or transmitted. The fraction of the incident radiation that is reflected by the surface is called *reflectivity*. Similarly, the terms *absorptivity* and *transmissivity* refer to the fractions of absorbed and transmitted radiation,

respectively. For radiation balance, the spectral absorptivity, reflectivity and transmissivity should sum up to unity.

$$\alpha_\lambda + \rho_\lambda + \tau_\lambda = 1 \quad (7)$$

When isothermal conditions exist, the emissivity and absorptivity should be equal for all wavelengths due to Kirchoff's law:

$$\varepsilon_\lambda = \alpha_\lambda \quad (8)$$

Then, the spectral emissivity of a surface can be calculated by:

$$\varepsilon_\lambda = 1 - \rho_\lambda - \tau_\lambda \quad (9)$$

1.2.2. Maxwell's Equations

Thermal radiation is an electromagnetic wave which is composed of oscillating perpendicular electric (\mathbf{E}) and magnetic field (\mathbf{B}) components. A representation of an electromagnetic wave is shown in Figure 1.2.

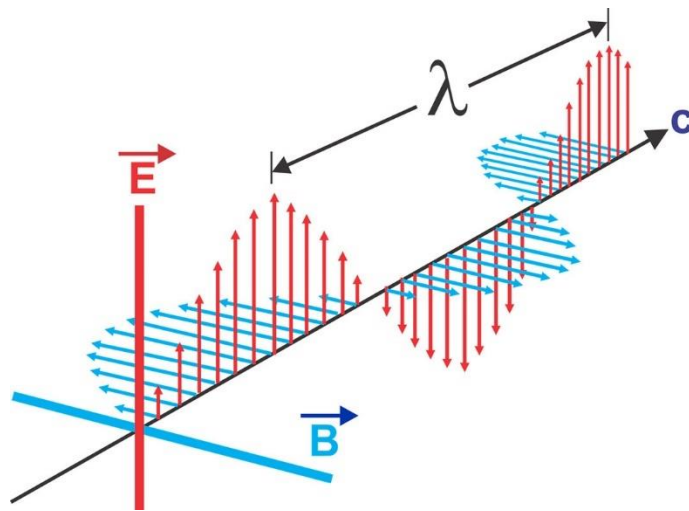


Figure 1.2. Illustration of an electromagnetic wave [5]

The propagation of electromagnetic waves is governed by Maxwell's equations. The differential form of macroscopic Maxwell's equations [6] is given through Eqs. (10 a-d).

$$\nabla \times \mathbf{E} = -\frac{\partial \mathbf{B}}{\partial t} \quad (10a)$$

$$\nabla \times \mathbf{H} = \mathbf{J} + \frac{\partial \mathbf{D}}{\partial t} \quad (10b)$$

$$\nabla \cdot \mathbf{D} = \rho_e \quad (10c)$$

$$\nabla \cdot \mathbf{B} = 0 \quad (10d)$$

In Eqs. (10 a-d), \mathbf{E} is the electric field, \mathbf{H} is the magnetic field, \mathbf{J} is current density, \mathbf{D} is the electric displacement, \mathbf{B} is the magnetic flux density, and ρ_e is the volumetric charge density. For linear and isotropic materials \mathbf{D} and \mathbf{B} are related to \mathbf{E} and \mathbf{H} through following constitutive equations [7]:

$$\mathbf{D} = \epsilon \mathbf{E} = \epsilon_r \epsilon_0 \mathbf{E} \quad (11a)$$

$$\mathbf{B} = \mu \mathbf{H} = \mu_r \mu_0 \mathbf{H} \quad (11b)$$

where μ_r is the relative magnetic permeability and ϵ_r is the dielectric constant. For nonmagnetic materials, μ_r is unity. Eq. (10a) is known as the Faraday's law of induction, which states that a change in the magnetic field, creates a circulating electric current. Eq. (10b) is Ampere's law which states that a change in the electric field or an electric current produces a magnetic field. Because the displacement current density term ($\partial \mathbf{D} / \partial t$) is added by Maxwell, it's also called the Ampere-Maxwell law. Eq. (10c) is Gauss' law which indicates that the flux of an electric field out of any closed surface is proportional to the electric charge enclosed by the surface. Eq. (10d) states the flux of magnetic field out of any closed surface is zero. This is because magnetic fields always exist as dipoles. For example, a bar magnet has two poles, north and south. Splitting a magnet in half creates additional poles, so each piece retains exactly two poles. This process can be repeated all the way to an electron, which itself has a dipole characteristic. Although magnetic monopoles have yet to be found, their existence would require all the electric charges in the universe to be quantized. Interestingly, the electric charge is already known to be quantized.

1.2.3. Optical Response of Materials

Electromagnetic radiation interacts with matter in various ways. A thin layer of glass transmits almost all of the visible light whereas a mirror reflects it. A sheet of paper also reflects light, but cannot be used as a mirror. When light is incident on a surface,

three processes can happen; reflection, transmission, and absorption. The amounts of reflected, transmitted or absorbed radiation depends on the energy of the light and the properties of the material. While light travels at a constant speed of 2.998×10^8 m/s in vacuum, it slows down when it propagates in a material. The ratio of free space velocity of light to the speed of light in the medium is called the *refractive index*, which is defined by:

$$n = \frac{c}{v} \quad (12)$$

If the media is absorbing, the intensity of propagating light decreases exponentially with the propagation depth. The intensity of transmitted light in an optical medium can be found by Beer-Lamber law [8]:

$$I(z) = I_0 e^{-\frac{4\pi k}{\lambda} z} \quad (13)$$

Where z denotes the position of the wavefront, I_0 is the intensity of light at $z = 0$, and k is the extinction coefficient of the material. The coefficients n and k , together form the complex refractive index of a material:

$$\tilde{n} = n + ik \quad (14)$$

When light is reflected at the interface between two materials, the reflectivity depends on complex refractive index of both materials. At normal incidence, the reflectivity can be found by Fresnel's law [8]:

$$\rho = \left| \frac{\tilde{n}_1 - \tilde{n}_2}{\tilde{n}_1 + \tilde{n}_2} \right|^2 \quad (15)$$

The refractive index of a medium is related to its relative permittivity through the relation:

$$\tilde{n}^2 = \tilde{\epsilon}_r^2 \quad (16)$$

The relative permittivity ($\tilde{\epsilon}_r$) quantizes electric polarizability of a material which is also called the *dielectric constant*. The complex dielectric constant is defined by:

$$\tilde{\epsilon}_r = \epsilon_1 + i\epsilon_2 \quad (17)$$

The mathematical models that describe the dispersive (frequency-dependent) response of materials to light, are usually developed to calculate $\tilde{\epsilon}_r$ rather than \tilde{n} . These models are used to calculate the optical constants n and k with the relation given in Eq. (17).

1.2.4. Permittivity Models

In classical electromagnetics, the dispersive optical characteristics of materials are explained by the dipole-oscillator model. The dipole-oscillator model assumes there are different kinds of oscillators in a medium with different resonant frequencies.

One such model is the Lorentz model, which explains the relative permittivity of dielectrics. In Lorentz model, atoms are considered to exist as dipoles with bound charges. The positive and negative charges are attached to each other by restoring forces, which act like springs. The displacement x of the electron is governed by a differential equation of the form:

$$m_0 \frac{d^2 x}{dt^2} + m_0 \gamma \frac{dx}{dt} + m_0 \omega_0^2 x = -eE \quad (18)$$

where e is the charge of an electron, E is the electric field strength, and γ is the damping coefficient. The frequency dependence of the relative permittivity for a dielectric can be described by [8]:

$$\epsilon_r(\omega) = \epsilon_\infty + \frac{Ne^2}{\epsilon_0 m_0} \frac{1}{(\omega_0^2 - \omega^2 - i\gamma\omega)} \quad (19)$$

where, ϵ_∞ and is the dielectric constant at high-frequencies, N is the number of atoms per unit volume, and ω is the angular frequency.

In metals, the electrons are not bound to nucleus unlike dielectrics. The permittivity of metals can be found by assuming zero spring force in the Lorentz model. The free electron model of metals is called the Drude-Lorentz or simply the Drude model. This model successfully explains why metals are good conductors of electricity and good reflectors of light. The Drude model is given in Eq. (20).

$$\epsilon_r(\omega) = 1 - \frac{\omega_p^2}{\omega^2 + i\gamma\omega} \quad (20)$$

In Eq. (20), ω_p is the plasma frequency which is defined as:

$$\omega_p = \left(\frac{Ne^2}{\epsilon_0 m_0} \right)^{1/2} \quad (21)$$

For a lightly damped system, the equation reduces to:

$$\epsilon_r(\omega) = 1 - \frac{\omega_p^2}{\omega^2} \quad (22)$$

It can be noticed that when the frequency (ω) is below the resonant frequency (ω_p), the dielectric function becomes negative which makes the complex refractive index (\tilde{n}) purely imaginary. When one uses Eq. (22) to calculate the reflection on the air-metal boundary for frequencies $\omega < \omega_p$, the reflectivity is found to be 100 %. This is consistent with the fact that metals are highly reflective above certain frequencies. However, this model is inadequate to explain why some metals (e.g., copper, gold) are colored, because it requires knowledge of band structure of these materials.

1.2.5. Quasiparticles

Quasiparticles are collective excitations or disturbances that behave as particles. Quasiparticles are emergent phenomena and they do not constitute matter on their own unlike the fundamental particles. However, they can have characteristics of fundamental particles such as charge or spin.

1.2.5.1. The Electron Hole

In semiconductors, when an electron absorbs a photon with enough energy, it jumps from valence band to the conduction band. This results in a vacancy in the valence band, which is known as an electron hole, or simply a “hole”. When a surrounding electron jumps into this vacancy, it leaves another hole in its old place, moving the location of the hole. Repeating the same process, the hole can effectively wander around in the band. The movement of the hole can be modeled as a free particle with a positive charge moving in a sea of bound electrons. Treating the electron hole as a real particle, even though it is not one, simplifies the calculations to a great extent.

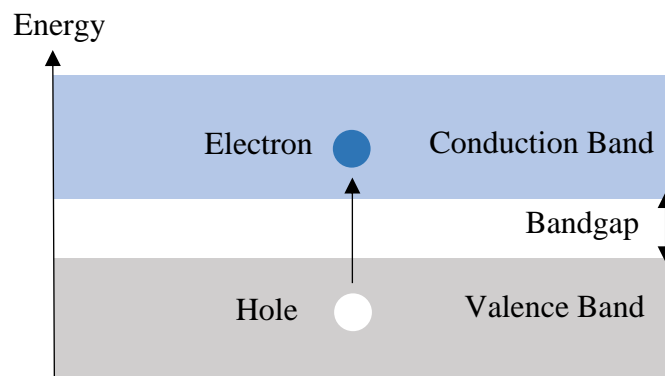


Figure 1.3. Creation of an electron-hole pair

1.2.5.2. Phonons and Plasmons

Quantization of electromagnetic waves explains phenomena including blackbody radiation and photoelectric effect, which cannot be fully explained by classical physics. In fact, this quantization is applicable to other types of waves as well. In solids, the quantization of lattice vibrations give rise to phonons. Similarly, the collective oscillations of electrons in metals are called plasmons. Plasmons near the surface of the metal can oscillate along the metal-dielectric interface. These are called surface plasmons (SP), which are usually formed in visible or near-infrared region in highly conductive metals.

1.2.5.3. Polaritons and Surface Waves

In some conditions, photons can strongly couple with other particles and behave like a new particle. These quasiparticles are called polaritons. For example, in polar dielectrics, the coupling of bound charges with the electromagnetic waves gives rise to surface phonon polaritons (SPhP) which occurs in the mid-infrared region. Photons can couple with oscillating electrons, as well. When photons couple with plasmons on the surface of a metal, they create surface plasmon polaritons (SPP). SPPs propagate along the metal-dielectric interface as shown in Figure 1.4. The field intensity exponentially decreases inside both media. Since SPPs only propagate along the surface, they constitute electromagnetic surface waves.

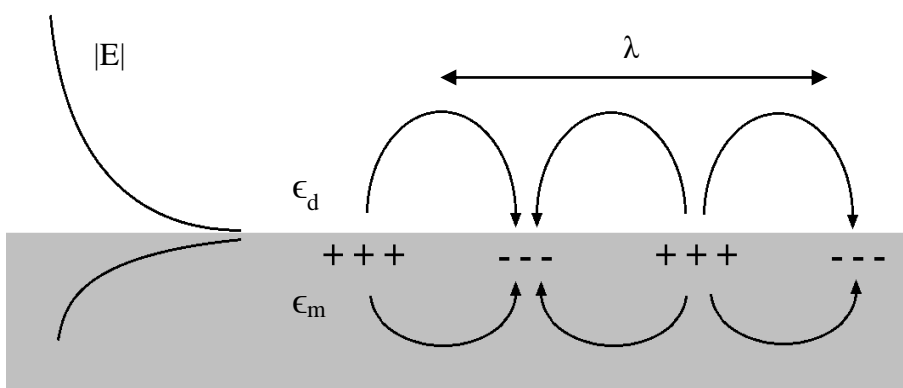


Figure 1.4. Propagation of SPPs

The dispersion relation between the surface plasmons and the light can be expressed in Figure 1.5, where the red line represents the light propagating in air, and black line shows the dispersion of SP. In Figure 1.5, k is the wave number in the x -direction which represents the momentum and ω is the angular frequency.

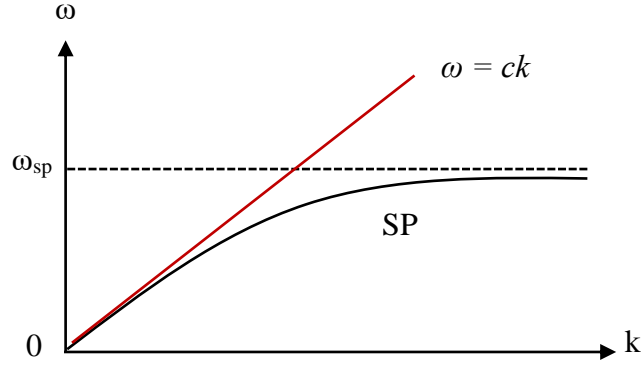


Figure 1.5. Dispersion relations of light and surface plasmons

The SP line asymptotically approaches to the surface plasmon frequency ω_{sp} that is given by:

$$\omega_{sp} = \frac{\omega_p}{\sqrt{1 + \epsilon_d}} \quad (23)$$

At frequencies below ω_{sp} , the light line approaches to the SP line, however its momentum is always smaller than the momentum of SP. In order to interact with the plasmons, photons need additional momentum. One way to acquire this momentum is using periodic gratings on the surface of the metal. The momentum of light incident on a grating configuration can be found by the Bloch-Floquet condition [6]:

$$k_{x,j} = k_x + 2\pi j / \Lambda \quad (24)$$

In Eq. (24), j represents the diffraction order and Λ is the periodicity of the grating. Eq. (24) predicts the SPP resonance to be correlated with the grating period. This relation is also confirmed by studying the absorption peaks in nanostructured metallic surfaces [9].

Another type of plasmon polariton is the magnetic polariton (MP). MP is the coupling of incident electromagnetic radiation to the magnetic excitation inside nanostructures.

MPs can be excited between two metallic strips. When a MP is excited, there exists a strongly confined magnetic field which is accompanied by a circulating electric current. Unlike SPPs, MPs are insensitive to the period of the structure and the angle of incidence of light.

In a radiating medium, gratings can be used to extract surface waves. Figure 1.6 represents the out-coupling of thermally generated surface waves to free space via grating structure [10]. In the far-field regime, the outcoupled radiation is ultimately bounded by the blackbody limit due to increase in the total area. However, surface gratings can be used to manipulate and tune the spectral and directional emissivity of surfaces.

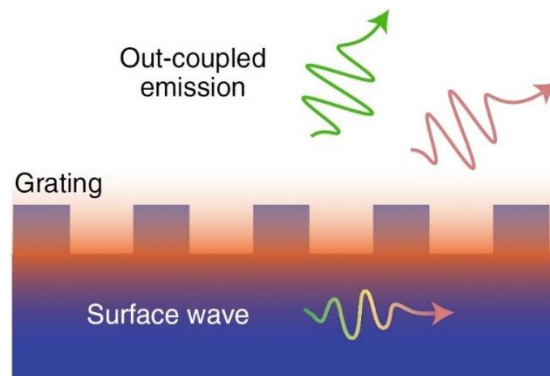


Figure 1.6. The out-coupling of surface waves via gratings [10]

1.2.6. Thermophotovoltaics

Thermophotovoltaic (TPV) energy conversion is a process that converts thermal radiation into electricity. A TPV system consists of two main parts; a thermal emitter and a receiver (PV cell). In the context of the TPV systems, the PV cell can also be named a TPV cell. A schematic of a simple TPV system is shown in Figure 1.7. In addition to the emitter and the cell, TPV devices may include optical filters, antireflective (AR) coatings, and a heat sink to cool down the cell.

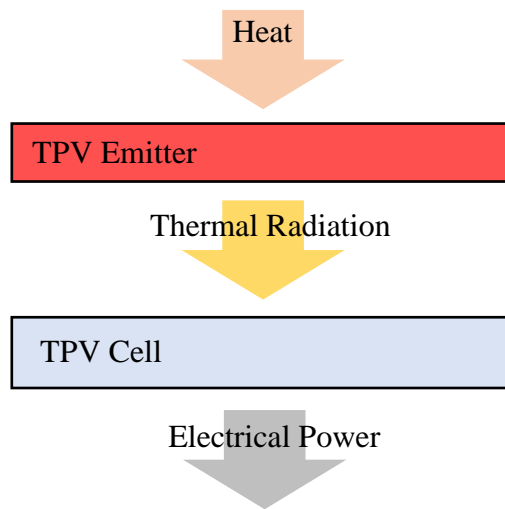


Figure 1.7. Schematic of a TPV System

When the emitter is heated by an external heat source, it begins to radiate photons, which is directed to the receiver. If the energy of photons is higher than the bandgap energy (E_g) of the cell, electron-hole pairs can be created to produce electric current. The first demonstration of TPV effect was performed by physicist Henry Kolm at Massachusetts Institute of Technology (MIT) in 1956 [11]. In Kolm's experiment, a silicon solar cell, which was just being developed, was placed next to a Coleman Lantern (a type of gas lamp). The electrical power output was measured and the results were presented in a Lincoln Laboratory progress report. For an efficient TPV conversion, the photons reaching the PV cell should have greater energy than the bandgap. These photons are called *in-band* photons. In the early stages of TPV research, mostly silicon cells were employed. Silicon has an E_g of 1.1 eV [8], which corresponds to photon energy with the wavelength of 1.1 μm . According to Wien's law, for an emitter to have a peak emission at this wavelength, it should be heated up to 2630 K, which possesses a challenge to practicality. In 1980's, the development of low bandgap TPV cell materials such as gallium antimonide (GaSb, $E_g = 0.72$ eV [12]) resurged the interest in TPV systems.

The biggest obstacle to creating efficient TPV systems is the mismatch between the emission spectrum of the TPV emitter and the bandgap of the PV cell. In an ideal TPV system, the emitter only emits *in-band* photons ($E > E_g, \lambda < \lambda_g$) and the receiver

should reflect all the out-of-band photons. This ideal two band model can be expressed in terms of the emissivity of the emitter (ε_E) and the reflectivity of the TPV cell (ρ_c) as:

$$\varepsilon_E = 1 \text{ or } \rho_c = 0, \quad 0 < \lambda \leq \lambda_g \quad (25a)$$

$$\varepsilon_E = 0 \text{ or } \rho_c = 1, \quad \lambda_g < \lambda < \infty \quad (25b)$$

The ideal spectral nature of the TPV emitter and cell are presented in Figure 1.8.

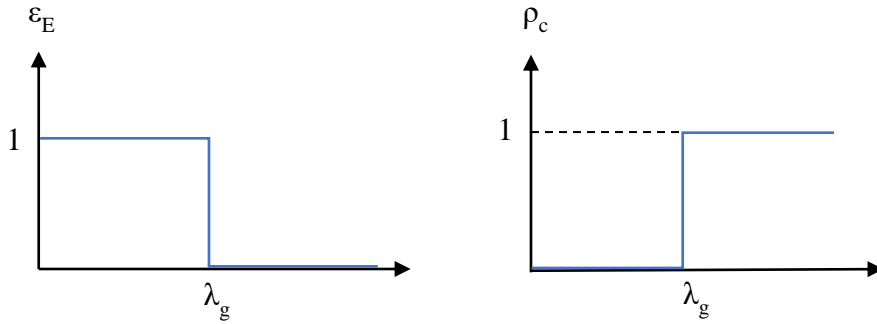


Figure 1.8. Ideal spectral nature of the emitter and TPV cell.

The efficiency of a TPV system can be determined by dividing the electrical power to the radiation incident on a TPV cell. In the case of a “perfect” cell, Chubb [11] estimates the maximum attainable efficiency for a TPV system with a GaSb cell at 1700 K as 20%, for constant emissivity and absorptivity. At the same temperature, for an ideal system described as in Eq. (25), an efficiency of 78% calculated [11]. This shows that by optimizing the spectral distribution of the radiation, the efficiency of TPV systems can be greatly improved. The control of wavelength dependance of optical characteristics is referred to as *spectral control*. One way to achieve spectral control is employing optical filters. Optical filters are used to reduce the reflectivity at specific wavelengths by exploiting the destructive interference [13]. In order to achieve broadband reflection reduction, multilayer coatings can be used, however, any additional layer between the emitter and the receiver can absorb and scatter radiation, which leads to heating and loss of efficiency. Finding coating materials with matching thermal expansion coefficients and high thermal stability also limits the use of filters in TPV applications. Another way of spectral control is patterning the surface of the emitter and/or the receiver. By imprinting nanostructures on a

surface, the optical properties of the material can be greatly altered. The next section gives a more detailed description on nanostructures and the current status of the spectral control based on surface nanostructures.

1.2.7. Nanostructures

Micro and nano structures on the surface are known to affect the optical response of the material. It is known that the reflectivity and emissivity depend on the surface roughness. It also has been known that the gratings on a metallic surface can significantly reduce reflectivity at certain wavelengths, which is known as the Wood's anomaly [6]. Today, surface texturing is used to reduce reflection in numerous applications including optical lenses, solar cells, and spectroscopy. Due to Kirchhoff's law, altering the reflectivity of a surface also changes its absorptivity and emissivity. The method of analysis to determine the optical response of micro and nano surface structures depends on their characteristic size. The micro and nano surface structures can be classified according to the relation between their dimensions and the wavelength of light that is considered.

1.2.7.1. Short Wavelength Limit ($\Lambda \gg \lambda$)

If the period of nanostructures is much larger than the wavelength of the incident light, the light can be treated as beams. This condition is referred as the short wavelength limit [14]. In this type of texturing, incident light undergoes consecutive reflections before escaping the surface. The intensity of total reflected light can be calculated by geometric optics methods like ray tracing. The resultant reflectivity is determined by dividing the total reflected intensity to the incident light intensity. In the literature, the ray tracing method was employed to calculate the reflectivity from textured silicon surfaces [15, 16].

1.2.7.2. Long Wavelength Limit ($\Lambda \ll \lambda$)

When the texturing period is much smaller than the wavelength of light, the light fails to "sense" the nanostructures. This is called the long wavelength limit [14]. In this case, the material acts as an isotropic material with an effective refractive index. The new refractive index can be calculated by means of the *effective medium theory*

(EMT), where an effective dielectric constant is calculated based on the *filling fraction* defined as the ratio of the area occupied by the grating to that of the unit cell. These small nanostructures act like a gradient refractive index film which minimizes the reflection.

1.2.7.3. Nanostructures with Size Comparable to Wavelength ($\Lambda \sim \lambda$)

If characteristic size of the nanostructures is comparable to the wavelength of the incident light, diffraction occurs. *Diffraction* is the scattering of light when it encounters an aperture or an obstacle. In this case, neither ray tracing nor EMT approximations are valid, hence solving Maxwell's equations are necessary to analyze their interaction with light. Throughout this thesis, the term nanostructures will be used to refer to this case. Analytical solutions to Maxwell's equations for complex geometries are difficult to obtain if not impossible. For this reason, numerical methods such as rigorous coupled-wave analysis (RCWA) or finite-difference time-domain (FDTD) are employed.

1.3. Literature Review: Control of Radiative Properties by Nanostructures

Metamaterials are artificially made structures that display optical properties that do not exist in naturally occurring materials. Developments in nano imprinting technologies made it possible to fabricate metamaterials with nanometer precision. The review section is divided into two parts, nanostructured surfaces, which consists of a nanopatterned surfaces with or without coating, and Metal-Insulator-Metal (MIM) structures. MIM structures are relatively new type of metamaterials that consist of a metal base (reflector), dielectric thin film, and metallic nano patches (resonators). MIMs are capable of exciting both SPP and MP resonances, which can be used to create tunable high absorptivity/emissivity in a broadband region. In the recent years, MIMs attracted attention due to their potential for developing selective TPV emitters.

1.3.1. Nanostructured Surfaces

Heinzel [17] fabricated periodic nanostructures on a tungsten (W) surface in order to reduce the mismatch between the emission spectrum of the TPV emitter and the

spectral sensitivity of the PV cell. The nanostructures consisted of disks with period of 1.4 μm and grating depth of 0.18 μm . At 1200 K, the maximum emissivity of 70% was measured at the wavelength of 1.6 μm at polar angle of 0° , by Fourier transform (FT) spectrometers. The location of emissivity peak was consistent with the RCWA calculation. The mechanism behind the emissivity peak was attributed to thermal excitation of surface plasmons by periodic nanostructures.

Sai [18] fabricated reverse-pyramid cavities on Si surface with structural periods of 1.5 and 2.0 μm in order to develop selective emitters for TPV systems. The nanostructured Si surfaces were coated with a thin layer of platinum (Pt) to enhance the effect of microstructures. Emissivity peaks at 1.7 and 2.2 μm were measured for periods of 1.5 and 2.0 μm , respectively. Selective emission efficiencies were calculated by matching the $\lambda = 1.5 \mu\text{m}$ emitter with GaSb and $\lambda = 2 \mu\text{m}$ emitter with InGaAsSb cells. The sensitive region of GaSb and InGaAsSb were taken as 0-1.7 μm and 0-2.3 μm , respectively. Between 1000-1800 K emitter temperatures, the efficiency of $\lambda = 2 \mu\text{m}$ emitter was calculated to be 16-20% higher than a graybody emitter with $\varepsilon = 0.9$. The efficiency of $\lambda = 1.5 \mu\text{m}$ emitter was also 5-14% higher than that of a graybody.

Sai [19] fabricated two-dimensional gratings with a periodicity of 1 μm and wall thickness of 200 nm, on single and polycrystalline W surfaces to obtain selective TPV emitters. A peak emissivity at 1.25 μm was obtained, which falls within the sensitive range of GaSb cells (0.8-1.8 μm). After heating up to 1400 K, the single crystalline grating was highly stable, but the polycrystalline grating was deformed due to the grain growth.

Sai [20] fabricated rectangular surface-relief gratings with a period of 1.0–1.2 μm on single crystalline W substrates to develop spectrally selective emitters for TPV applications. Fabricated emitters showed emission peaks at 1.22 μm , 1.48 μm and 1.56 μm wavelengths, respectively. The emissivity enhancement was attributed to the microcavity effect. Power generation tests were carried out with an InGaAs photodiode whose sensitive region is 0.9–1.7 μm . It was observed that the selective emission efficiency of W gratings was more than two times higher compared to a SiC emitter.

Sai [21] showed that the reflectivity of a Si surface can be reduced below 1% by fabricating subwavelength nanopylamids. In RCWA simulations, the period and the base length of the pyramid were set to be 100 nm and height of the pyramids were varied between 100-400 nm. Pyramids with the height of 400 nm were fabricated on Si wafers. The mean reflectivity between wavelengths 300-1000 nm was measured as 0.8%. After annealing at 800°C and 1000°C, the average reflectivity increased to 3.2% and 9.2%, respectively. The deterioration in antireflective feature was attributed to deformation of nanostructures at high temperatures, which was confirmed by scanning electron microscopy (SEM).

Chen [22] designed a W emitter with a complex grating made of superposition of two simple binary gratings. The two gratings had the same height of 0.2 μm while having periods of 0.4 μm and 1.6 μm . The grating was designed to have high emissivity in the high quantum efficiency region of GaSb related cells. Under transverse magnetic (TM) polarized waves, it was seen that the complex grating structure showed broader emissivity peak compared to its constituent simple gratings. The emissivity enhancement was attributed to surface plasmon polariton (SPP) resonance. In the RCWA simulations, the emissivity peak was observed to be insensitive to the direction.

Boden [13] numerically and experimentally investigated the subwavelength “moth eye” structures on Si surface for reflectivity reduction. It was seen that the reflectivity of Si can be reduced below 1% between wavelengths 504-834 nm, for a period of 193 nm. In general, the reflectivity was observed to drop sharply with increasing pillar height, however, fabricating nanostructures of heights beyond the half of the wavelength was deemed too costly. The experimental results indicated that the local maxima of the reflectance spectra strongly depend on the period of nanostructures. It was shown that the EMT approach was inadequate to predict the complex reflectivity spectra of moth eye structures. Methods based on rigorous solutions to Maxwell’s equations such as RCWA was shown to be more compatible with experiments.

Celanovic [23] designed and fabricated W photonic crystals that consisted of deep cylindrical cavities with a period of 1 μm as selective TPV emitters. Depending on the depth and the radius of cavities, emissivity peaks were observed at 974 nm, 1184

nm and 1286 nm wavelengths with three different prototypes. It was noted that by changing nanostructure parameters, the design can be optimized for GaSb, InGaAs, and InGaAsSb cells. In all of the three samples, the emissivity had very sharp cut-offs. Numerical simulations based on finite element method (FEM) predicted the emissivity peaks, although measured emissivity above 1.7 μm of all three prototypes and the flat W surface was larger than the simulated emissivity.

Bandiera [24] showed that the absorptivity of a 100 nm thick Si can be as high as 50% in between wavelengths 700-830 nm, by employing periodic nanostructures. The period and height of the grating was fixed at 540 nm and 108.5 nm, respectively. The absorption enhancement was attributed to the coupling of the light to a resonant guided mode through the periodic grating.

Mavrokefalos [25] showed that inverted nano pyramids on the surface of thin film crystalline Si can greatly enhance its absorption. The fabricated sample consisted of 90 nm SiN_x AR coating, 10 μm Si, 1 μm silica (SiO_2) passivation layer and 200 nm silver (Ag) back reflector. The periodicity of inverted nanopyramids were 700 nm. Based on the efficiency measurements, it was seen that the nanostructured Si of 10 μm thickness could absorb as much light as by a planar Si of 300 μm thickness. The simulated maximum efficiency was independent of the incident angle up to 40°.

Nguyen-Huu [26] developed a W emitter based on a binary grating structure that showed very little polarization dependence. An optimization scheme was performed by using RCWA with a genetic algorithm. At $\lambda=890$ nm, emissivity peaks of 0.997 and 0.935 were observed for TE and TM polarizations, respectively. The emissivity enhancement was attributed to SPP, cavity resonance, and Wood's anomaly.

Arnold [27] fabricated cross slit 2D gratings on a silicon carbide (SiC) surface with a periodicity of 11.5 μm . At 400°C, an emissivity peak close to 90% was observed at $\lambda=12.18$ μm with p polarization. The emission was highly collimated with an angular width around 3.9°. The cause of this coherent thermal emission was identified as the thermal excitation of the surface phonon polaritons.

Rinnerbauer [28] designed and fabricated selective emitters based on 2D tantalum (Ta) photonic crystals. Ta was chosen as the emitter material due to its high melting

point and low vapor pressure. The photonic crystal consisted cylindrical cavities with period of 1.35 μm and depth of 6.26 μm . The surface of Ta was coated with a Hafnia (HfO_2) of 20 nm to prevent the formation of tantalum carbide. The emitter was designed match the bandgap of an InGaAs cell with a target cut-off wavelength of 2 μm . A peak emissivity at 1.78 μm was measured by a Fourier-Transform Infrared (FTIR) spectrometer at normal incidence. The sample showed no degradation after annealing for 1 hour at 1000°C and 144 hours at 900°C.

Zhao [29] numerically demonstrated that the absorptivity of graphene could be increased at desired wavelengths by placing it onto deep metallic gratings. A monatomic graphene sheet was laid on top of an Ag grating with a period of 400 nm and a depth of 200 nm. The wavelengths of MP resonance, 541 nm and 1.49 μm , were not affected by the graphene layer. However, with the addition of graphene, the absorptivity was raised from 0.62 to 0.99 at 541 nm and 0.21 to 0.81 at 1.49 μm .

Yüksel [30] designed a nanostructured W emitter with by optimizing V-groove surface gratings. The emissivity was calculated with the FDTD method, by using TM polarized light normally incident to the surface. A narrow band high emissivity peak was observed at 2.28 μm , matching well with the bandgap of GaInAsSb cell. However, this peak does not occur with the transverse electric (TE) polarized light. At 1200 K, the ratio of electric power to the incident radiative power (TPV efficiency) was calculated as 43%, meanwhile the efficiency of a blackbody emitter at the same temperature was given 20%.

Siddique [31] designed and fabricated nanostructured and thin PV absorbers with disordered nanoholes. The nanostructure was inspired from the scales on the wings of the black butterfly *Pachliopta aristolochiae*. On a 130 nm thick a-Si:H film, nanoholes with diameters 200-280 nm were patterned. The configuration of nanoholes were generated with a Gaussian distribution. The integrated absorptivity between 300-800 nm increased by 93%, compared to unstructured a-Si:H film.

Among the studies on nanostructured surfaces, it is seen that there is a lack of demonstrations on selective TPV cells. Although there are nanostructured Si designs, they are aimed at solar PV which mainly utilizes visible light [25, 31]. TPV cells

mainly utilize IR light and absorption of visible light leads to thermalization which lowers the cell performance and increases the cooling load.

1.3.2. Metal-Insulator-Metal Structures

Lee [32] showed that large emissivity peaks can be obtained by placing a dielectric layer between a metallic layer and periodically spaced metallic strips. The design consisted of Ag bottom layer, a SiO₂ middle layer of thickness 20 nm, and rectangular Ag strips with 20 nm thickness, 250 nm width and 500 nm period. The design with the SiO₂ layer exhibited four reflectivity dips, while the simple Ag grating had only one. It was seen that the extra dips in reflectivity were due to magnetic polariton (MP) resonances, which was confirmed by the equivalent inductor and capacitor (LC) circuit model. It was seen that the magnetic resonance largely depends on the width of the metal strip, while showing little change with the period.

Aydın [33] designed and fabricated a MIM plasmonic absorber with Ag base, SiO₂ dielectric layer and a nanostructured Ag film composed of fishnet-like crossed trapezoidal arrays. The unit cell had a period of 300 nm and total thickness of 260 nm. A broadband and polarization insensitive absorption was achieved over the visible spectrum (400–700 nm). The FDTD simulations yielded an average absorptivity of 0.85 while the measured absorptivity was 0.71. In the designed structure, the light was absorbed in the metallic sections and converted to heat.

Wang [34] designed a magnetic polariton enhanced TPV emitter with W base, SiO₂ spacer and W strips. From 0.62 μm to 1.98 μm, an emissivity over 0.8 was predicted by the RCWA simulations. Close to unity emissivity peaks were observed at 0.73 μm and 1.83 μm. The peak at 1.83 μm was associated with the excitation of MP which was consistent with the prediction of LC circuit model. Although the design shows good spectral selectivity, the MP resonance can only be excited with the TM light, due to the 1D periodicity of the structure.

Zhao [35] proposed a MIM selective emitter with W base, SiO₂ spacer, and square W patches with periodicity of 0.6 μm. Due to the 2D design of the nanostructures, resonance peaks were observed under randomly polarized light. The two major peaks near 0.7 μm and 1.8 μm which were attributed to the excitation of SPP and MP

resonances, respectively. The location of the SPP changed with the incidence angle while the MP was stable under incidence angles up to 60° with TM polarization. However, the strength of MP peak decreased with the incidence angle under TE polarized light.

Wang [9] designed W-SiO₂-W solar absorbers with single sized and multi-sized W square patches. The double-sized metamaterial absorbers showed absorptivity above 0.95 in the wavelength region 0.6-1.8 μm , and below 0.04 between 4-20 μm . It was observed that multi-sized patches allow broader absorption band while single sized patches showed higher absorptivity. In addition, the geometric effects on the absorptivity spectrum are investigated. It was seen that the SPP resonance wavelength strongly depends on the grating period and the angle of incidence, while MP resonance mainly depends on the metallic patch width and spacer thickness.

Woolf [36] fabricated a TPV emitter that consisted of platinum (Pt) base, alumina (Al₂O₃) spacer, and cross shaped Pt patches. The structure was encapsulated by an Al₂O₃ layer in order to withstand high temperatures. The encapsulated emitter was shown to survive temperatures up to 1300 K. At this temperature, the emitter was predicted to demonstrate a spectral efficiency of 43% and TPV efficiency of 22% when coupled with an InGaAs cell.

Song [37] proposed a two-dimensional W-SiO₂-W emitter for TPV applications. In this design, the bottom W layer was also patterned with grating with the same periodicity as the top W patches. For TM polarization, an average emissivity of 0.95 was obtained from 600 nm to 1900 nm. The broadband emissivity peak was considered as the result of SPP and MP resonances.

Shemelya [38] fabricated a Pt-Al₂O₃-Pt emitter on a sapphire substrate. The ellipsometry measurements of the fabricated sample showed a peak absorptivity of 0.6 at the wavelength of 1050 nm, with a full width half maximum of 500 nm. The metamaterial emitter was shown to withstand multiple heating cycles above 650°C with the emissivity spectrum similar to that of pre-heating.

Wang [39] fabricated a MIM solar absorber based on W ground film, Magnesium fluoride (MgF₂) spacer, and titanium (Ti) gratings with a period of 600 nm. Ti was

selected as the grating material rather than W due to ease of fabrication. FTIR measurements showed two major absorption peaks at 0.68 μm and 1.6 μm . The origins of the peaks were determined as SPP and MP resonances, respectively. The FDTD simulations correctly predicted the absorption peaks but underestimated the absorptivity after 1.6 μm .

Ding [40] fabricated a solar absorber composed of gold (Au) base, SiO_2 spacer, and Ti disks with periodicity 600 nm. Ti was chosen to construct the nano disk arrays instead of Au due to the intrinsic high loss of Ti, which decreases the quality factor of the localized surface plasmon resonance. It was argued that the combination of the propagating surface plasmon resonance and the low-quality localized surface plasmon resonance which occur at different wavelengths give rise to a broadband absorption. An absorptivity over 90% was measured by a spectrometer in the wavelength range 900-1825 nm, which was consistent with the numerical simulations based on FEM.

Yokoyama [41] fabricated a thermal emitter with molybdenum (Mo) base, Al_2O_3 spacer, and hexagonal array of Mo disks. The periodicity and diameter of Mo disks were designed as 3 μm and 2.6 μm , respectively. In RCWA simulations, two narrow band absorptions at 3 μm and 7.2 μm were observed. In the FTIR measurements, two peaks were observed at the predicted wavelengths with the emissivity being lower than predicted at 3 μm . After 3-hour vacuum heating at 1000°C, the peaks were still retained with a slight shift.

Han [42] fabricated W- SiO_2 -W based selective solar absorber with disk resonators with periodicity 0.5 μm . The FDTD simulations showed that the absorber had an absorptivity over 90% in the wavelength range of 0.5–1.75 μm which drops sharply to less than 12.6% beyond 2.5 μm . The absorptivity profile remained nearly unchanged up to the incidence angle of 40°. The measured absorptivity showed excellent agreement with the simulations up to 1.75 μm but showed higher absorption than predicted beyond this wavelength.

Matsuno [43] fabricated an MIM emitter with aluminum (Al) and ceria (CeO_2) that exhibits high emissivity around the wavelength of 9.8 μm . The emitter consisted of

an Al base, CeO₂ spacer of 270 nm and Al disks spaced with a period of 4 μm. The emissivity was numerically calculated by FDTD, by choosing the sizes of the minimum meshes as 15 nm in the x and y directions, and 5 nm in the z direction. The FTIR measurements agreed well with the simulations. It was found that the wavelength of peak emissivity shifted with the diameter of Al disks.

Silva-Oelker [44] designed a two-dimensional MIM emitter with W and HfO₂. HfO₂ was chosen as the dielectric material due to its high thermal stability and thermal expansion coefficient that is compatible with W. For shallow gratings, an emissivity of 99.9% was achieved at $\lambda=1.734$ for TM polarization. For deep gratings, emissivity peaks of 97.8% and 99.7% were achieved for TE and TM polarizations, respectively. The emissivity peaks at TM polarization were attributed to SPP and MP resonances, while the high emissivity at TE polarization was attributed to cavity resonances.

Chen [45] compared Au, Ag, copper (Cu), nickel (Ni), Ti, and W in order to develop broadband solar absorbers. The MIM absorbers composed of a metal layer, a SiO₂ dielectric layer, and metallic nanodisks with a period of 200 nm. The upper surface of the metal disks was also covered by the dielectric layer. The numerical simulations based on FEM showed that Ni, Ti, and W resulted in a broader absorption compared to Au, Ag, and Cu. Ni based MIM absorber showed an absorptivity above 95% in the region 300-1180 nm. The absorption mechanism was explained by the surface plasmon resonance, magnetic resonance and the intrinsic absorption properties of the metals.

Sakurai [46] designed a W-SiO₂-W thermal emitter for TPV systems with GaSb cells. The designed emitter showed high emissivity in the high quantum efficiency region of GaSb cells. The origin of emissivity peaks at 0.7 μm and 1.7 μm were explained by the excitation of SPP and MP, respectively. The emissivity of the proposed emitter was shown to be nearly independent of incident and polarization angles. The designed emitter was fabricated, while the diameters of the W disks were patterned larger than intended, leading to a red-shift of the cut-off wavelength. At 1600 K, the simulated efficiency of the TPV system approached 20% while the efficiency of fabricated sample was predicted to be half of this value.

Khorrami [47] proposed two W-SiO₂-W emitter designs for TPV emitters; one with shallow W strips and one with biperiodic deep cylindrical W structures. The first emitter showed an emissivity higher than 0.96 in the broadband spectral region from 0.73 to 1.83 μm , for TM polarization. In the second emitter, an emissivity higher than 0.97 were observed between 0.6-1.6 μm . The parameters of the second emitter were set by using particle swarm optimization (PSO) with RCWA.

Zheng [48] fabricated an Au-SiO₂-Au structure with an array of triangular Au pyramids with height of 200 nm. The reason for selecting pyramids was explained by the larger electromagnetic field enhancement at the edges and corners compared to round shapes. The thickness of SiO₂ was varied from 35 nm to 130 nm. It was found that the reflection dip shifted from 918 nm to 834 nm with increasing SiO₂ thickness.

Isobe [49] designed a selectively absorbing GaSb cell made of metal-semiconductor-metal structure with Au base and square grid (fishnet) electrode layer. FDTD simulations showed that the absorption of GaSb can be enhanced around its bandgap while maintaining high reflectivity in the long wavelength regions.

Dang [50] proposed a metamaterial absorber composed of titanium nitride (TiN) base, SiO₂ spacer, and Ti truncated pyramids placed with a period of 200 nm. At normal incidence the absorber exhibited 98% absorption within 417–1091 nm. A broadband absorption over 95% were maintained up to 40° incidence angle for TE polarization and 20° incidence angle for TM polarized light.

In the literature, it can be seen that MIM designs show promising results as selective emitters. There are several shortcomings among aforementioned studies on MIM emitters. Firstly, although there are emitter designs matching GaSb cell [46], there is a lack of systematic optimization towards developing efficient selective TPV emitters matching GaSb cell. Secondly, there has not been any investigations on the effect of resonator shape on the emissivity profile and TPV performance. Thirdly, to the best of the author's knowledge, there is not any MIM emitter design aimed to spectrally match Si cell.

1.4. Objective and Outline of the Thesis

The objective of this thesis is to investigate the effect of nanostructures on the optical properties of surfaces in order to develop efficient TPV emitters and cells. This thesis does not aim to create a whole TPV system, instead is aimed to study the effects of nanostructures on the performance of individual TPV emitters and cells. This way, the designed nanostructures can be fabricated, tested and incorporated into commercially available TPV systems more easily. Chapter 1 presents the background on thermal radiation, optics, thermophotovoltaics, and nanostructures. Chapter 2 presents the methods used in the development and analysis of spectrally selective TPV emitters and cells. In Chapter 3, MIM based TPV emitters were developed to be paired with GaSb and Si cells, in order to achieve high efficiency and power output in TPV systems. In the design of TPV emitters, commercially available cells such as GaSb cell produced by JX Crystals (JXC) and Si cell developed by The University of New South Wales (UNSW) are considered instead of hypothetical cell designs for better compatibility. In the design of selective emitter matching GaSb cell, MIM structures made of tungsten and silicon dioxide with metallic nanostructures with different shapes were optimized and compared in terms of efficiency and power output. For the design of selective emitters matching Si cell, a novel MIM emitter design made of tantalum and hafnia is optimized. Chapter 4 presents nanostructured Si cell designs for TPV applications in order to increase useful absorption in the cell and decrease the cooling load of TPV systems. For this purpose, 2D and 3D nanostructures are investigated and optimized for Si TPV cell in order to achieve selective high absorption near Si bandgap. Finally, the main conclusions and recommendations for future work are provided in Chapter 5.

CHAPTER 2

METHODS

2.1. Problem Statement

This thesis aims to design and optimize nanostructures in order to propose promising configurations that may lead to overcoming the spectral mismatch between TPV emitter and receivers, and increase their efficiency. The problem statement then can be expressed as: How much TPV emitters and cells can be improved by employing nanostructures? This question was attempted to be answered in two parts:

1. Optimizing nanostructured selective TPV emitters spectrally matching GaSb and Si cells
2. Optimizing nanostructured Si TPV cell to efficiently capture IR light

In these studies, the finite-difference time-domain (FDTD) method is employed to solve the Maxwell's equations in order to quantify the optical characteristics of nanostructures. The periodic design of nanostructures allows to determine the optical response of the nanostructured surfaces by simulating one unit cell. Figure 2.1 shows periodic nanostructures from the literature [26, 27] which can be analyzed by 2D and 3D simulations, respectively.

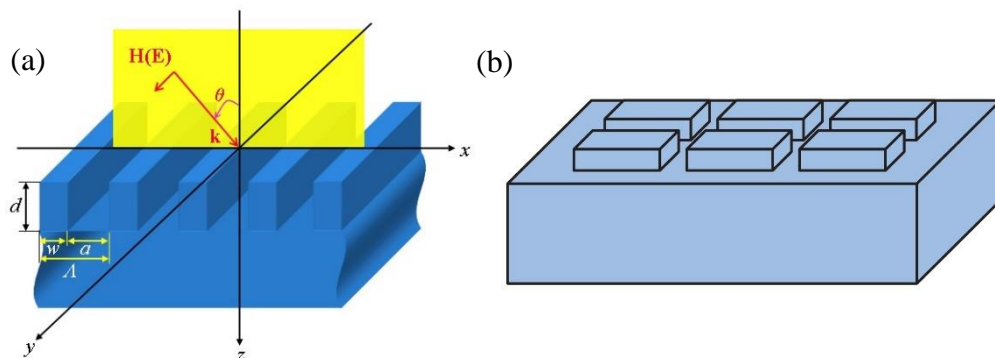


Figure 2.1. (a) 2D nanostructures from Nguyen-Huu et al. [26] (b) 3D nanostructures from Arnold et al. [27]

In TPV applications, the emitter material needs to be resistant to high temperatures. Refractory metals of Tantalum (Ta) and Tungsten (W) have melting temperatures of 3269 K and 3660 K, respectively [2]. These metals are used to design TPV emitters in this thesis. In the first part of Chapter 3, selective MIM emitters for GaSb cells were designed with W and SiO₂ by optimizing and comparing different resonator shapes; disk, square, cone, and pyramid. In the second part of Chapter 3, a selective MIM emitter made of Ta and HfO₂ is optimized to be matched with Si cells. In Chapter 4, 2D (rectangular, triangular and v-groove gratings) and 3D nanostructures (square and pyramid) on Si cell were optimized to achieve selective absorption by Si cell. In order to find the optimum parameters of simple nanostructures in Chapter 4, a grid search optimization method is employed. For more complex MIM nanostructures of Chapter 3, the Particle Swarm Optimization (PSO) method is utilized. The methodology employed in design and optimization of nanostructured TPV components is outlined in Figure 2.2. The following chapters give more detailed description of numerical methods used in this thesis.

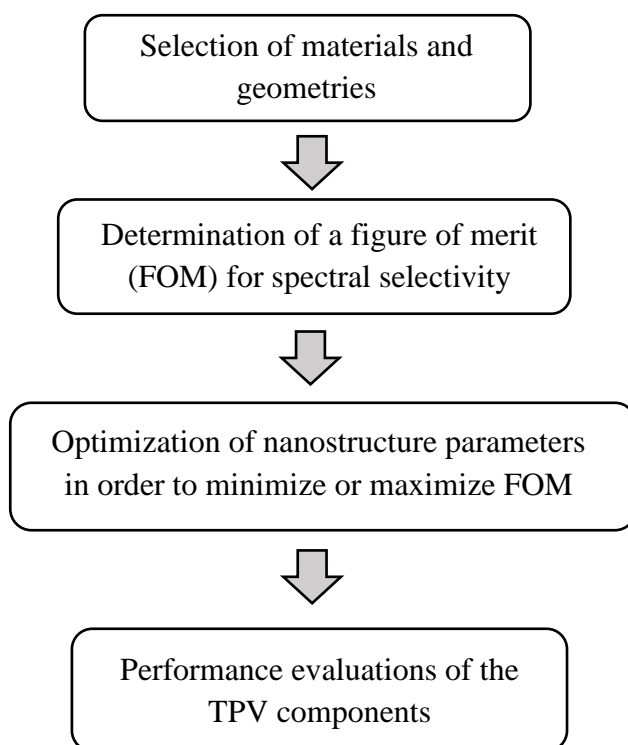


Figure 2.2. Flowchart of the methodology

2.2. The Finite-Difference Time-Domain (FDTD) Method

Originally developed by electrical engineer and mathematician Kane S. Yee [51], the finite-difference time-domain (FDTD) method is a grid based numerical method developed for solving Maxwell's equations. The main advantages of FDTD are its ease of application and ability to resolve arbitrarily complex geometries as long as the mesh size is sufficiently small. The main disadvantage of FDTD is that the mesh size should be small enough to resolve both the smallest structure and the smallest wavelength, which makes it computationally expensive.

In FDTD, Maxwell's curl equations are discretized in a central difference manner, both in time and space. The basic computational unit of the FDTD algorithm is the Yee lattice (Yee cell) as shown in Figure 2.3 [52].

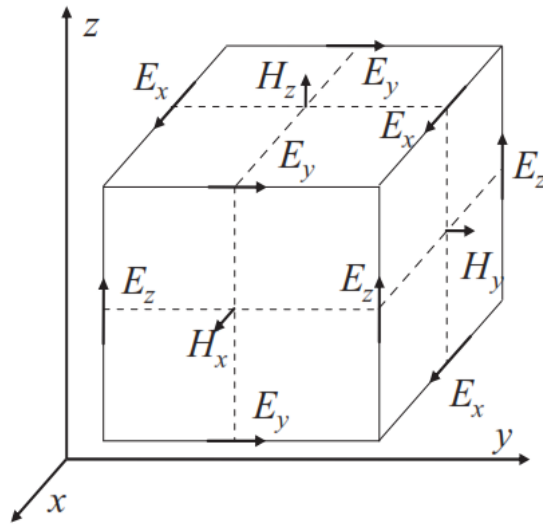


Figure 2.3. Yee lattice [52]

FDTD aims to solve for the curl equation of Maxwell. The divergence equations are not solved since they are automatically satisfied. Omitting the current term (\mathbf{J}) for simplicity, Maxwell's curl equations can be rewritten as:

$$\frac{\partial \mathbf{H}}{\partial t} = -\frac{1}{\mu} \nabla \times \mathbf{E} \quad (26a)$$

$$\frac{\partial \mathbf{E}}{\partial t} = \frac{1}{\epsilon} \nabla \times \mathbf{H} \quad (26b)$$

In time domain, the differential Eqs. (26a) and (26b) can be approximated as finite-difference algebraic equations, as [53] :

$$\frac{\mathbf{H}\left(t + \frac{\Delta t}{2}\right) - \mathbf{H}\left(t - \frac{\Delta t}{2}\right)}{\Delta t} = -\frac{1}{\mu} \nabla \times \mathbf{E}(t) \quad (27a)$$

$$\frac{\mathbf{E}(t + \Delta t) - \mathbf{E}(t)}{\Delta t} = \frac{1}{\epsilon} \nabla \times \mathbf{H}\left(t + \frac{\Delta t}{2}\right) \quad (27b)$$

In a Yee lattice shown in Figure 2.1, every \mathbf{H} vector component is surrounded by four \mathbf{E} vector components. The \mathbf{H} component at any time increment can be found with the knowledge of previous \mathbf{H} component and the circulating \mathbf{E} components. In the next time step, the Yee Lee lattice is centered around an \mathbf{E} component and the value of \mathbf{E} component is updated with the knowledge of solved \mathbf{H} components. \mathbf{H} and \mathbf{E} components of the electromagnetic field are updated back and forth. This solution method is known as the “leap-frog”.

For computational stability, the time and spatial steps should satisfy the Courant stability condition:

$$\Delta t \leq \frac{1}{c\sqrt{(1/\Delta x)^2 + (1/\Delta y)^2 + (1/\Delta z)^2}} \quad (28)$$

Since it is a time domain method, FDTD records the values of \mathbf{E} and \mathbf{H} fields in discrete time steps. In order to find the fields in the frequency domain, Fourier transform is employed. Then, the reflectivity and absorptivity can be evaluated at any frequency by using time-averaged Poynting vector (\mathbf{S}) using Eq. (29).

$$\langle \mathbf{S}(\omega) \rangle = \frac{1}{2} \text{Re}(\mathbf{E}(\omega) \times \mathbf{H}(\omega)^*) \quad (29)$$

where * denotes the complex conjugate.

FDTD method can be applied to a wide scale of frequency and size. It is shown that FDTD results are compatible with the geometric optics (e.g., ray tracing) in the short wavelength limit and EMT in the long wavelength limit [14]. FDTD is widely employed in nanophotonic research and used to simulate the interaction of electromagnetic radiation with nanostructures both in far field regime [26, 39, 46, 54] and the near-field regime [55].

2.2.1. ANSYS Lumerical

In this thesis, the FDTD module of the commercial software ANSYS Lumerical (Lumerical FDTD) is used to perform FDTD simulations. The basic layout of Lumerical FDTD is given in Figure 2.4.

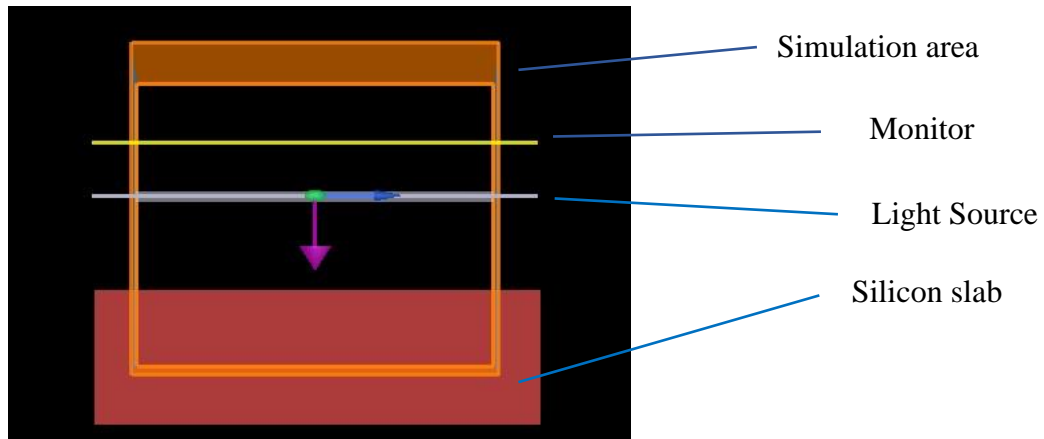


Figure 2.4. Lumerical FDTD layout with simulation components

In the simulations, a plane light source is incident normal to the x - y plane is used. The x and y boundary conditions are periodic, since the unit cell repeats both in x and y directions. The z boundary conditions are set as perfectly matched layers (PML) in order to prevent reflections from the boundaries. This set of boundary conditions is frequently employed in the simulation of periodic nanostructures [30, 56] and shown to be consistent with experiments [43]. In all simulations throughout the thesis, the background is assumed to be air ($n = 1$) and all materials are nonmagnetic ($\mu_r = 1$). In the simulation area, a monitor is placed behind the light source to record the reflected radiation.

2.2.2. Validation Studies

In order to verify the method; the FDTD simulations are compared to three types of results; analytical calculations, numerical studies and experimental studies.

2.2.2.1. Comparison with Analytical Calculations

The first part of verification consists of comparing the analytical (exact) reflectivity calculations with the numerical calculations carried out by the FDTD method. The reflection of a light beam incident normally to a surface is calculated by Fresnel's law.

$$\rho = \left| \frac{\tilde{n}_1 - \tilde{n}_2}{\tilde{n}_1 + \tilde{n}_2} \right|^2 \quad (15)$$

Eq. (15) can be written more explicitly in terms of the refractive index (n) and the extinction coefficient (k) of materials that constitute the interface.

$$\rho = \frac{(n_1 - n_2)^2 + (k_1 - k_2)^2}{(n_1 + n_2)^2 + (k_1 + k_2)^2} \quad (30)$$

If one wants to calculate the reflectivity at an interface between a dispersive medium and air, Eq. (30) reduces to Eq. (31), since $n_{air} = 1$ and $k_{air} = 0$.

$$\rho = \frac{(n - 1)^2 + k^2}{(n + 1)^2 + k^2} \quad (31)$$

In order to work out what mesh size gives sufficiently close results to analytical reflection calculations, a mesh convergence test is conducted. In FDTD, the mesh size should be at least 10 times smaller than the smallest wavelength that is simulated [14]. In TPV applications (1000-2500 K), the radiation below 0.5 μm is negligible, therefore in the scope of this thesis, correct simulation of wavelengths 0.5 μm and longer is needed. Starting from the mesh size of 40 nm, the FDTD results of reflectivity from the air-Si interface at 0.5 μm is given in Figure 2.5. The mesh size is decreased by 2-fold at each step. The optical properties of Si are taken from Green [57].

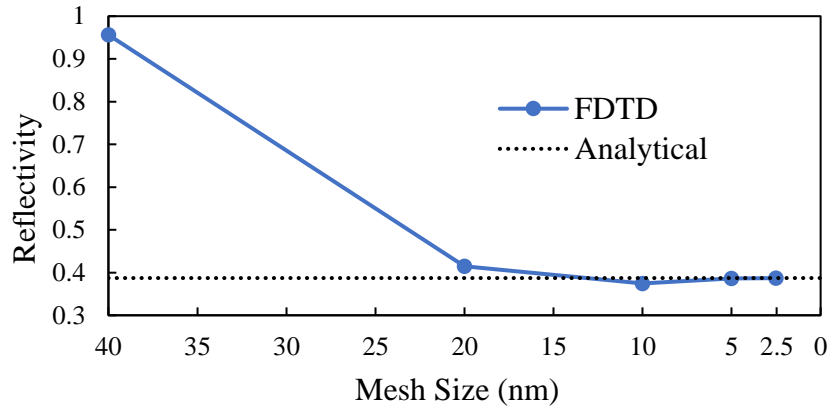


Figure 2.5. Reflectivity of silicon at $\lambda = 0.5 \mu\text{m}$, analytical (exact) results vs. FDTD simulations with various mesh size.

The deviation from the analytical results is 0.29% at 5 nm and 0.1% at 2.5 nm mesh sizes. In order to save computational time, 5 nm mesh size is used for the rest of the simulations. The reflectivity of Si between 0.25-1.25 μm calculated analytically and by FDTD are plotted in Figure 2.6. The FDTD results agree well with the analytical results with the maximum deviation of 3.18% at 0.31 μm .

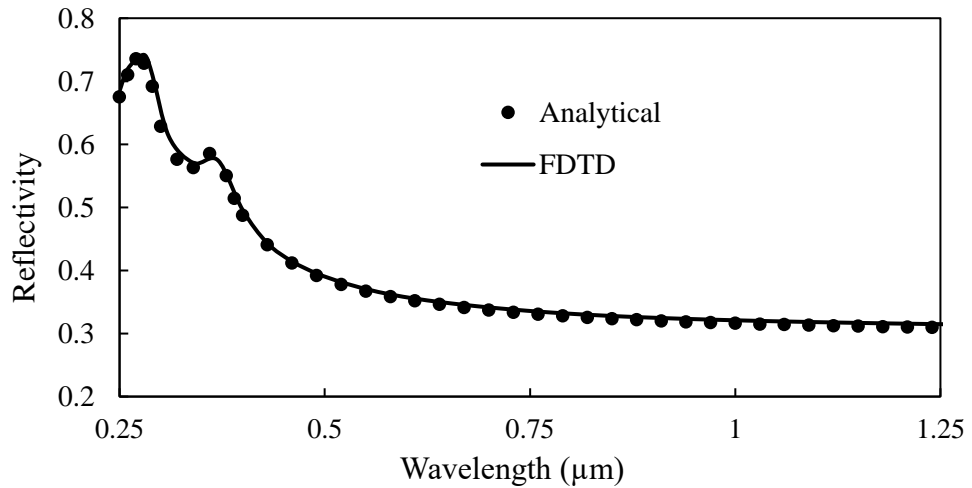


Figure 2.6. The reflectivity of silicon, analytical results and FDTD simulations

Next, the reflectivity of Ta and W are calculated by Eq (31) and by FDTD with mesh size of 5 nm. In Figure 2.7, the reflectivity spectra of Ta and W, calculated analytically and by FDTD method are given. The optical constants of Ta and W are

taken from Palik [58]. The FDTD agrees with the analytical results with maximum deviations of 1.06% for Ta and 1.17% and W.

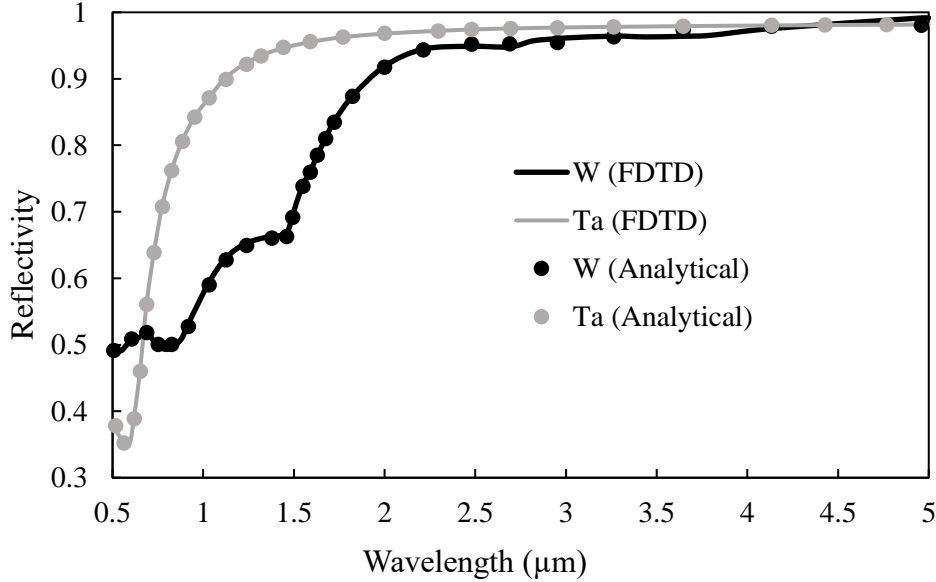


Figure 2.7. The reflectivity spectra of Tantalum (Ta) and Tungsten (W), analytical results and FDTD simulations

2.2.2.2. Comparison with Previous Numerical Studies

Sai [21] used RCWA method to simulate the reflectivity from a flat Si surface and Si surface patterned with nanopylamids. The RCWA results of Sai [21] for flat Si and nanostructured Si, compared to analytical and FDTD results are presented in Figure 2.8. The current FDTD simulation of the same structure agrees with the RCWA result between 0.3-1.25 μm . However, FDTD predicts an additional reflectivity peak around 0.28 μm , which is absent in the RCWA simulation. In the case of the flat Si surface, the RCWA simulation of Sai [21] agrees with the exact results except for the peak at 0.28 μm . The existence of this peak on flat Si indicates that it originates from the inherent optical characteristics of Si. Therefore, it can be concluded that, the current FDTD simulation predicts the reflectivity of Si more correctly compared to the RCWA.

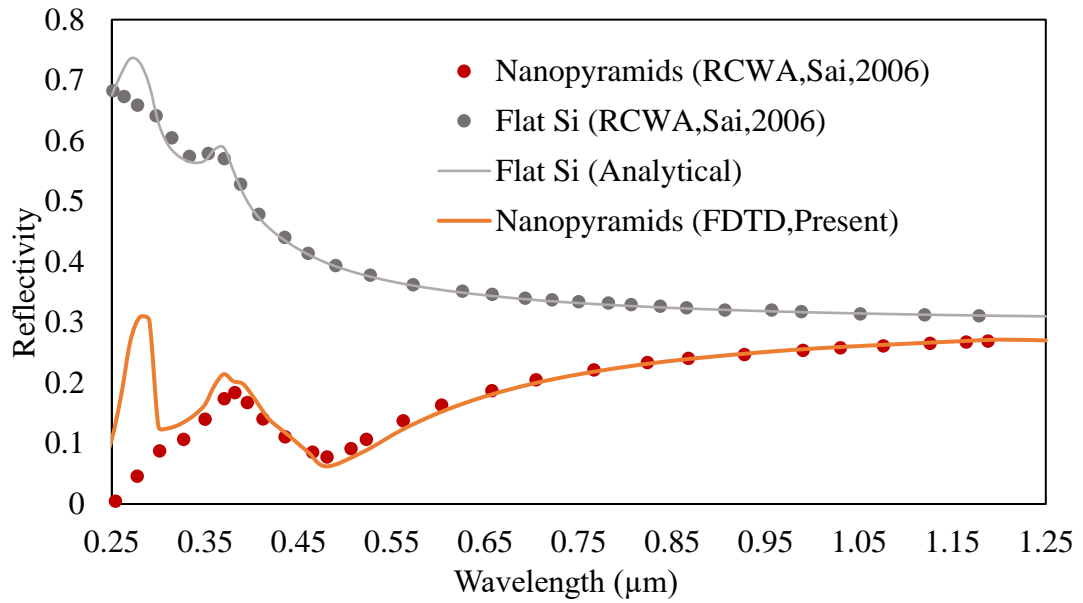


Figure 2.8. The RCWA results of Sai [21] for flat Si is and nanostructured Si, compared to analytical and FDTD results.

Sakurai [46] designed a MIM emitter based on W and SiO₂. The FDTD calculations of Sakurai and the present FDTD calculation of the same structure is give in the Figure 2.9. The present FDTD results show very good agreement with the FDTD simulation of Sakurai.

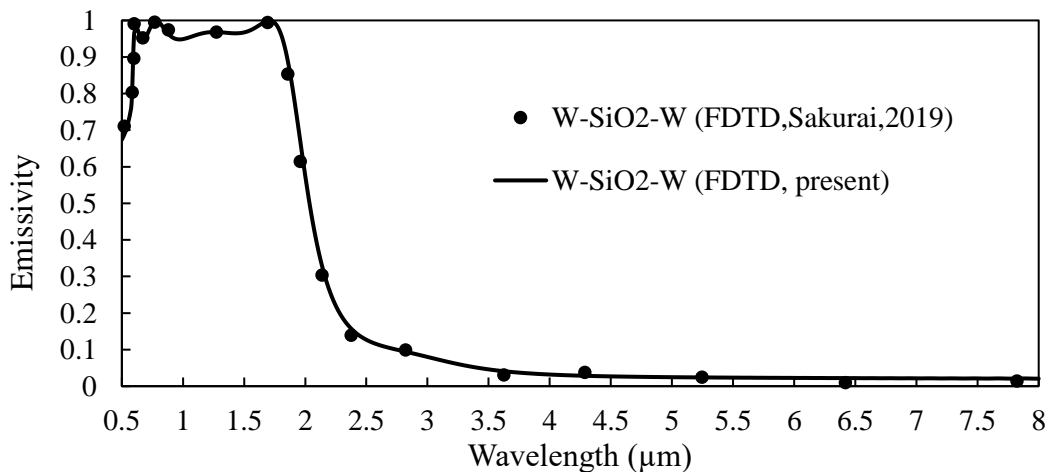


Figure 2.9. The emissivity spectrum of W-SiO₂-W emitter, FDTD results of Sakurai [46] and current FDTD simulation.

2.2.2.3. Comparison with Previous Experimental Studies

Han [42] fabricated a W-SiO₂-W based selective solar absorber using a W nanodisk array. The measurement was carried out using a spectrophotometer (Lambda 950, PerkinElmer) with an oblique angle 8° from the normal. The schematic and the SEM image of the absorber is given in Figure 2.10. The experimental results of Han, compared to present FDTD results are given in Figure 2.11.

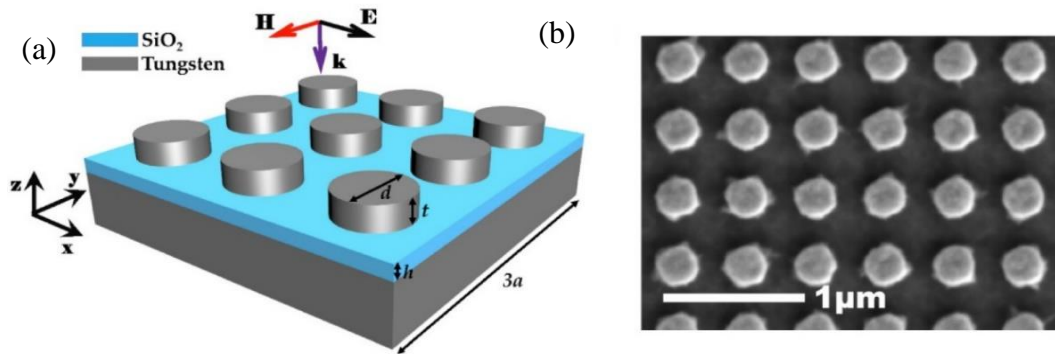


Figure 2.10. (a) The schematic of absorber design by Han [42], with $d=300$ nm, $a=500$ nm, $h=100$ nm, and $t=60$ nm. (b) SEM image of the fabricated absorber

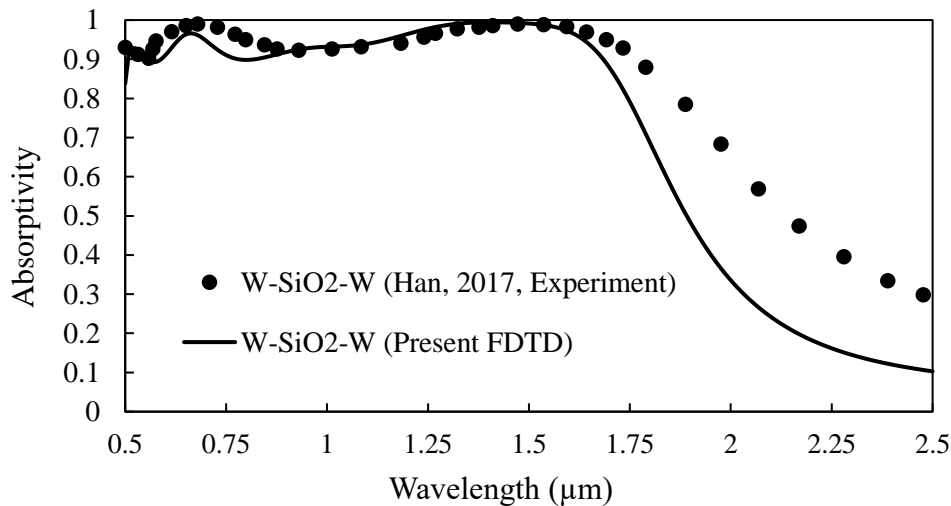


Figure 2.11. The spectral absorptivity of the emitter design by Han [42], measured values vs FDTD simulations.

The FDTD results agree with the measured values up to the cut-off wavelength around 1.6 μm . At longer wavelengths, FDTD underestimates the spectral absorptivity. Understanding of the origin of this discrepancy requires further analysis. Wang [39] reports a similar result where the FDTD simulation shows good agreement with the measurements up to the cut-off wavelength, but underestimates the absorption at higher wavelengths. In a work by Kim [59], the discrepancy between numerical and experimental results were attributed to the impurities (such as oxygen) present in the sputtered W layer.

Overall, it is seen that current FDTD simulations with mesh size of 5 nm agrees well with the exact results and FDTD simulations done by other researchers. The FDTD is also consistent with the RCWA simulations and experiments with a reasonable accuracy.

2.3. Derivative-free Optimization Methods

Derivative-free or gradient-free optimization methods are a large class of stochastic optimization algorithms which do not require the derivatives of the function that is to be optimized. For a continuously differentiable function, the minima and maxima can be found by equating the derivatives of that function to zero. However, in many engineering applications, derivatives are either unavailable or too costly to acquire. In some of these situations, one can apply finite difference approximations to evaluate the derivatives, in other cases the function may be noisy or sometimes unknown. Most of the naturally occurring problems are often complex, nonlinear, and not explicitly defined [60]. Nevertheless, sometimes it is still desirable to perform an optimization, and in this case, derivative-free optimization methods can be employed.

2.3.1. Parameter Sweep

One method of finding the extrema of a function is checking all the available solutions. This is called the brute-force or exhaustive research. Although it is easy to implement and guaranteed to find a solution, it is computationally expensive and the required computational power grows with the number of potential solutions. In continuous functions where there are infinite number of candidate solutions, the function can be evaluated at discretely spaced points in order to create a solution

space. This is called the parameter sweep or grid search method. In this method, parameters are swept through a range of values determined by the user. The computational cost grows exponentially with the number of parameters. Nevertheless, parameter sweep can be employed when the problem size is limited and can also be used to benchmark other optimization algorithms. In this thesis, parameter sweep is employed when the number of parameters does not exceed two, that is being the nanostructures in Chapter 4.

2.3.2. Particle Swarm Optimization

Particle swarm optimization (PSO) is a heuristic optimization algorithm that aims to find optimum values by iteratively improving the candidate solutions. Originally proposed by Kennedy and Eberhart [61], the PSO works by generating possible solutions called “particles”, then moving these particles in the solution space until maximum number of generations or a given convergence criteria is achieved. The movements of particles are affected both by their personal best positions and the best positions attained by the other particles. A mathematical description of the velocity (v) and the position (x) of each particle at each iteration are given in Eqs. (32a) and (32b) [62]. With this iterative process, eventually, all particles are expected to flock to the global best position, similar to bees swarming around the region with highest flower density.

$$v = w \cdot v + c_1 r_1 (p_{best} - x) + c_2 r_2 (g_{best} - x) \quad (32a)$$

$$x = x + v \quad (32b)$$

In Eq. (32), w is the inertia factor, c_1 and c_2 are weights, r_1 and r_2 are random coefficients, p_{best} is the personal best position a particle has encountered, and g_{best} is the global best position encountered by all particles. In this work, $w = 0.729$, and $c_1 = c_2 = 1.494$ are used as recommended by Robinson [63] for electromagnetics. In this thesis, PSO is utilized for the optimization of MIM nanostructures in Chapter 3.

2.4. TPV Performance Evaluations

The performance evaluation metrics are presented in three parts. First part presents a method to quantify how efficiently a TPV emitter radiates energy. The second part gives the theoretical limits of power output and efficiency of the TPV systems with

hypothetical perfect cells. The third part presents a more realistic calculation of power output and efficiency when TPV emitters were paired with real life cells. The TPV performance evaluations presented in this thesis assume constant emitter and cell temperatures. Directional effects, view factor losses, near-field effects, photon recycling (photons reflected by the cell picked up by the emitter) and the thermal emission of the cell are neglected.

2.4.1. In-band Radiation and Emitter Efficiency

The total emissive power of the emitter can be calculated by integrating the spectral emissive power over all wavelengths.

$$E_{total} = \int_0^{\infty} \varepsilon_E(\lambda) E_{\lambda,b}(\lambda, T_E) d\lambda \quad (33)$$

For a blackbody, $\varepsilon = 1$ and the integral equates to σT^4 . The in-band radiation is the portion of emitted radiation that can be utilized by TPV cell to generate electricity. In other words, it is the sum of the energies of all in-band photons. For any thermal emitter, the amount of in-band radiation can be calculated by integrating the spectral emissive power from $\lambda = 0$ to $\lambda = \lambda_g$.

$$E_{in} = \int_0^{\lambda_g} \varepsilon_E(\lambda) E_{\lambda,b}(\lambda, T_E) d\lambda \quad (34)$$

The emitter efficiency (η_E), sometimes called the spectral efficiency [64] or selective emission efficiency [18] is defined as the ratio of in-band radiation to the total emissive power of the emitter at a given temperature.

$$\eta_E = \frac{E_{in}}{E_{total}} = \frac{\int_0^{\lambda_g} \varepsilon_E(\lambda) E_{\lambda,b}(\lambda, T_E) d\lambda}{\int_0^{\infty} \varepsilon_E(\lambda) E_{\lambda,b}(\lambda, T_E) d\lambda} \quad (35)$$

2.4.2. Maximum Theoretical Power Output and Efficiency

The theoretical limit of maximum power output ($P_{el,max}$) and efficiency (η_{max}) of a TPV system can be calculated by assuming a “perfect cell”, which is the PV cell model used by Shockley and Queisser to calculate the ultimate efficiency of solar cells [11]. In this model, the only mechanism of loss is the excess energy of the high energy photons (thermalization). In PV effect, one in-band photon creates one

electron-hole pair, regardless of the energy it carries. The energy of a photon is proportional to its frequency, hence inversely proportional to its wavelength.

$$E_{\text{photon}} = \frac{hc}{\lambda} \quad (36)$$

The portion of photon energy that is utilized by the cell can be found by dividing the bandgap energy to the energy of the in-band photon:

$$\frac{E_g}{E_{\text{photon}}} = \frac{hc/\lambda_g}{hc/\lambda} = \frac{\lambda}{\lambda_g} \quad (37)$$

In a perfect cell, every in-band photon that is absorbed contributes to the power generation, with a fraction of its energy according to Eq. (37). The maximum power density can be calculated by [11]:

$$P_{el,max} = \frac{1}{\lambda_g} \int_0^{\lambda_g} \alpha_c(\lambda) \varepsilon_E(\lambda) E_{\lambda,b}(\lambda, T_E) \lambda d\lambda \quad (38)$$

In Eq. (38), the absorptivity of the cell (α_c) can be assumed 1 to calculate maximum power output. The maximum theoretical efficiency for a TPV system can be calculated by dividing the maximum power output to the total emissive power of the emitter.

$$\eta_{max} = \frac{P_{el,max}}{E_{total}} \quad (39)$$

An equivalent formulation of maximum theoretical efficiency is given by Chubb [11]:

$$\eta_{max} = \frac{1}{\lambda_g} \frac{\int_0^{\lambda_g} \left[\frac{\varepsilon_E(1 - \rho_c) E_{\lambda,b}}{1 - \rho_E \rho_c} \right] \lambda d\lambda}{\int_0^{\infty} \left[\frac{\varepsilon_E(1 - \rho_c) E_{\lambda,b}}{1 - \rho_E \rho_c} \right] d\lambda} \quad (40)$$

It should be noted that this formulation gives rise to singularities when $\rho_E = \rho_c = 1$. In case of ideal spectral control given in Eq. (25), the emitter only emits in-band radiation. Hence, the maximum efficiency for an ideal system can be calculated by;

$$\eta_{max,ideal} = \frac{P_{el,max}}{E_{in}} \quad (41)$$

As a verification, maximum efficiency values for a TPV system with GaSb cell paired with a blackbody and ideal emitters at 1700 K are calculated. For a blackbody at 1700 K, the total emissive power can be calculated from the Stefan-Boltzmann Law. The

maximum output power is calculated from Eq. (38) with $\varepsilon_E = \alpha_c = 1$ and $\lambda_g = 1.72 \mu\text{m}$. The calculated blackbody emissive power, in-band radiation, maximum electrical power, TPV efficiencies for the blackbody case and ideal case are given in Table 2.1. This calculated η_{max} and $\eta_{max,ideal}$ are identical to the estimations by Chubb [11].

Table 2.1. The blackbody emissive power, in-band radiation, maximum power output, maximum blackbody efficiency and ideal emitter efficiency of a TPV system with 1700 K emitter paired with a GaSb cell

$E_{bb} (\text{W cm}^{-2})$	$E_{in} (\text{W cm}^{-2})$	$P_{el,max} (\text{W cm}^{-2})$	$\eta_{max,bb}$	$\eta_{max,ideal}$
47.356	12.111	9.458	20%	78%

2.4.3. Realistic Power Output and Efficiency

The thermophotovoltaic system efficiency (η_{TPV}) is calculated by dividing electrical power output from the TPV system to the total emissive power of the emitter.

$$\eta_{TPV} = \frac{P_{el}}{E_{total}} \quad (42)$$

The electrical power output (P_{el}) from a TPV cell is a fraction of the product of the maximum possible voltage (open circuit voltage, V_{oc}) and the maximum possible current (short circuit current, J_{sc}) [11]:

$$P_{el} = FF \cdot J_{sc} \cdot V_{oc} \quad (43)$$

In Eq. (43), FF denotes the *fill factor*. The maximum possible current occurs when the PV cell is short circuited. This is called the short circuit current density (J_{sc}) or the photocurrent density. Calculation of J_{sc} requires the knowledge the *quantum efficiency* of the cell. Quantum efficiency is defined as the probability of a photon to create an electron-hole pair. The *internal quantum efficiency* (IQE) is the number of electron-hole pairs generated by an absorbed photon while the *external quantum efficiency* (EQE) is the number of electron-hole pairs created per incident photon. The EQE and IQE are related to each other by; $EQE = \alpha_c \cdot IQE$. The quantum efficiency is a spectral property of the cell and usually obtained by measurements. The J_{sc} can be calculated by Eq. (44) [65]:

$$J_{sc} = \frac{e}{hc} \int_0^{\infty} \varepsilon_E(\lambda) \cdot EQE(\lambda) \cdot E_{\lambda,b}(\lambda, T_E) \lambda d\lambda \quad (44)$$

If there is no current present, maximum possible voltage is achieved. This is called the open circuit voltage (V_{oc}) and is calculated by [66]:

$$V_{oc} = \frac{nk_B T_c}{e} \ln \frac{J_{sc}}{J_0} \quad (45)$$

In Eq. (45), n is the *ideality factor* that can take a value between 1 and 2. In this thesis it is assumed to be 1 for ideal diode. In Eq. (45), J_0 denotes the reverse saturation current density (the dark current) which represents the current flowing in reverse direction when there is no light present. J_0 depends on the material as well as the temperature of the cell. An empirical correlation for the minimum J_0 (in A/cm²) as a function of bandgap (in eV) and temperature (in K) of the cell is given by [66]:

$$J_0 = 1.5 \cdot 10^5 \exp\left(\frac{-E_g}{k_B T_c}\right) \quad (46)$$

In the case of the GaSb cell, an expression for J_0 was derived by Fraas [67]:

$$J_0 = 1.84 \cdot 10^{-3} T_c^3 \exp\left(\frac{-E_g}{k_B T_c}\right) \quad (47)$$

Then, the fill factor is calculated by [68]:

$$FF = \beta \frac{v - \ln(v + 0.72)}{v + 1} \quad (48)$$

where v is the normalized open circuit voltage given by [66]:

$$v = \frac{V_{oc}}{nk_B T_c / e} \quad (49)$$

In Eq. (48), β is the amendment factor which accounts for cell parasitic losses. In this article, $\beta = 0.96$ is used as recommended by Qiu [68]. In Eqs. (45), (46), (47) and (49), the cell temperature (T_c) is assumed to be 300 K.

It is worth noting that, both maximum and realistic power calculations assume a view factor of unity between the emitter and the receiver. A view factor close to unity can be achieved by placing the emitter and receiver in concentric cylinders or minimizing the distance between the emitter and the receiver. When the gap between the emitter and the receiver surfaces are smaller than the characteristic wavelength of the

radiation, near field effects start to be dominant. In this case, the electrical power calculations should be modified in order account for near-field radiation, which can surpass the blackbody radiation by several orders of magnitude [69]. Throughout this thesis, the contribution of the near field heat transfer is assumed to be negligible.

In order to determine whether the method works successfully, two validation studies are performed. In the first case, the efficiency of a TPV system with GaSb cell produced by JX Crystals (JXC) and the blackbody emitter is calculated. The *EQE* of JXC GaSb cell is taken from Frass [70]. J_0 is calculated with Eq. (47) with $E_g = 0.72$ eV. The results are compared with Sakurai [46] who used method similar to that of Loferski [71] to calculate the power output. Figure 2.12 shows the TPV system efficiencies for GaSb and a blackbody emitter, present calculation and calculation by Sakurai [46].

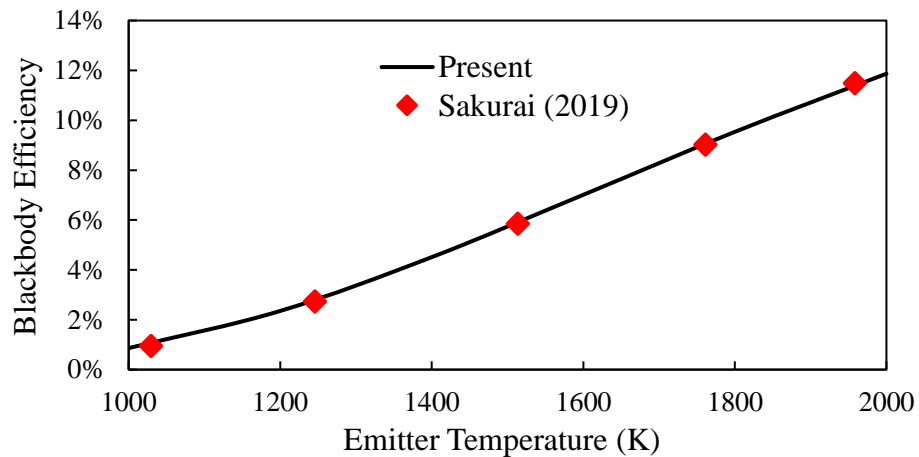


Figure 2.12. Efficiency of a TPV system with GaSb cell and blackbody emitter

For a second validation, the power output from a Si cell developed by UNSW operated under the Sun is calculated and compared with the experimental data. The J_{sc} , V_{oc} and FF values are calculated for a Si cell illuminated by sun, by replacing the incident power ($\epsilon_\lambda E_\lambda$) in Eq. (44) with global 1.5 air mass (AM1.5) solar spectrum [72]. The J_0 is calculated by Eq. (46) with $T_c = 300$ K and $E_g = 1.1$ eV. The predicted results were compared to the experimental results of Zhao [73] in Table 2.2.

Table 2.2. The predicted and measured values of J_{sc} , V_{oc} and FF of UNSW silicon solar cell under AM1.5 solar spectrum

Method	J_{sc} (mA cm ⁻²)	V_{oc} (V)	FF (%)
Predicted in this chapter	42.1	0.708	81.3
Measured (Zhao [73])	41.5	0.704	81.0

Based on the measured values of Zhao [73], the power output can be calculated from Eq. (43) as 0.0237 W cm⁻², which is 2% lower than the predicted power output of 0.0242 W cm⁻². The difference can be explained by the variations in sunlight, and the calculation of the reverse saturation current, J_0 . Eq. (46) gives an estimate for the minimum value of J_0 . In real systems, J_0 is expected to be higher, which would decrease the power output from the PV cell. Overall, the predicted and measured power outputs show good agreement with a maximum deviation of 2%, hence, the model is shown to work correctly.

CHAPTER 3

DESIGN AND OPTIMIZATION OF METAL-INSULATOR-METAL SELECTIVE THERMOPHOTOVOLTAIC EMITTERS

This chapter of the thesis is aimed at developing selective emitters to have emissivity spectra matching with the bandgap of TPV cells. In an efficient TPV system, the emitter should mainly emit photons with energies higher than or equal to the bandgap of the cell, i.e., in-band photons. Nanopatterning the surface with periodic structures can reduce reflectivity and increase the absorptivity/emissivity of the material [14, 20, 24, 30, 74]. Metal-insulator-metal (MIM) configurations were shown to create multiple plasmonic resonances that allows tunable absorption/emission peaks [32, 33, 41, 75, 76] which is a useful feature for TPV emitters. Several researchers employed MIM structures to design selective TPV emitters [34, 36, 77, 78], solar absorbers [42, 79], and TPV cells [49]. GaSb and Si are the two most popular cells used in TPV prototypes [80]. The lower bandgap of GaSb ($E_g = 0.72$ eV [12]) makes it more suitable than Si for TPV systems with currently attainable emitter temperatures. However, its availability and relative inexpensiveness make Si cells attractive as well. In this part of the thesis, two selective emitters were designed and optimized to be paired with GaSb and Si cells, respectively, by employing FDTD and PSO methods. In the design of TPV emitters, the properties of GaSb and Si cells were taken from commercially available cells instead of hypothetical cell designs for better compatibility.

3.1. Design and Optimization of Tungsten-Silicon Dioxide-Tungsten (W-SiO₂-W) Emitter Matching GaSb Cell

3.1.1. Material

GaSb has a direct bandgap of 0.72 eV [12], which corresponds to the energy of a photon with the wavelength of 1.72 μm . According to Wien's Displacement Law, in order to have thermal radiation peak at this wavelength, a blackbody should be heated up to 1680 K. For ideal performance, the emitter material(s) should be stable at working temperatures. In this chapter, W is selected as the metal base, due to its high emissivity in the range that is suitable for GaSb cell and its high melting temperature (3660 K [2]). In MIM designs, weakly absorbing dielectric oxides are usually used as the insulator layer. SiO₂ is largely transmissive to visible and near infrared light and has a melting temperature of 1883 K [2], hence it is chosen as the dielectric spacer. MIMs consisting from W and SiO₂ were shown to exhibit broadband high emissivity/absorptivity in the sensitive region of GaSb cells [34, 35, 42, 46]. MIMs composed of W and SiO₂ have been successfully fabricated as TPV emitters [46], and solar absorbers [42]. Kim [59] has shown that a TPV emitter composed of multiple W and SiO₂ thin layers were stable at 1300 K although they displayed delamination spots at 1400 K. Compared to the design of Kim [59], the MIM structure has fewer layers, hence it is expected to be more resistant to delamination at higher working temperatures.

Majority of the MIM studies are focused on one resonator type, which were usually disks or square patches. To the best of the author's knowledge, there are limited number of MIM studies with pointy resonators such as pyramids or cones, and none were thus far optimized as TPV emitters. Zheng [48] fabricated a MIM structure composed of SiO₂ dielectric layer and Au nanopyramid arrays. It was argued that the pyramid shaped resonators exhibit larger electromagnetic field enhancement at the corners and edges as compared to round shapes. Dang [50] designed a metamaterial absorber with truncated pyramid resonators, and reported that broadband high absorption was achieved over the visible and near-infrared range. Thus, a comprehensive study of both flat and pointy resonators is needed to determine the

effect of resonator shape on the design of TPV emitters. This part of the thesis is aimed at designing MIM emitters based on W metallic layer and SiO₂ spacer, to be paired with GaSb cells, by independently optimizing the nanostructure parameters of the following four resonator shapes: square patches, disks, pyramids, and cones. The performance of emitters is compared in terms of the emitter efficiency, power output and TPV system efficiency.

3.1.2. Method

An ideal broadband TPV emitter has an emissivity of 1 above the bandgap and 0 below the bandgap as given in Eq. (50):

$$\varepsilon(\lambda) = \begin{cases} 1, & 0 < \lambda \leq \lambda_g \text{ } \mu\text{m} \\ 0, & \lambda > \lambda_g \text{ } \mu\text{m} \end{cases} \quad (50)$$

Although Eq. (50) represents the ideal case, obtaining an emissivity spectrum with a sharp cut-off as like this is challenging, if not impossible. In order to maximize in-band radiation with high utility, researchers usually try to obtain a peak emissivity at around the bandgap. However, having a peak emissivity at λ_g results in considerable emission for $\lambda > \lambda_g$, which in turn decreases the overall efficiency. Other than the bandgap, one other important parameter for TPV emitter design is the external quantum efficiency (*EQE*) of the cell. *EQE* is defined as the number of electron-hole pairs created per incident photon. Most PV cells do not have their highest quantum efficiencies at their bandgaps. For example, GaSb has a bandgap of 1.72 μm , but the GaSb cell produced by JX Crystals (JXC) has peak *EQE* around 80% at $\lambda = 1.5 \text{ } \mu\text{m}$ which falls sharply after 1.60 μm [70]. The *EQE* of JXC standard GaSb cell is presented in Figure 3.1.

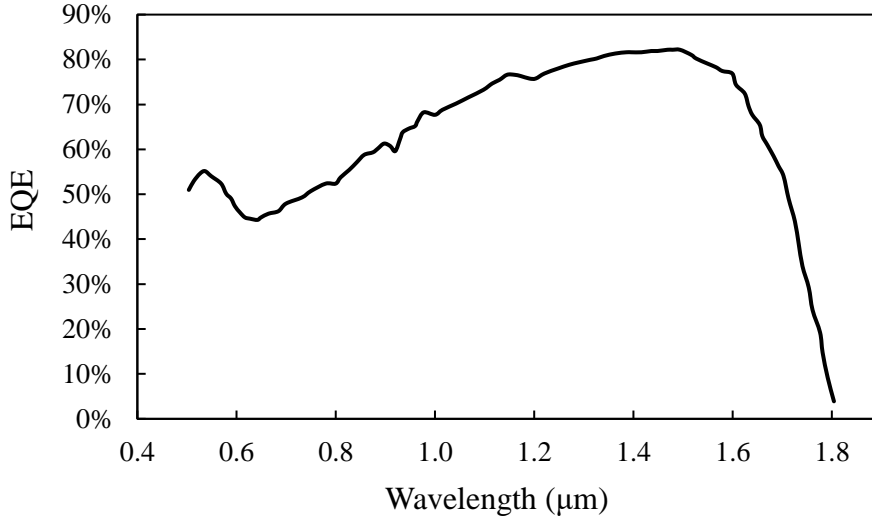


Figure 3.1. The EQE of JXC standard GaSb cell [70]

Between the wavelengths 0.9-1.66 μm , GaSb has an *EQE* of $> 60\%$. A selective emitter matching this high *EQE* region would have less out-of-band radiation while maximizing the electrical power output. For wavelengths below 0.8 μm , the *EQE* of GaSb is low and the amount of radiation emitted by TPV emitters at attainable temperatures (1000-2000 K) is negligible. Therefore, the high emissivity region is set to be 0.8-1.66 μm . The emitter should have low emissivity for $\lambda > \lambda_g$. Although the bandgap of GaSb is 1.72 μm , nonzero *EQE* values are reported for JXC GaSb cells up to 1.8 μm , which might be due to bandgap shrinkage in the case of doping. With these considerations, a figure of merit (*FOM*) is defined as in Eq. (51), which is to be maximized.

$$FOM = \frac{\int_{0.8}^{1.66} \varepsilon_{\lambda}(\lambda) d\lambda}{\int_{0.8}^{1.66} d\lambda} - \frac{\int_{1.8}^5 \varepsilon_{\lambda}(\lambda) d\lambda}{\int_{1.8}^5 d\lambda} \quad (51)$$

With this *FOM*, the emissivity is expected to decrease between 1.66-1.8 μm , showing a similar trend as the *EQE* of GaSb cell. In order to prevent additional emissivity peaks, the long wavelength limit of the low emissivity region is taken as 5 μm . An objective function similar to *FOM* in Eq. (51) was previously used in the optimization of MIM emitters for GaSb cell, where the optimized emitter showed both higher efficiency and higher in-band radiation than frequently used emitters such as silicon carbide (SiC) and plain W [81].

In the design of W-SiO₂-W emitter, the bottom W layer is assumed to be optically thick, so the transmission through it is assumed to be zero. By Kirchhoff's law, for a body at equilibrium, the emissivity and the absorptivity should be equal at all wavelengths. Therefore, the spectral emissivity can be calculated using Kirchhoff's law:

$$\varepsilon_\lambda = \alpha_\lambda = 1 - \rho_\lambda \quad (52)$$

The reflectivity of the nanostructures was calculated using the FDTD method. The optical constants of W and SiO₂ are taken from Palik [58]. In Figure 3.2, the four MIM designs and the computational area of a disk MIM structure are given. In the FDTD simulations, a plane light source was assumed to be incident normal to the x - y plane. The x and y boundary conditions are periodic, since the nanostructure design repeats both in x and y directions. The z boundary conditions are set as perfectly matched layers (PML) in order to prevent reflections from the boundaries.

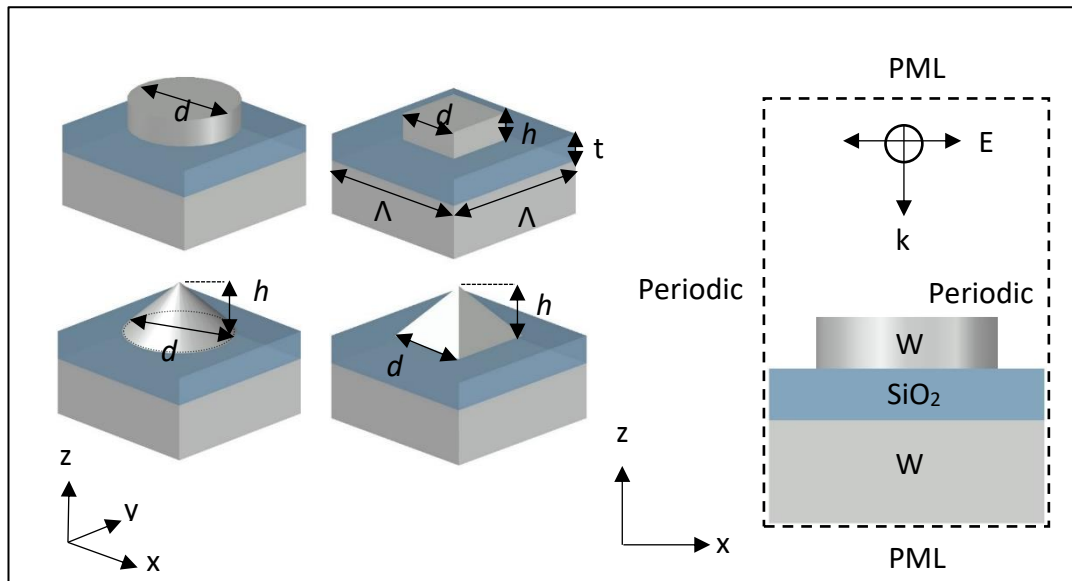


Figure 3.2. Four MIM designs and the computational area of a disk MIM structure.

For accurate results, the mesh step should be at least ten times smaller than the smallest wavelength being simulated [14]. Since wavelengths shorter than 500 nm are not in the scope of this work, the mesh step should be smaller than 50 nm. For the

mesh convergence test, the W-SiO₂-W solar absorber design of Han [42] is repeated. Figure 3.3 shows the absorptivity of the W-SiO₂-W nanostructure of Han [42] at $\lambda = 0.5 \mu\text{m}$ corresponding to different mesh steps. It is seen that the results converge to a constant value at 5 nm mesh size and decreasing the mesh size further did not improve the results.

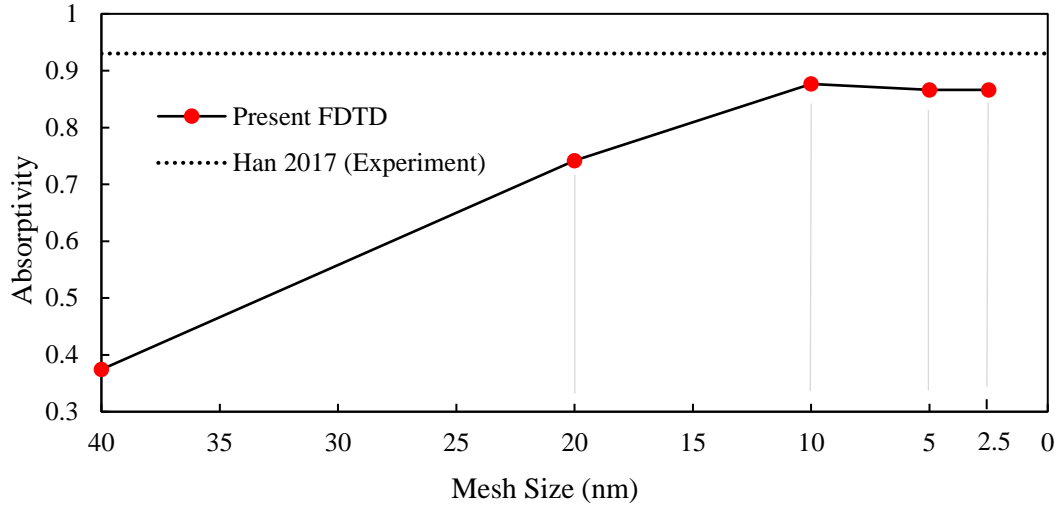


Figure 3.3. The absorptivity at $\lambda=0.5 \mu\text{m}$ of metamaterial solar absorber design of Han [42], simulated again with FDTD with varying mesh sizes.

The power output (P_{el}) is calculated from Eq. (43) which was explained in detail in Chapter 2.

$$P_{el} = FF \cdot J_{sc} \cdot V_{oc} \quad (43)$$

The efficiency is calculated by dividing power output to the total emissive power of the emitter.

$$\eta_{TPV} = \frac{P_{el}}{E_{total}} \quad (42)$$

3.1.3. Optimization

In order to obtain the emissivity profile giving maximum FOM , there are four parameters to be optimized: period (A), dielectric layer thickness (t), width (d) and height (h) of the metallic patches. The width is equated to base length for square bases

and diameter for circular bases. Wang et al. [9] studied the effects of geometric parameters of the MIM structure on the emissivity profile. It was seen that the cut-off wavelength was strongly correlated with the resonator width. Therefore, in the current work, the width is varied between 0 and the period of the structure. In the same study, the cut-off wavelength around 1.8 μm due magnetic polaritons, was not affected by changing the period between 0.5-0.8 μm . In other studies, with W-SiO₂-W designs, cut-off wavelengths between 1.57-1.83 μm were achieved for periods of 0.5-0.6 μm [35, 42, 46, 47]. In this chapter, three period values of 0.4, 0.6 and 0.8 μm are considered. Wang et al. [9] considered the thickness of the spacer layer to vary between 30-150 nm in their work. It is seen that the peak maximum absorptivity was increased with SiO₂ thickness up to 80 nm, but decreased with further SiO₂ thickness increase. Khorrami [47] showed that the emissivity was enhanced gradually by increasing the thickness of the SiO₂ layer from 30 nm to 110 nm. In the present work, the SiO₂ thickness limits are set as 0-200 nm. Finally, the height of the W resonators is varied between 0-500 nm, considering fabrication requirements.

Within the scope of this Chapter, PSO works are performed separately for each period. The solution space is three dimensional with the parameters t , d , and h . For each optimization, 20 random particles are generated initially. These particles are moved through the solution space for 10 generations, and evaluated according the FOM given in Eq. (51).

3.1.4. Results and Discussion

In order to design efficient TPV emitters, geometric parameters of MIM structures with four different resonator shapes were optimized. In Figure 3.4., a sample PSO optimization graph is given for the disk resonator of period 0.4 μm . The FOM converged at 9th generation. The remaining FOM vs generation plots were not included for simplicity.

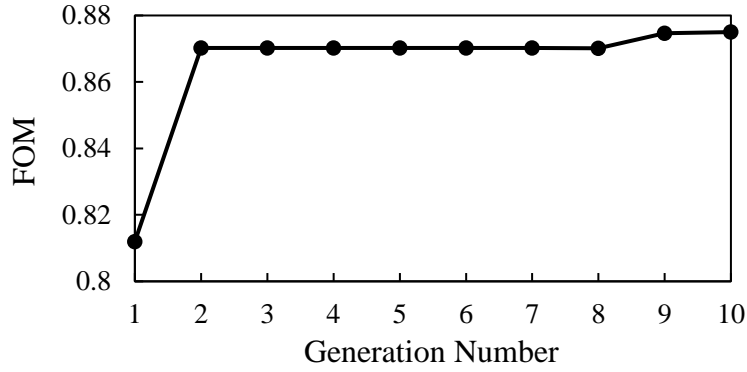
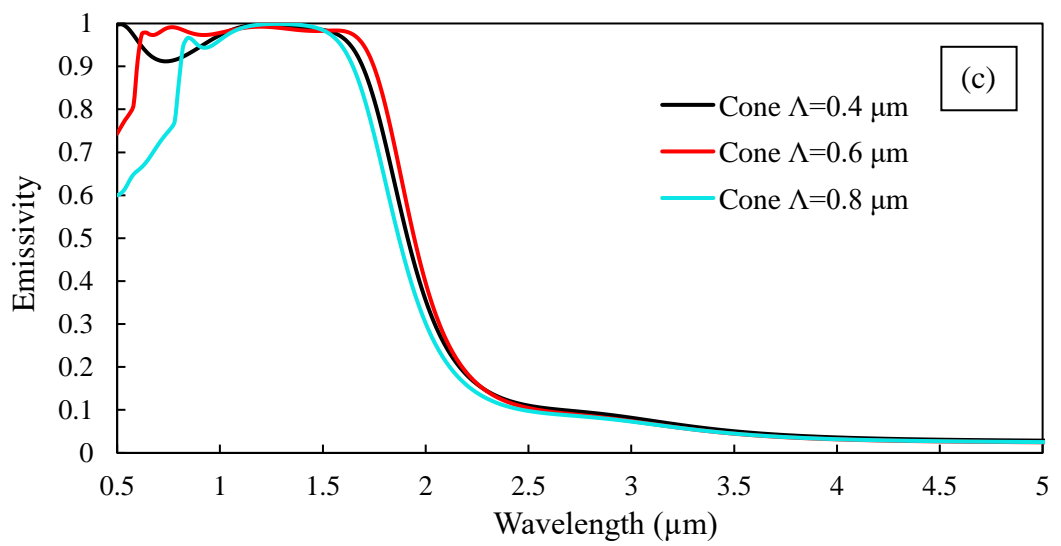
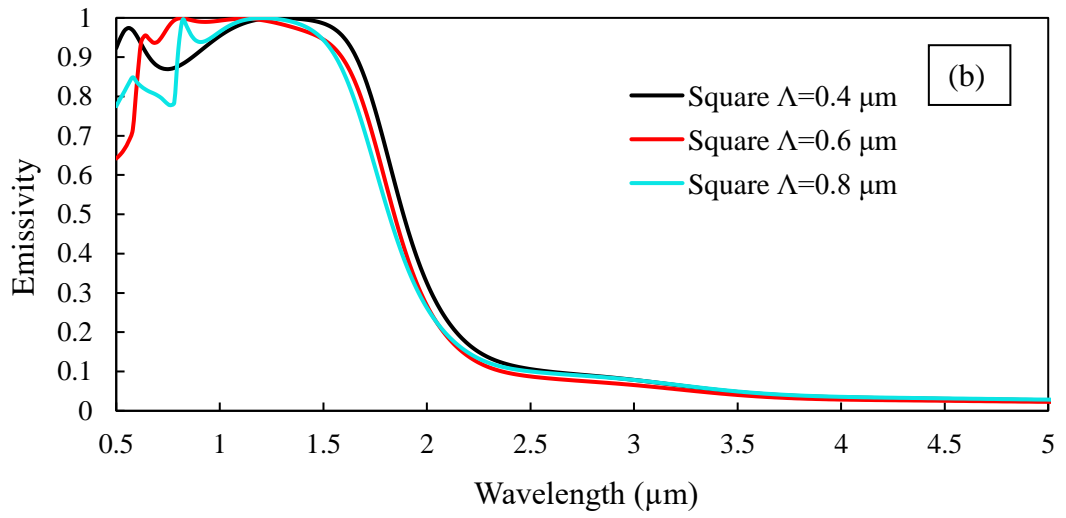
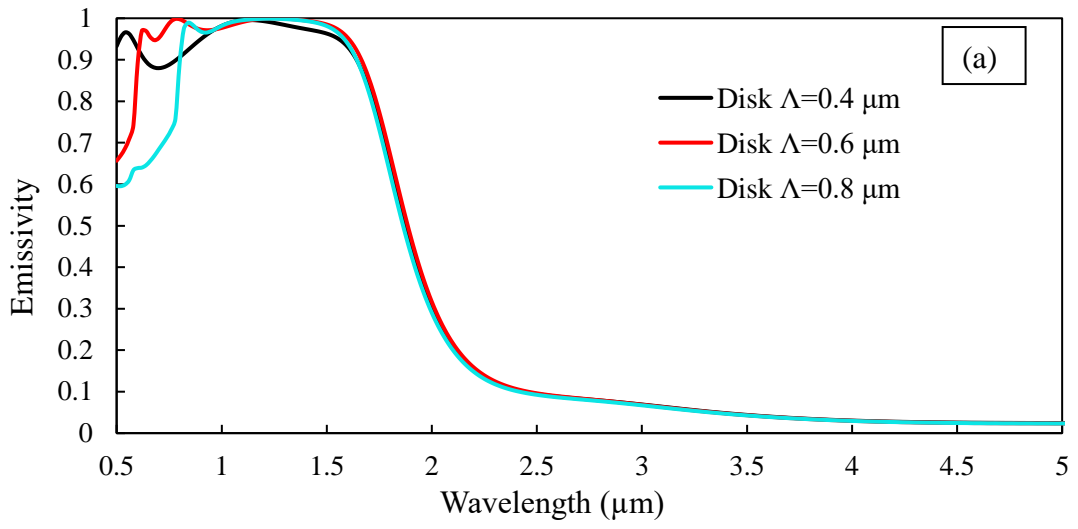


Figure 3.4. FOM vs generation number for disk resonator of period 0.4 μm .

The optimum parameters found by PSO and the corresponding *FOM* values are presented in Table 3.1. None of the optimized parameters converged into parameter limits, which indicates there is a maximum within the specified boundaries. It is seen that the optimized SiO₂ thickness is proportional to the period of the structure. A similar result is observed with the optimum resonator widths, but not with the optimum heights. The emissivity spectra of MIM emitters with the parameters in Table 3.1 are shown through Figure 3.5 a-d.

Table 3.1. Optimized nanostructure parameters and corresponding FOM values

Resonator Shape	Period (μm)	SiO ₂ Thickness (nm)	Resonator Height (nm)	Resonator Width (nm)	<i>FOM</i>
Disk	0.4	70	59	258	0.875
	0.6	114	50	314	0.891
	0.8	140	61	337	0.891
Square	0.4	69	79	220	0.830
	0.6	117	50	250	0.866
	0.8	183	100	276	0.867
Cone	0.4	69	205	281	0.870
	0.6	108	154	339	0.877
	0.8	143	217	365	0.879
Pyramid	0.4	50	290	251	0.837
	0.6	95	252	285	0.881
	0.8	131	315	302	0.875



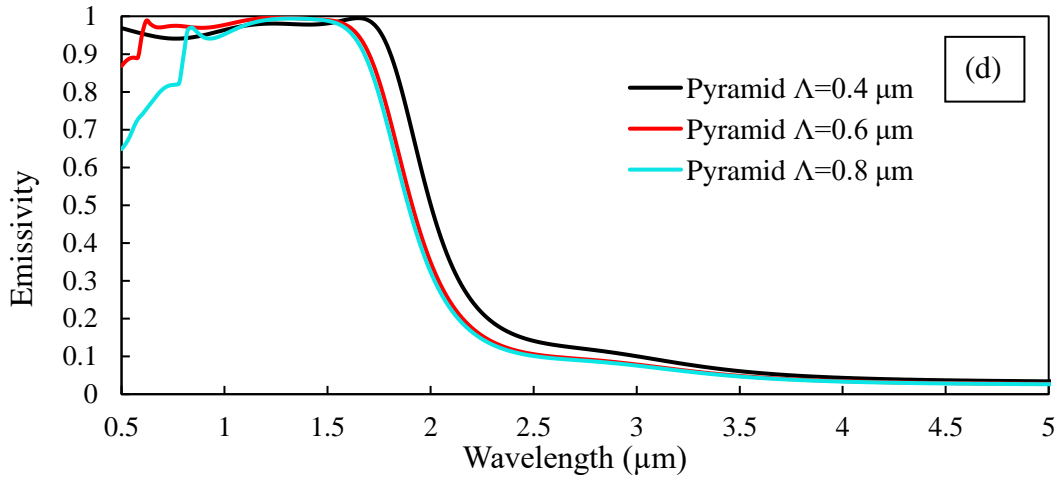


Figure 3.5. The spectral emissivity of MIM emitters with periods 0.4-0.6 μm . (a) Disk (b) Square (c) Cone and (d) Pyramid resonators.

In Figure 3.5, the emissivity peak at short wavelength is strongly correlated with the periodicity, regardless of the shape. This indicates that the peaks around 0.5-0.9 μm is due to the resonance of surface plasmon polaritons (SPP). On the other hand, the peaks at the long wavelengths ($\lambda_{cut-off}$) do not have such a relation. This can be explained by the magnetic polariton (MP) resonance, which depends on the resonator width rather than period [32]. It appears that, by choosing smaller periods, the SPP resonance can be shifted towards shorter wavelengths. However, choosing $\Lambda = 0.4$ μm results in a dip around 0.7 μm .

In order to compare the effect of resonator shape on the emissivity, the emissivity spectra of different emitters are plotted in Figure 3.6 (a-c) for the same periods. The peak between 0.5-0.9 μm did not show any noticeable change with the resonator shape. However, it is noticed that the pyramid and cone resonators showed a broader emissivity peak towards longer wavelengths compared to square and disk ones, for all periods.

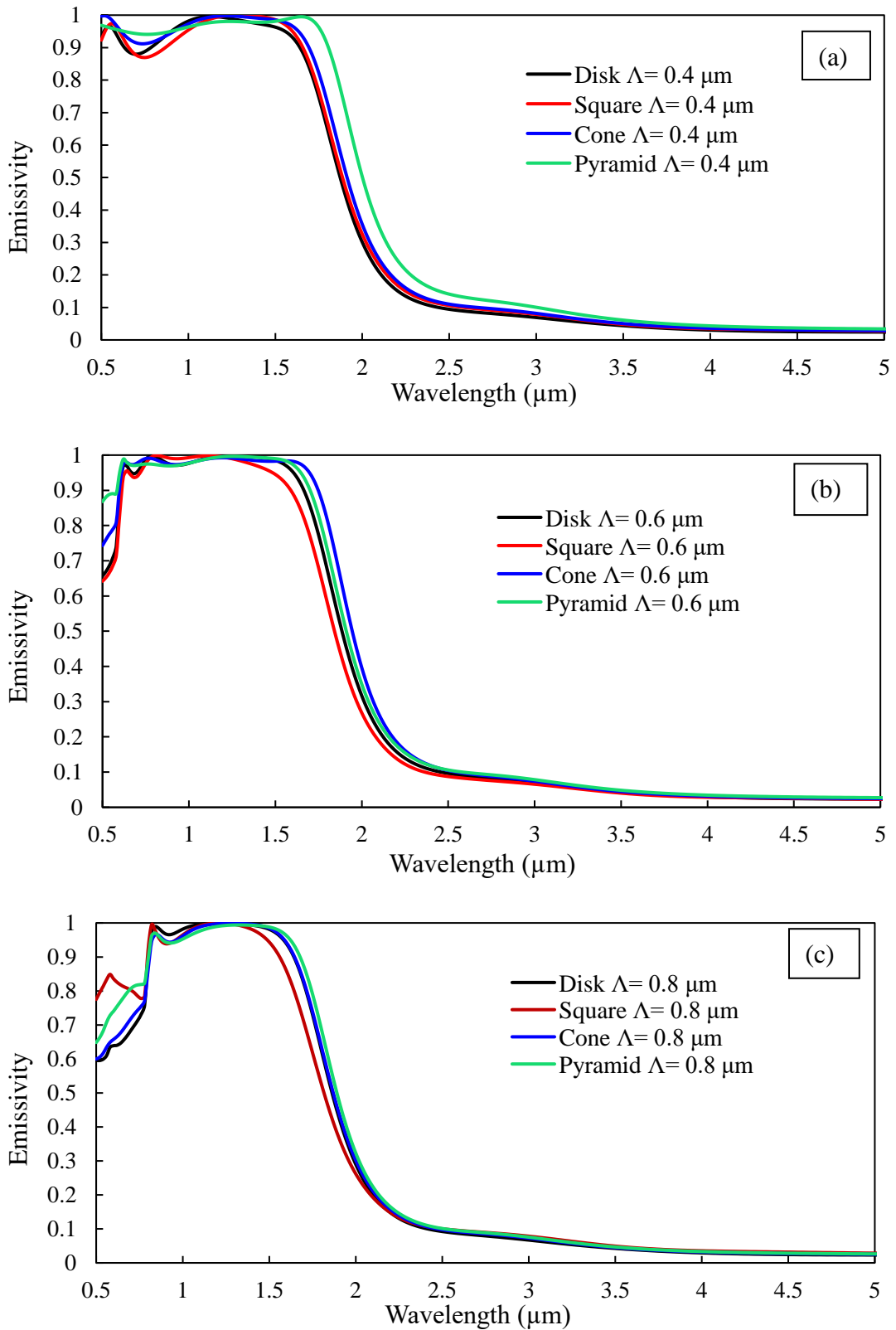


Figure 3.6. Comparison of the emissivity spectra of MIM emitters with different shapes for periods (a) $0.4 \mu\text{m}$ (b) $0.6 \mu\text{m}$, and (c) $0.8 \mu\text{m}$.

3.1.5. Performance Evaluations

The emitter efficiency, TPV efficiency and power output at 1700 K are given in Table 3.2 for 12 optimized emitters, blackbody, SiC and the ideal emitter. SiC as an emitter is frequently paired with low bandgap TPV cells such as GaSb in the experimental TPV prototypes due to its broadband high emissivity [80]. In this chapter, SiC is approximated as a graybody emitter with $\varepsilon = 0.85$ [2]. The emissivity spectrum of the ideal emitter is given Eq. (50) with $\lambda_g = 1.8 \mu\text{m}$ to cover all of the wavelength range with nonzero quantum efficiency.

Table 3.2. The emitter efficiency, TPV efficiency and power output for emitters at 1700 K paired with GaSb cells

Emitter	Period (μm)	η_E	$P_{el} (\text{W cm}^{-2})$	η_{TPV}
W-SiO ₂ -W Disk	0.4	76.40%	3.693	22.37%
	0.6	76.21%	3.767	22.32%
	0.8	77.03%	3.724	22.67%
W-SiO ₂ -W Square	0.4	74.98%	3.743	22.03%
	0.6	77.77%	3.622	22.73%
	0.8	76.57%	3.561	22.50%
W-SiO ₂ -W Cone	0.4	73.93%	3.788	21.63%
	0.6	73.48%	3.831	21.38%
	0.8	76.14%	3.727	22.42%
W-SiO ₂ -W Pyramid	0.4	68.75%	3.841	19.95%
	0.6	74.48%	3.808	21.77%
	0.8	75.30%	3.761	22.11%
SiC	-	28.65%	3.303	8.21%
Blackbody	-	28.65%	3.925	8.29%
Ideal Emitter	-	100.00%	3.925	28.93%

In Table 3.2 it is observed that on average, η_{TPV} is less than 30% of η_E , which means that most of the in-band radiation does not contribute to the electrical power. This loss can be attributed to thermalization, surface recombination, and other intrinsic cell losses. At 1700 K, it is seen that the optimized emitters yield 7.8-16.3% higher power outputs while being 143-177% more efficient than SiC emitter. Among the selective emitter designs, the highest TPV efficiency (shown as bold in Table 3.2) is obtained with the square resonator of period 0.6 μm , while the highest power output is obtained from pyramid resonator with of period 0.4 μm . Among flat and pointy

resonators of the same base shape and period, the highest relative efficiency difference of 10.43% is observed between square and pyramid emitters of period 0.4 μm . Similarly, the highest increase in the power output of 5.62% is seen between pyramid and square emitters of period 0.8 μm . On average, the disk and square resonators seem to have higher efficiencies than cone and pyramid resonators. However, cone and pyramid resonators outperform disk and square ones in terms of the power output. This can be explained by the broadening of high emissivity region towards longer wavelengths in pointy resonators. The shifting of $\lambda_{cut-off}$ towards higher wavelengths adds to the power output, but reduces the efficiency due to increased out-of-band radiation. For further comparisons, the configuration with the highest efficiency, that is W-SiO₂-W emitter with square resonator of period 0.6 μm is selected. In Figure 3.7, the efficiency of this emitter, the ideal emitter, and the blackbody emitter in the temperature range 1000-1800 K is presented. In Figure 3.8, the power outputs at different emitter temperatures are plotted for the selective emitter and blackbody emitter.

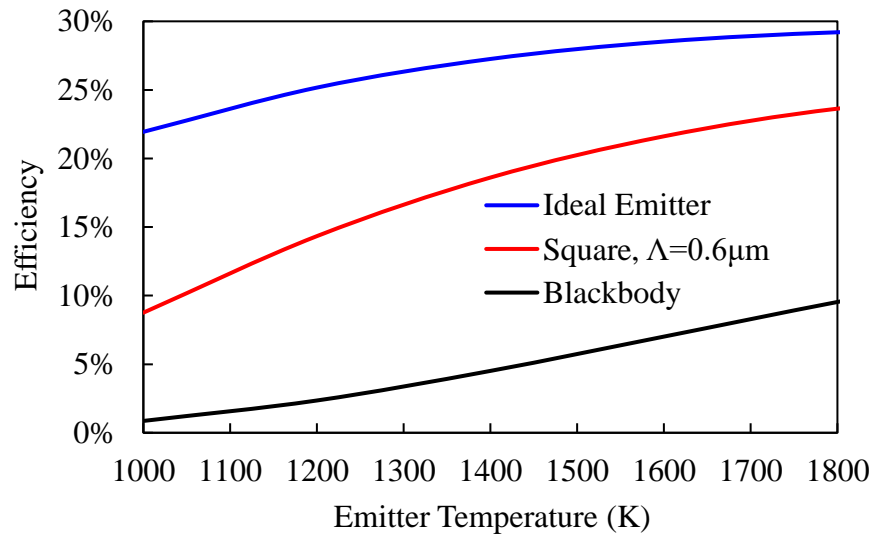


Figure 3.7. TPV system efficiencies for the MIM emitter, the ideal emitter and the blackbody emitter in the range 1000-1800 K.

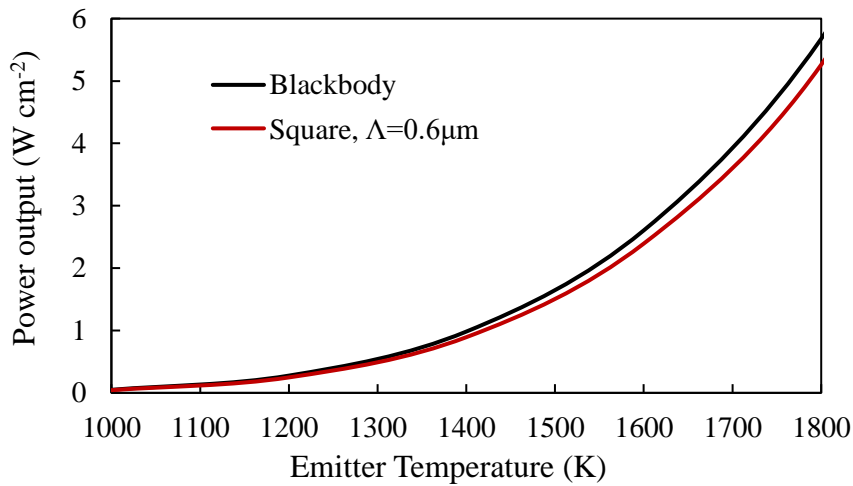


Figure 3.8. The power outputs from TPV systems with the selective emitter and blackbody at different temperatures

Between emitter temperatures of 1000-1800 K, the most efficient emitter has a power output that is about 88-93 % of that of a blackbody. The efficiency is 2.5-10 times of that of the blackbody emitter and within 40-80 % of the ideal emitter. The efficiency values obtained by ideal, selective, and the blackbody emitters tend to get closer as the temperature increases. This can be explained by the shifting of the peak emissive power towards lower wavelengths, according to Wien's Displacement Law. With increased temperature, the ratio of in-band radiation to the total emissive power increases for all emitters considered. It should be noted that the ideal emitter does not represent the ultimate attainable efficiency with a predetermined cell. A narrowband emitter may be more efficient, but the power output would be much smaller compared to broadband emitters at the same temperature. Efficiency estimates of TPV systems with JXC GaSb cell matched with hypothetical narrowband emitters can be found in Sakurai [46].

3.1.5.1. High Temperature Adjustments on Emissivity

Up to now, the optimizations and performance analyses were carried out based on the optical properties (n, k) of W measured at room temperature [58]. It is empirically known that the spectral emissivity of W changes with the temperature [82].

Measuring optical properties at high temperatures is a challenging task, however, indirect methods can be used to calculate the optical properties at high temperatures. Roberts [83], measured dielectric constants of W at 1100 K and 1600 K in the wavelength range 0.365-2.65 μm and fitted parameters to the Drude model. The fitted parameters are extrapolated to 2000 K and 2500 K as well. The refractive indices (n , k) obtained from the model are used in FDTD simulations to predict the high temperature emissivity spectra of the selective emitter. Figure 3.9 shows the emissivity spectra of the square W-SiO₂-W emitter of period 0.6 μm , at 300 K, 1100 K and 1600 K.

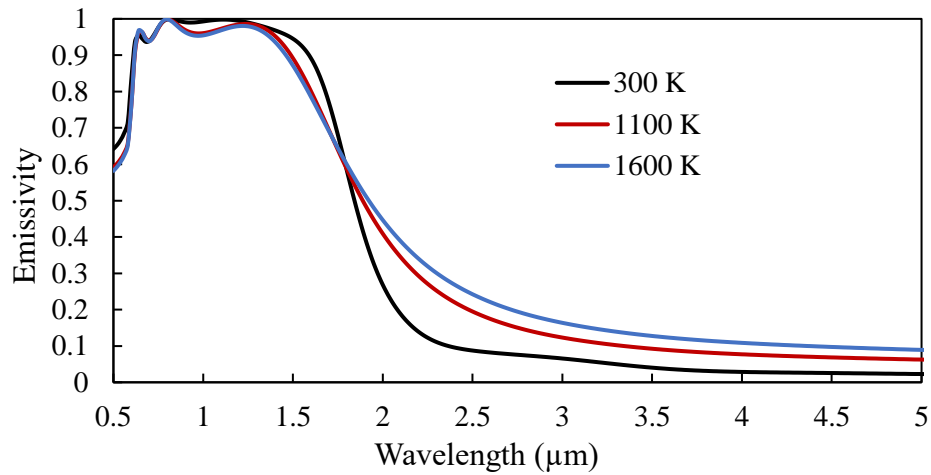


Figure 3.9. The emissivity spectra of square W-SiO₂-W emitter of period 0.6 μm , at different temperatures.

Based on the emissivity spectra of 1100 K and 1600 K, the emissivity spectra at other temperatures are calculated by linear interpolation. The efficiency and power outputs adjusted to the emissivity change at high temperatures are presented in Table 3.3. From the table it is seen that the temperature adjusted power outputs decreased by 5.8-6.2% and the efficiencies are 20-38% lower compared to the values predicted by constant emissivity assumption. The slight difference in the power output can be explained by the decrease in the emissivity spectra below 1.8 μm . The resonant wavelengths seem not to be affected by the temperature which keeps the in-band radiation high. On the other hand, the emissivity after 1.8 μm increases with temperature which creates more out-of-band radiation and decreases efficiency.

Nevertheless, the efficiencies at high temperatures are still 2-6 times that of the graybody emitters, such as SiC.

Table 3.3. The efficiency and power output of the square W-SiO₂-W emitter of period 0.6 μm , constant emissivity vs emissivity adjusted to high temperatures

T (K)	Constant Emissivity		Emissivity Adjusted to Temp.	
	P_{el} (W cm ⁻²)	η_{TPV}	P_{el} (W cm ⁻²)	η_{TPV}
1000	0.043	8.76%	0.040	5.43%
1200	0.248	14.34%	0.232	9.59%
1400	0.893	18.61%	0.837	13.37%
1600	2.393	21.62%	2.245	16.39%
1800	5.261	23.63%	4.940	18.74%

3.2. Design and Optimization of Tantalum-Hafnia-Tantalum (Ta-HfO₂-Ta)

Emitter Matching Silicon Cell

3.2.1. Material

Although silicon cells are inexpensive and readily available, their use in TPV systems is limited due to their high bandgap ($E_g = 1.1\text{eV}$ [8]). According to Wien's Displacement Law, in order match the peak emission of a blackbody emitter with the bandgap of Si, it should operate around 2630 K. On the other hand, for low bandgap semiconductors such as GaSb ($E_g = 0.72\text{ eV}$ [12]), this temperature is 1680 K, which is easier to achieve. Hence, majority of the studies on developing TPV systems focus on low bandgap cells such as GaSb [44, 46, 84]. The main disadvantages of GaSb cells are their high cost and toxicity [85]. On the other hand, Si cells are relatively inexpensive and non-toxic. Although the performance of low bandgap TPV cells are superior to Si cell at low temperatures, the cost of Si cell can compensate for its low efficiency. Fraas [86] compared TPV combined heat and power systems with Si and GaSb cells. The cost of electricity generated was projected to be 10 cents/kWh for GaSb and 7.3-10.7 cents/kWh for Si cells. In [86], GaSb cell is paired with AR coated W emitter and Si cell is paired with ytterbia (Yb₂O₃) emitter. Although it is challenging to match the peak blackbody emission with the bandgap of Si cell, selective emitters can be utilized to match the peak emission at lower temperatures.

Previously, metal-insulator-metal (MIM) configurations were used to design metamaterial TPV emitters to match their emissivity with low bandgap TPV cells such as GaSb [44, 46], InGaAs [36] and InGaSb [35]. However, to the best of the author's knowledge, there has not been a MIM emitter designed to be paired with Si cells. In order to design a MIM emitter suitable for Si cell, the base metal should meet two elementary requirements: High melting point and low emissivity (or high reflectivity) in the out-of-band range of Si ($\lambda > 1.1 \mu\text{m}$). Refractory metals such as W and Ta are suitable to be used in TPV applications due to their excellent resistance to heat and high melting temperatures. Previously, W and Ta have been used to design selective TPV emitters [30, 34, 87]. Ta has the higher reflection in the range $\lambda > 1.1 \mu\text{m}$ compared to W, hence it is more suitable for an emitter aimed to match the Si cell. In MIM structures, weakly absorbing oxides such as SiO₂ [34, 46], Al₂O₃ [36, 38] and HfO₂ [44] were previously used in the design of TPV emitters. Among aforementioned dielectrics, HfO₂ has the highest melting temperature (3053-3083 K [88]). For TPV applications, in addition to a high melting temperature, the insulator material should have a thermal expansion coefficient (α) that is compatible with the base metal to prevent delamination. HfO₂ has an α of 5.8-6.5 $\mu\text{m}/\text{m}$ [88], which is similar to that of Ta ($\alpha = 6.3 \mu\text{m}/\text{m}$ [89]). In [90], a thermal emitter made from multiple HfO₂ and W thin layers was demonstrated to work without delamination at 1273 K. The thermal expansion coefficient of HfO₂ is closer to that of Ta than W ($\alpha = 4.3 \mu\text{m}/\text{m}$ [89]), therefore an emitter with Ta-HfO₂ layers can be expected to be stable as well. In Wang [91], it was observed that the shape of Au nanoparticles in a MIM structure changed into rounder shapes upon heating. In order to prevent a similar effect, the shape of metallic resonators is chosen as disks. Hence, this part of the thesis is aimed at designing MIM emitters based on Ta metallic layer, HfO₂ spacer, and periodically spaced Ta nanodisks to be paired with Si cells, by independently optimizing the nanostructure parameters. For high thermal stability, a modified design with nanodisks coated with a thin HfO₂ layer is also presented. The efficiency and power outputs of the emitters were calculated and compared to blackbody and Yb₂O₃ emitters.

3.2.2. Method

A unit cell of the MIM emitter design is presented along with the computational area in the Fig. 3.10, where Λ is the period, t is the thickness of the HfO_2 layer, h is the height and d is the diameter of the Ta nanodisks.

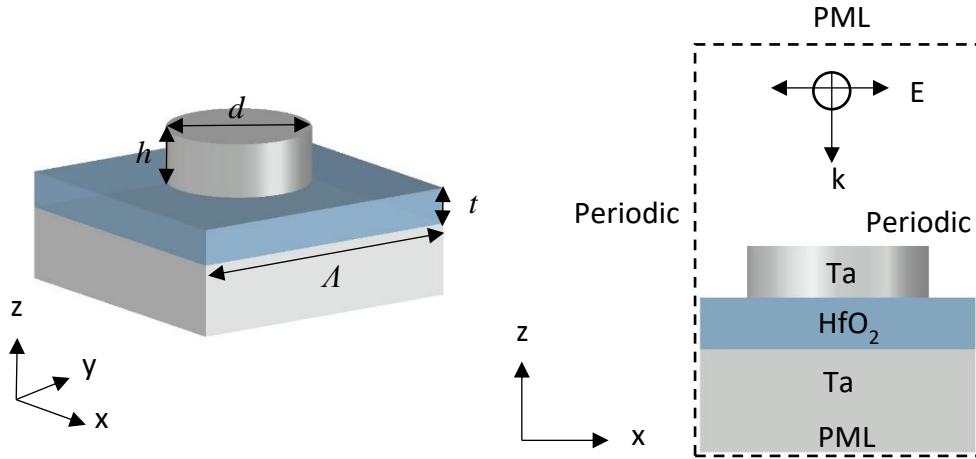


Figure 3.10. The schematic and design parameters of the proposed MIM emitter

In the MIM design, the Ta substrate is assumed to be sufficiently thick, and therefore opaque to visible and IR light. For a body at thermal equilibrium, the emissivity and absorptivity should be equal to each other at all wavelengths by Kirchhoff's Law. The reflectivity of the nanostructure is obtained by numerically solving Maxwell's equations via FDTD. In the simulations, the optical properties of HfO_2 and Ta are taken from Al-Kuhaili [92] and Palik [58], respectively. The nanostructure is illuminated by a plane wave source incident normally to the x - y plane. The z boundary conditions are set up as PML, while x and y boundary conditions are set as periodic. A mesh independence test with a convergence yielded mesh step of 5 nm is sufficient and this value is used throughout the simulations.

For designing a selective emitter, the external quantum efficiency (EQE) of the cell should be taken into account. EQE indicates how efficiently the incident radiation is used to generate electricity. The EQE of crystalline silicon (c-Si) solar cells produced UNSW [93] is shown in Fig 3.11.

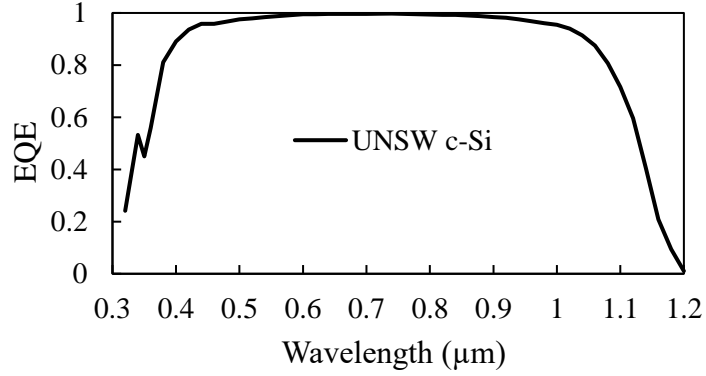


Figure 3.11. External quantum efficiency of the UNSW c-Si cell

Although the bandgap of Si is 1.1 μm , it is seen that non-zero EQE values up to 1.2 μm is present. This is due to the bandgap shrinkage resulting from doping. Therefore, the emissivity of the emitter should be high up to 1.2 μm to maximize the power output from the TPV system. Si has considerable EQE in the range 0.3-0.5 μm , however, in this range the portion of thermal radiation emitted by a blackbody at 1000 - 2500 K is negligible. Therefore, the short wavelength limit of the in-band radiation can be fixed to 0.5 μm for optimization. In order to eliminate the additional peaks after 1.2 μm , the long wavelength limit of out-of-band radiation region can be defined as 5 μm . A simple FOM to increase in-band radiation and suppress the out-of-band radiation is defined in Eq. (53).

$$FOM = \frac{\int_{0.5}^{1.2} \varepsilon_{\lambda}(\lambda) d\lambda}{\int_{0.5}^{1.2} d\lambda} - \frac{\int_{1.2}^5 \varepsilon_{\lambda}(\lambda) d\lambda}{\int_{1.2}^5 d\lambda} \quad (53)$$

3.2.3. Optimization

The desired emissivity spectrum can be obtained by adjusting the four parameters of the unit cell; period (A), spacer thickness (t), height (h), and diameter (d) of the nano disks. Previous MIM studies have shown that the magnetic polariton (MP) resonance occurred at wavelengths longer than the surface plasmon polariton resonance, effectively determining the cut-off wavelength of the high emissivity region. The location of the MP is strongly related to the resonator width [32, 39, 94] which is bounded by the period of the unit cell. In order to determine the period, previous MIM

designs with similar selectivity are investigated. Although there are not any MIM selective emitters that are designed to match the bandgap of Si, there are MIM solar absorber designs with similar cut-off wavelengths. Chen [45] designed a MIM solar absorber with period of 200 nm, by using Ni for metal layers and SiO₂ for the dielectric spacer. Absorptivity over 95% was observed up to 1180 nm. Dang [50] designed a metamaterial emitter with TiN-SiO₂-Ti structure with periodicity 200 nm which showed high absorption (98%) between 391-1171 nm. In this part of the thesis, the period is set to be 200 nm as well.

In order to find the t , h , and d values giving the maximum FOM , the PSO algorithm is used together with the FDTD. In the optimization, d is varied between 0 - 200 nm, the t is varied between 0 – 100 nm, and the h is varied between 0 – 200 nm. In the parameter space, 10 random combinations of t , d , and h are generated for the initial run. The emissivity spectra of these combinations are computed with FDTD and assigned a value by the figure of merit. The candidate solutions are moved through the solution space for 10 iterations.

3.2.4. Results and Discussion

The PSO algorithm converged to $FOM = 0.815$ at 5th iteration with the following nanostructure parameters: $d = 54$ nm, $h = 37$ nm, and $t = 75$ nm. The result of the PSO algorithm is presented in Figure 3.12.

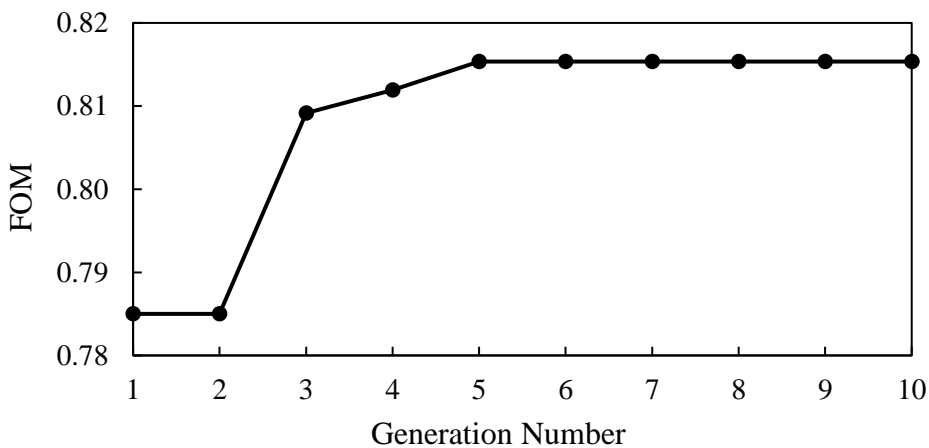


Figure 3.12. FOM vs generation number in PSO algorithm

The emissivity of the optimized MIM emitter is shown in Fig 3.13, compared to Ta with 37 nm-thick HfO₂ film and plain Ta. It can be seen that although the presence of HfO₂ film increases the emissivity, the enhancement is mostly due to the presence of Ta nanodisks.

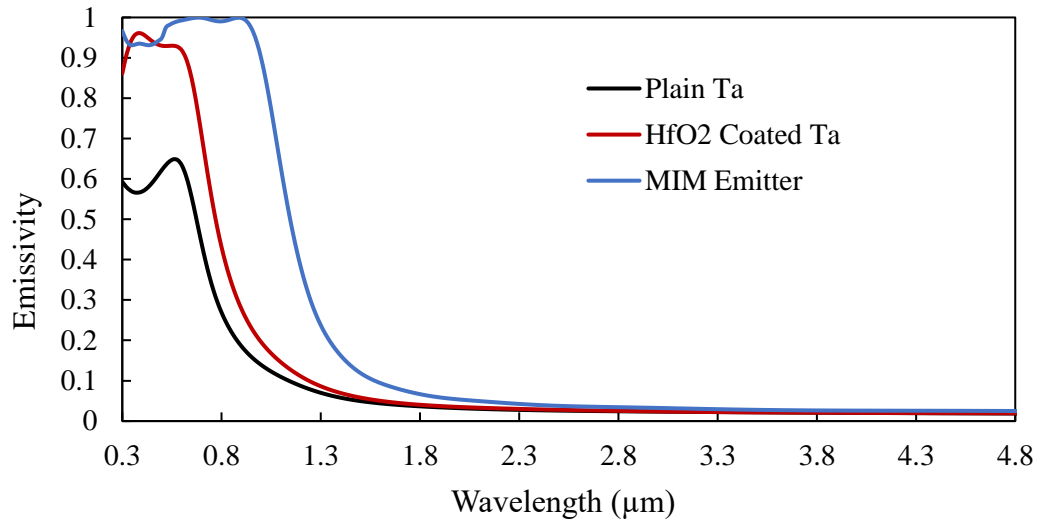


Figure 3.13. Emissivity spectra of the plain Ta, Ta with 37 nm HfO₂ coating and the MIM emitter

Previous studies showed that nanostructures can be deformed at high temperatures [19, 91]. Coating the nanostructured surface with an additional ceramic was shown to increase the thermal stability. In [95], heating of a nanostructured W emitter resulted in destruction of the nanostructures at 1273 K, however, when a 25 nm HfO₂ coating is applied, the emitter remained stable at 1473 K. Arpin [96] fabricated a W inverse opal photonic crystal as a narrow band emitter. It is seen that, coating the structure with Al₂O₃ increased the stability up to 1273 K, whereas using HfO₂ increased stability up to 1673 K. Rinnerbauer [28] fabricated a TPV emitter made by Ta photonic crystal and coated it with a thin HfO₂ layer. After annealing at 1173 K for 6 days (144 hours), no degradation was noticed. Stelmakh [87] reported that the Ta emitter with HfO₂ coating was stable at 1373 K with no sign of deterioration, suggesting that the structure should be stable at higher temperatures, as well. In order to increase the thermal stability and prevent the formation of tantalum carbide, the Ta nanodisks in MIM emitter can be coated with a 25 nm of HfO₂. In order to keep the

distance between nanodisk structures, the period is increased from 200 nm to 250 nm. The schematic of this coated MIM emitter design is shown in Figure 3.14, along with the emissivity spectra of the coated MIM emitter, MIM emitter, and the ideal emitter. The ideal emitter has the cut-off wavelength of 1.2 μm to ensure maximum power output.

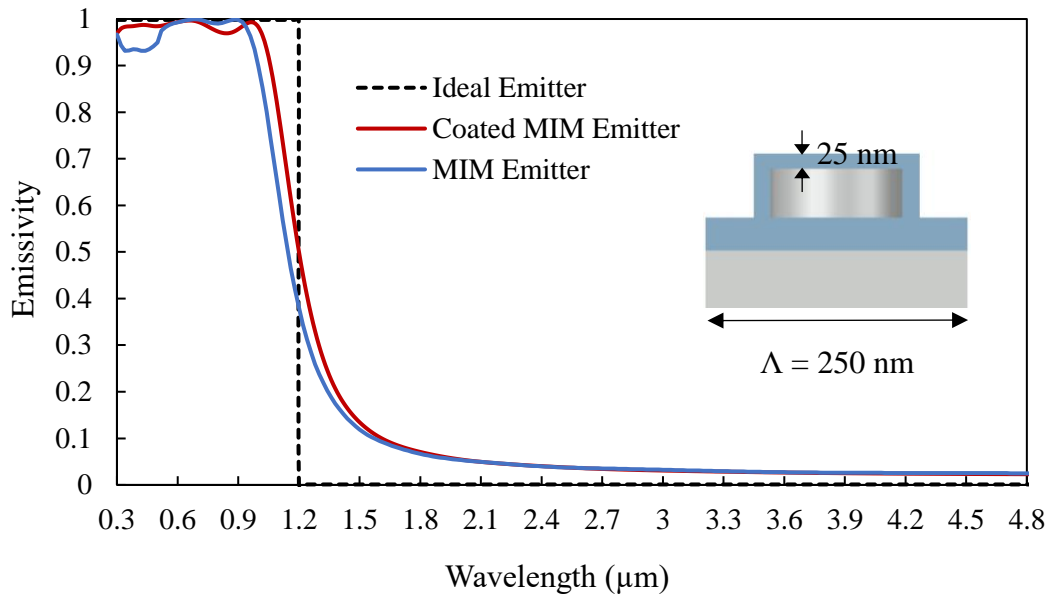


Figure 3.14. The schematic of coated MIM emitter, and the emissivity spectra of MIM emitter, coated MIM emitter and ideal emitter

3.2.5. Performance Evaluations

The power and efficiency calculations were performed in the wavelength range of 0.3-10 μm . Table 3.4 shows the emitter efficiency, power output and TPV system efficiency of the MIM emitter, HfO_2 coated MIM emitter, Yb_2O_3 and ideal emitter.

Table 3.4. Emitter efficiency, power output and TPV system efficiency of the MIM emitter, HfO_2 coated MIM emitter, Yb_2O_3 and ideal emitter

Emitter	Period (nm)	η_E	P_{el} (W cm^{-2})	η_{TPV}
MIM	200	63.98%	4.395	28.57%
Coated MIM	250	63.54%	4.755	27.91%
Yb_2O_3	-	38.78%	2.537	18.21%
Ideal	-	100.00%	5.185	41.49%

In Figure 3.15, the efficiency of the TPV systems with Si cell and the selective emitters, Yb_2O_3 , ideal emitter and blackbody are plotted for emitter temperatures 1000-2500 K. Table 3.5 shows the electrical power outputs for TPV systems with Yb_2O_3 emitter, selective emitters, and the blackbody emitter at temperatures 1000-2500 K, paired with Si cells. For power and efficiency calculations, the emissivity of Yb_2O_3 is taken from Bitnar [97]. In Figure 3.15, it is seen that the efficiencies of coated and uncoated MIM emitters are similar, however as seen from Table 3.5, the power output of the coated MIM emitter is 6-17% higher than uncoated MIM emitter. The difference in power can be explained by the higher emissivity of the coated emitter between wavelengths 0.94-1.2 μm . The coated emitter has also higher emissivity after 1.2 μm , which increases its the out-of-band radiation. From Fig 3.5, it is seen that the Yb_2O_3 emitter is more efficient than a blackbody emitter due to its narrow emission peak around 1 μm . However, as evident from Table 3.5, the power output of Yb_2O_3 is 44-55% of that of the blackbody at the same temperature. Between 1000-2500 K, the coated MIM emitter can provide 55.7-113.7% more electrical power than Yb_2O_3 emitter while being 19-99.5% more efficient. The difference in efficiency is larger at lower temperatures.

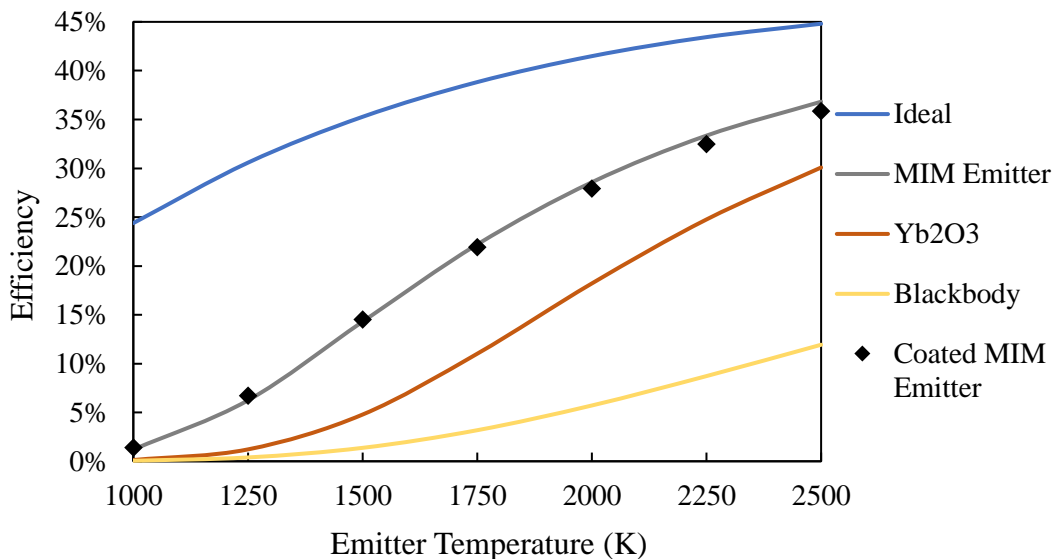


Figure 3.15. Efficiency of TPV systems with Si cell paired with MIM emitters, Yb_2O_3 and blackbody

Table 3.5. Electrical power outputs from TPV systems with Si cells paired with selective emitters, Yb₂O₃ and blackbody

T (K)	Power Output (W cm ⁻²)			
	MIM	Coated MIM	Yb ₂ O ₃	Blackbody
1000	0.0021	0.0025	0.0016	0.0029
1250	0.0415	0.0472	0.0292	0.0541
1500	0.3157	0.3521	0.2100	0.3949
1750	1.3981	1.5330	0.8683	1.6920
2000	4.3952	4.7550	2.5368	5.1847
2250	10.9685	11.7397	5.8725	12.6784
2500	23.2458	24.6665	11.5434	26.4336

CHAPTER 4

DESIGN AND OPTIMIZATION OF NANOSTRUCTURED SILICON THERMOPHOTOVOLTAIC CELLS

A PV cell works best when all the absorbed photons have energies greater than or equal to its bandgap. The thickness of Si PV cells ranges from 200 μm to 500 μm to ensure proper absorption. However, Si reflects more than 30% of incident radiation in the IR range. Therefore, reducing reflectivity is crucial for increasing the number of absorbed photons with sufficient energies. Typically, Si cells are patterned with micro surface structures to reduce reflection. Pyramidal surface structures have been the most common choice for texturing Si solar cells due to their light trapping properties. However, their size is on the order of 1-10 μm [98, 99] and additional coatings or smaller texturing are employed to reduce reflectivity below 10% [100]. Developments in nanoimprinting techniques made it possible to fabricate nanometer sized surface structures. Several nanostructures have been proposed including nanoholes [31, 101], nanorods [13, 102], pyramids [103, 104], inverted pyramids [25], hexagonal gratings [105], triangular and rectangular grooves [106, 107, 108]. By using nanostructures, it was shown that a reflectivity as low as 0.1% can be achieved [13]. These studies are mostly focused on solar PV and aimed to reduce reflectivity for a wide range of wavelengths, mostly in the visible range (0.3-0.7 μm). In fact, well established efficient solar cells with broadband low reflectivity are available such as UNSW Si cell. However, this broadband approach may present a disadvantage for Si cells used in TPV systems. In a PV cell, when photons of $E > E_g$ are absorbed, although contributing to electricity generation, cause thermalization (i.e., excess energy of absorbed photons dissipated as heat). Since the source of thermal radiation in TPV systems is physically much closer to the cell than solar PV systems, the amount of thermalization and heating are also much larger. Temperature rise is a substantial contributor to the loss of efficiency in TPV cells, and requires additional cooling measures. In order to limit thermalization, the cell can be tailored

to have low reflectivity in a narrow region close to its bandgap and high reflectivity otherwise. Figure 4.1 shows the broadband low reflectivity employed in the literature and the narrowband low reflectivity approach suggested in this chapter.

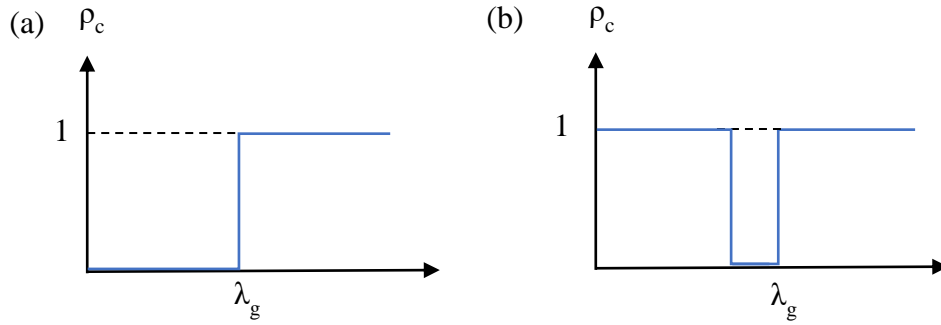


Figure 4.1. (a) Broadband low reflectivity (b) Narrowband low reflectivity

Reflecting any in-band photon may be considered as a loss of power for a solar PV system. However, in a TPV system, the reflected photons are reflected back to the emitter (photon recycling) and raise the emitter temperature. This temperature raise works in favor of improving the efficiency of the TPV system. In this Chapter, it is aimed to develop selective Si cells which absorb strongly around its bandgap and reflect otherwise. This way, the absorption of useful light can be increased while keeping the unwanted heating. Previously, nanoholes and nanorods showed good antireflective properties, but they cause high surface recombination rates due to substantial increase in the surface area [109]. Triangular structures create less increase in the surface area compared to rectangular ones with the same depth. Rectangular structures with low height can also be considered in order to limit the area increase. In this Chapter, to obtain spectral selectivity, firstly one-dimensional periodic structures of triangular, v-groove, and rectangular gratings are studied. Then, square based pyramids and nanopillars are investigated. By optimizing two independent parameters (width and depth) of the nanostructures, it is shown that the reflectivity can be minimized for the wavelength of interest, resulting in a narrow band absorption peak. The designed Si cells are compared to flat Si and nanopillar design of Sai [21], which shows broadband low reflectivity, in terms of absorbed, usable and thermalized radiation. Since this chapter uses a simplified cell model,

realistic power and efficiency calculations that require the measurement of *EQE* of the cell were not attempted. In order to calculate the maximum amount of usable and thermalized radiation, Si cells are paired with a blackbody emitter instead of selective emitter designs such as presented in Chapter 3. The main mechanism behind the reflectivity reduction in this chapter is diffraction.

4.1. Modeling of a Silicon Cell

A silicon cell can be modeled as a 300 μm thick Si wafer with an Ag back reflector. Additional coatings and passivation layers are not considered in the simplified model, to study AR effects of surface structures more clearly. The front and back reflections, denoted by ρ_1 and ρ_2 , are calculated by Fresnel equations for normal incidence, for air-Si; and Si-Ag boundaries, respectively.

$$\rho = \left| \frac{\tilde{n}_1 - \tilde{n}_2}{\tilde{n}_1 + \tilde{n}_2} \right|^2 \quad (15)$$

In Eq. (15), $\tilde{n} = n + ik$ denotes the complex refractive index of the material. The measured n and k values for Si and Ag are taken from Green [57] and Yang [110], respectively. Figure 4.2 shows the schematic of the basic model and multiple reflections of a light beam from the cell.

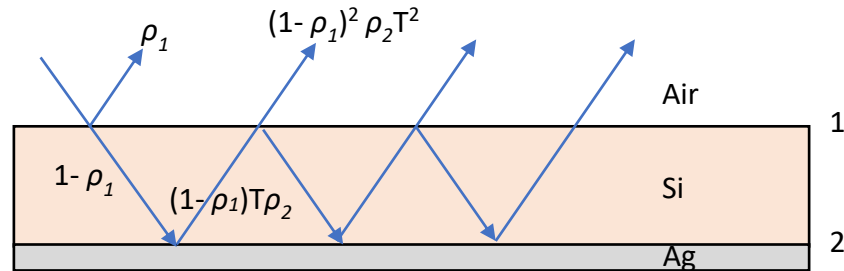


Figure 4.2. Reflection of light from a simple silicon cell

Since the thickness of the Si cell (300 μm) is much larger than the wavelength of interest ($\sim 1 \mu\text{m}$), the light can be assumed incoherent and multiple reflections can be calculated by ray-tracing. The amount of transmitted light (T) after it passes through length l is calculated by the Beer-Lambert law.

$$T = e^{-\frac{4\pi k l}{\lambda}} \quad (54)$$

where $l = 300 \mu\text{m}$. The reflectivities at the air-Si and Si-Ag interfaces are denoted as ρ_1 and ρ_2 respectively. The reflectivity of the Si cell can be calculated by adding up the subsequent reflections.

$$\rho_{total} = \rho_1 + (1 - \rho_1)^2 \rho_2 T^2 + (1 - \rho_1)^2 \rho_1 \rho_2^2 T^2 + (1 - \rho_1)^2 \rho_1^2 \rho_2^3 T^6 + \dots \quad (55)$$

In Eq. (55), multiple reflections form a geometric series which is sums up to;

$$\rho_{total} = \rho_1 + \frac{(1 - \rho_1)^2 \rho_2 T^2}{1 - \rho_1 \rho_2 T^2} \quad (56)$$

The Ag layer can be assumed opaque in the visible and IR region. Then, the absorption from the Si cell can be found by Kirchhoff's law:

$$\alpha = 1 - \rho_{total} \quad (57)$$

Based on Eqs. (56) and (57), the spectral reflection and absorption of Si cell model is plotted in Figure 4.3.

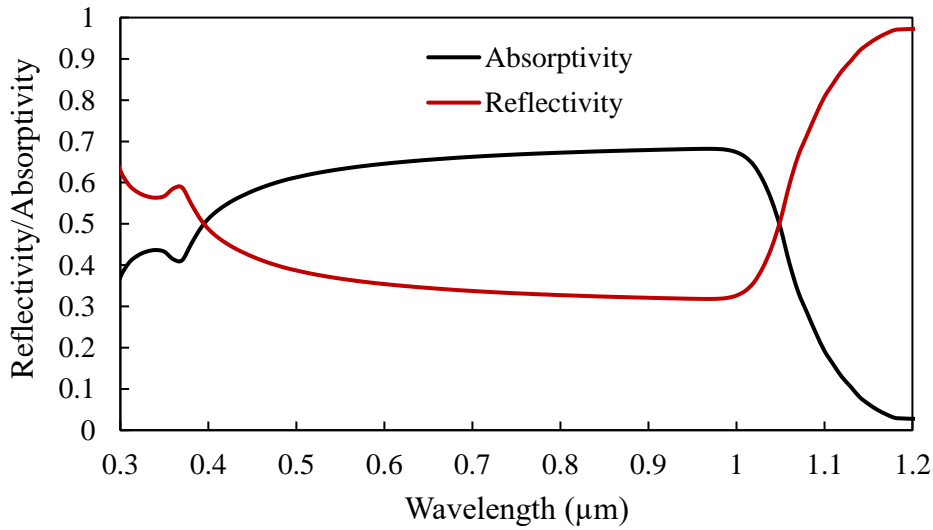


Figure 4.3. The reflectivity and absorptivity of 300 μm thick Si cell with Ag back reflector

On Figure 4.3., the absorptivity of a 300 μm thick Si cell reaches its maximum value of 68.2% at $\lambda = 0.97 \mu\text{m}$ and decreases towards the bandgap wavelength of 1.1 μm . The high reflectivity after 1 μm is due to the reflection from Ag. Considering Figure

4.3, a narrow band absorption peak can be obtained between 0.9-1.1 μm . For this purpose, the reflectivity on the air-Si interface should be minimized between 0.9-1.1 μm and should be close to the reflection of a flat Si cell for other wavelengths. This condition can be expressed in Eq. (58).

$$\rho_{\lambda}(\lambda) = \begin{cases} \approx 0, & \lambda \in [0.9 - 1.1] \mu\text{m} \\ \approx \rho_{Si,flat}, & \lambda \notin [0.9 - 1.1] \mu\text{m} \end{cases} \quad (58)$$

In a typical TPV emitter with attainable temperatures, radiation below wavelength 0.5 μm can be neglected. Also, Si absorbs poorly after its bandgap, therefore high reflectivity is not crucial after 1.1 μm . With these considerations, a *FOM* is defined in Eq. (59), which is aimed to be maximized. On the right-hand side, the first and second terms represent the high and low reflectivity regions, respectively. The upper wavelength of low reflectivity region is chosen as 0.8 μm to allow a smooth transition. With this equation, the reflectivity between 0.9-1.1 μm is to be minimized while keeping the reflection at other wavelengths as high as possible.

$$FOM = \frac{\int_{0.5}^{0.8} \rho_{\lambda}(\lambda) d\lambda}{\int_{0.5}^{0.8} d\lambda} - \frac{\int_{0.9}^{1.1} \rho_{\lambda}(\lambda) d\lambda}{\int_{0.9}^{1.1} d\lambda} \quad (59)$$

For optimization, parameter sweep method is combined with the FDTD method. For numerical simulations, a mesh convergence test showed 5 nm is sufficient for both 2D and 3D cases, and will be used throughout the rest of the Chapter.

4.2. Optimization of Two-Dimensional Nanostructures

Two-dimensional (2D) structures can be defined by geometric parameters in two dimensions. In the literature, they are sometimes called 1D gratings, since periodicity repeats in one dimension. The advantage of working with 2D structures is that their computational analysis requires much shorter simulation time than 3D structures. 2D simulations can be used to obtain a rough idea about the behavior of 3D nanostructures. In this chapter, three types of 2D nanostructures are investigated; triangular gratings, v-grooves and rectangular gratings. The nanostructures have three parameters: width (w), height or depth (h), and period (Λ). Figure 4.4. shows the schematic of the proposed structures and a sample unit cell.

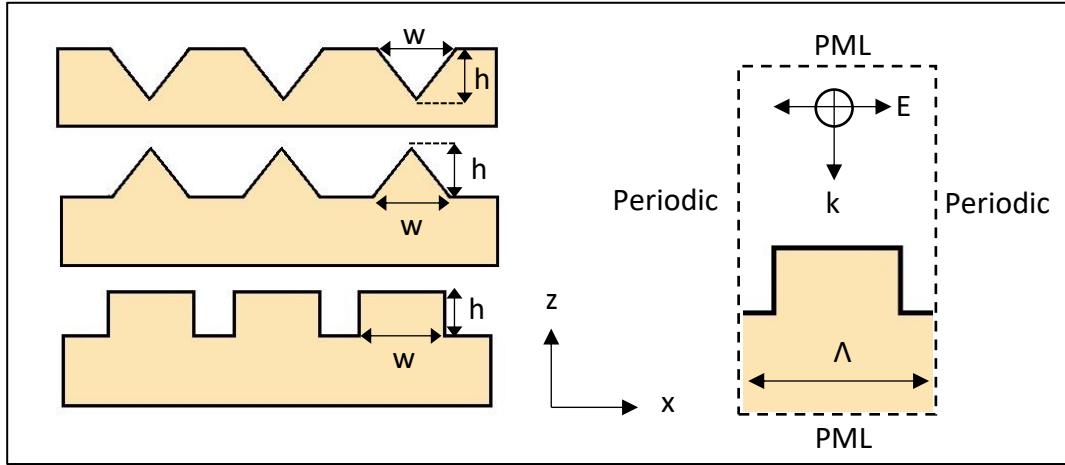


Figure 4.4. 2D silicon nanostructures and a sample unit cell

In FDTD simulations, the z boundary conditions are set to PML to prevent reflection from boundaries, while x boundary conditions are set to periodic. The light source is characterized as TM polarized plane wave incident normally to the surface.

Previous studies have shown that AR behavior of nanostructures is a strong function of its period [13, 17, 20, 84, 106]. For example, in [106], the triangular grooves with period of $1 \mu\text{m}$ showed minimum reflection around the wavelength $1 \mu\text{m}$, regardless of the groove angle. In rectangular gratings with the period of $0.65 \mu\text{m}$, sharp fall in reflectivity appeared around the wavelength of $0.65 \mu\text{m}$, regardless of the groove height. Since it is desired to reduce the reflectivity around $0.9 \mu\text{m}$ wavelength, the periodicity of the nanostructures is chosen as $0.9 \mu\text{m}$. To determine the optimum w and h , a parameter sweep optimization is employed with the aim of maximizing the FOM given in Eq. (59). In the optimization, the width and height of the gratings were varied with 50 nm increments. For rectangular gratings, the maximum allowed height is fixed to 350 nm to limit the area increase. A total number of 240 combinations have been studied. Table 4.1-4.3 show the FOM values for varying w and h for the triangular, v-groove and rectangular gratings, respectively.

Table 4.1. FOM values with varying height and width of triangular gratings

Height (nm)	Width (nm)										0.16
	450	500	550	600	650	700	750	800	850	900	
100	0.052	0.061	0.070	0.077	0.082	0.084	0.085	0.084	0.081	0.078	
150	0.072	0.089	0.104	0.114	0.122	0.127	0.128	0.127	0.123	0.118	
200	0.093	0.113	0.130	0.141	0.148	0.153	0.155	0.153	0.151	0.147	
250	0.106	0.121	0.135	0.143	0.148	0.151	0.152	0.154	0.154	0.154	
300	0.102	0.114	0.120	0.116	0.120	0.122	0.125	0.128	0.134	0.138	
350	0.086	0.088	0.085	0.081	0.080	0.078	0.087	0.093	0.101	0.109	
400	0.062	0.058	0.051	0.044	0.042	0.045	0.052	0.057	0.070	0.078	
450	0.042	0.034	0.026	0.020	0.020	0.024	0.031	0.039	0.047	0.050	
500	0.030	0.022	0.015	0.012	0.012	0.017	0.023	0.028	0.033	0.036	0.0

Table 4.2. FOM values with varying depth and width of v-groove gratings

Depth (nm)	Width (nm)										0.2
	350	400	450	500	550	600	650	700	750	800	
100	0.066	0.074	0.083	0.088	0.093	0.095	0.095	0.094	0.091	0.087	
150	0.108	0.125	0.138	0.147	0.152	0.153	0.152	0.147	0.141	0.133	
200	0.138	0.159	0.175	0.186	0.192	0.192	0.188	0.180	0.171	0.162	
250	0.141	0.163	0.180	0.190	0.196	0.195	0.189	0.179	0.169	0.161	
300	0.125	0.143	0.158	0.168	0.173	0.169	0.164	0.152	0.142	0.135	
350	0.102	0.116	0.127	0.135	0.138	0.136	0.128	0.113	0.107	0.100	
400	0.082	0.091	0.100	0.106	0.108	0.105	0.096	0.084	0.073	0.065	
450	0.072	0.078	0.082	0.086	0.087	0.082	0.073	0.061	0.050	0.045	
500	0.070	0.074	0.076	0.076	0.075	0.070	0.059	0.046	0.035	0.031	0.0

Table 4.3. FOM values with varying height and width of rectangular gratings

Height (nm)	Width (nm)										0.27
	300	350	400	450	500	550	600	650	700	750	
100	0.051	0.102	0.148	0.171	0.174	0.166	0.151	0.130	0.100	0.068	
150	0.133	0.198	0.248	0.261	0.251	0.229	0.207	0.177	0.139	0.101	
200	0.181	0.224	0.243	0.243	0.232	0.213	0.189	0.155	0.116	0.084	
250	0.172	0.189	0.190	0.192	0.192	0.177	0.149	0.116	0.083	0.065	
300	0.117	0.125	0.130	0.143	0.150	0.127	0.099	0.072	0.053	0.045	
350	0.040	0.049	0.072	0.096	0.105	0.072	0.048	0.029	0.022	0.022	0.0

From Tables 4.1-4.3, the performance of rectangular gratings was observed to be superior compared to triangular and v-groove gratings, based on the *FOM* defined in Eq. (59). It is worth noting that the *FOM* of rectangular gratings is much more sensitive to the changes in the height and width of the structure, compared to

triangular and v-groove gratings. The optimum parameters of the three types of nanostructures and the corresponding *FOM* values are presented in Table 4.4.

Table 4.4. Optimum parameters of three simple gratings

Grating	Λ (μm)	w (nm)	h (nm)	<i>FOM</i>
Triangular	0.9	750	200	0.155
V-Groove	0.9	550	250	0.196
Rectangular	0.9	450	150	0.261

The reflectivity spectra of Si with three optimized gratings, compared to flat Si are shown in Figure 4.5. All three optimized structures show a sharp decrease in reflectivity around 0.9 μm , which is due to the periodicity of the nanostructures. The triangular and v-groove gratings show very similar reflectivity spectra with v-groove having slightly lower average reflectivity. The rectangular gratings show a broader reflectivity dip compared to triangular and v-groove gratings. The absorptivity of the Si cell is found by inserting the reflectivity data presented in Figure 4.5 into Eqs. (56) and (57). The absorptivity spectra of the nanostructured Si cells compared to flat Si are shown Figure 4.6. In the figure, the wavelengths after 1.2 μm was not included due to negligible absorptivity of Si at this range.

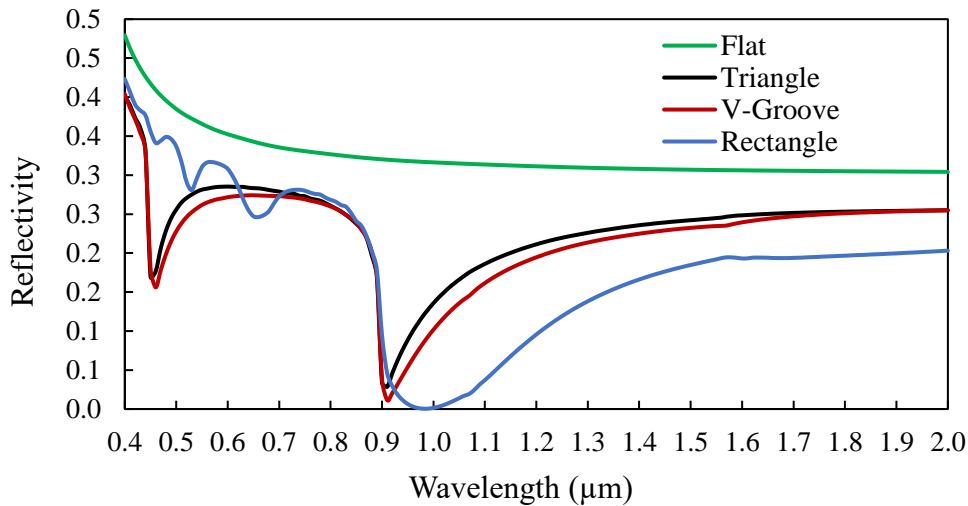


Figure 4.5. Reflectivity of Si with three optimized gratings

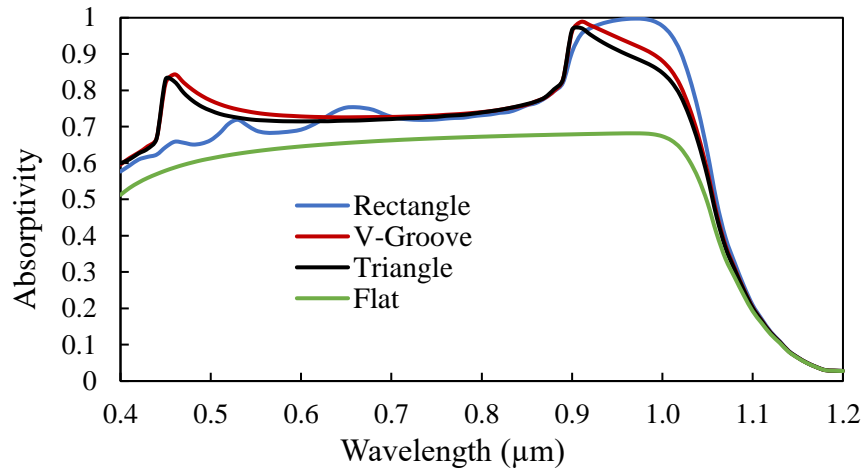


Figure 4.6. Absorptivity spectra of nanostructured Si cells compared to flat Si

4.3. Optimization of Three-Dimensional Nanostructures

In order to have low reflection in both TM and TE polarizations, the nanostructure should be symmetric with respect to both x and y axes. For 3D simulations, square based pyramids and nanopillars are investigated. The square nanopillar shape is referred as square for simplicity. Figure 4.7 shows the unit cells of square and pyramid nanostructures.

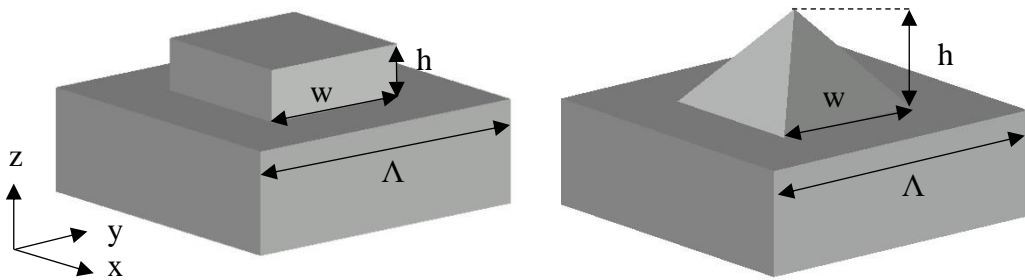


Figure 4.7. Unit cells of 3D Si nanostructures

In the 3D FDTD simulations, both x and y boundary conditions are set as periodic. Similar to 2D case, the optimizations are conducted with parameter sweep. Tables 4.5-4.6 show the FOM values for varying height and width of pyramid and square nanostructures. The optimum parameters of the pyramid and square nanostructures and the corresponding figures of merit are presented in Table 4.7.

Table 4.5. FOM values with varying pyramid height and width

Height (nm)	Width (nm)										0.17
	450	500	550	600	650	700	750	800	850	900	
200	0.046	0.058	0.070	0.081	0.091	0.097	0.100	0.101	0.098	0.092	0.0
250	0.060	0.077	0.094	0.108	0.119	0.127	0.131	0.130	0.126	0.119	
300	0.075	0.097	0.116	0.130	0.142	0.149	0.152	0.151	0.147	0.140	
350	0.089	0.112	0.130	0.143	0.153	0.158	0.161	0.159	0.155	0.150	
400	0.099	0.121	0.136	0.146	0.153	0.156	0.157	0.153	0.151	0.148	
450	0.105	0.123	0.135	0.141	0.144	0.144	0.141	0.138	0.137	0.136	
500	0.107	0.121	0.128	0.130	0.129	0.125	0.119	0.115	0.115	0.118	

Table 4.6. FOM values with varying square height and width

Height (nm)	Width (nm)								0.24
	250	300	350	400	450	500	550	600	
100	0.018	0.017	0.036	0.064	0.086	0.098	0.104	0.103	0.0
150	0.050	0.061	0.107	0.159	0.189	0.196	0.190	0.176	
200	0.099	0.130	0.181	0.224	0.236	0.225	0.208	0.181	
250	0.143	0.182	0.213	0.230	0.225	0.210	0.192	0.155	
300	0.168	0.184	0.193	0.199	0.194	0.178	0.160	0.113	
350	0.160	0.139	0.138	0.145	0.147	0.133	0.109	0.063	

Table 4.7. Optimum parameters of the pyramid and square nanostructures

Nanostructure	λ (μm)	w (nm)	h (nm)	FOM
Pyramid	0.9	750	350	0.161
Square	0.9	450	200	0.236

Figure 4.8 shows the reflection spectra of optimized square and pyramid structures compared to that of flat Si. In Figure 4.9, the absorptivity of Si cells with square and pyramid structures compared to that of flat Si cell are presented. The average absorptivity between 0.9-1.1 μm is found to be 57%, 76% and 79% for flat, pyramid and square structured Si cells, respectively.

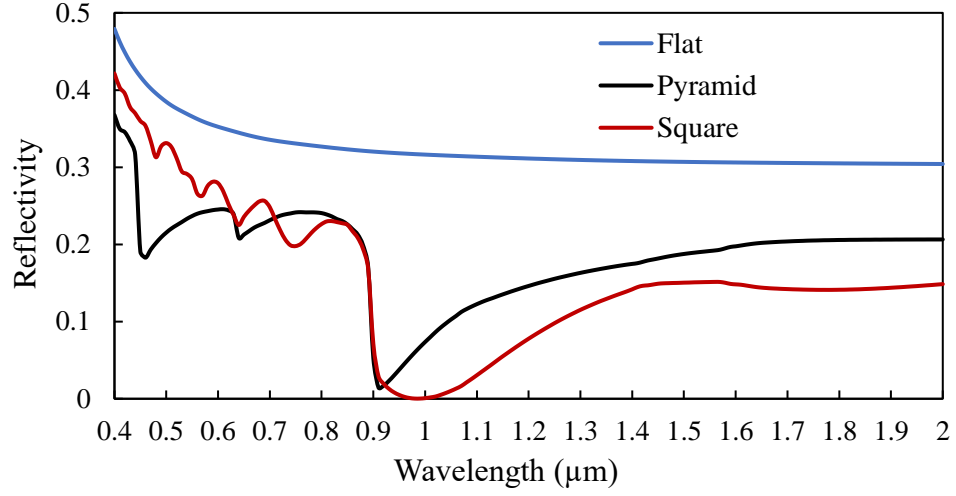


Figure 4.8. Reflectivity spectra of optimized square and pyramid structures

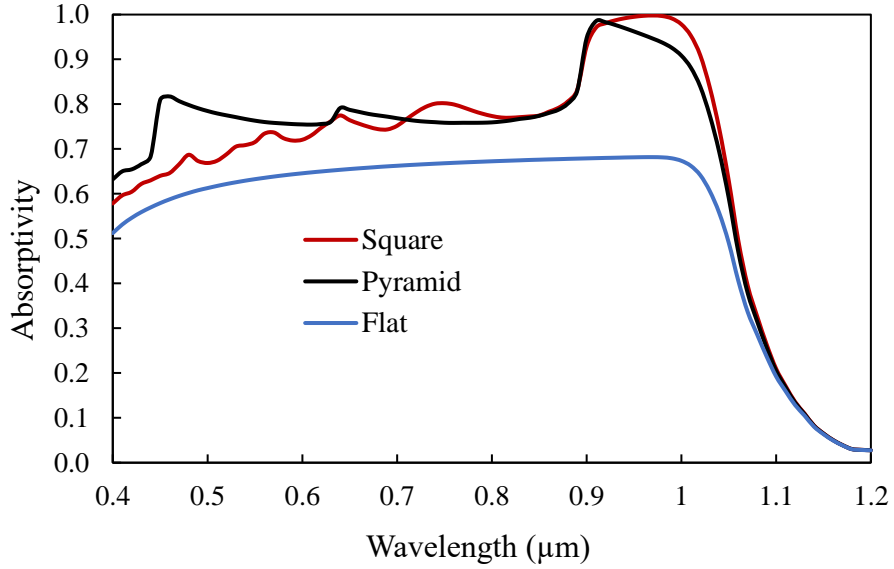


Figure 4.9. Absorptivity of Si cells with square and pyramid structures

4.4. Performance Evaluations

To evaluate the performance of the selective TPV cells, a blackbody emitter is considered. The absorbed in-band power (P_{abs}) is calculated by integrating the multiplication of the absorptivity of the cell and the in-band blackbody radiation:

$$P_{abs} = \int_0^{\lambda_g} \alpha_c(\lambda) E_{\lambda,b}(\lambda, T_E) d\lambda \quad (60)$$

The maximum amount of absorbed radiation that can be utilized to create electron-hole pairs (useful radiation) is given by $P_{el,max}$, with $\varepsilon_E = 1$:

$$P_{el,max} = \frac{1}{\lambda_g} \int_0^{\lambda_g} \alpha_c(\lambda) \varepsilon_E(\lambda) E_{\lambda,b}(\lambda, T_E) \lambda d\lambda \quad (38)$$

The difference between P_{abs} and $P_{el,max}$ gives the thermalization loss ($P_{thermal}$).

$$P_{thermal} = P_{abs} - P_{el,max} \quad (61)$$

The performance of designed Si cells can be compared to flat (polished) Si and the pyramid design of Sai [21]. In Sai, pyramids textures with $\lambda = w = 100$ nm and $h = 400$ nm showed reflection below 1% between 0.3-1.1 μm . Table 4.8 shows the absorbed radiation, usable radiation and the thermalization losses, for flat Si, pyramid design of Sai [21] and present pyramid and square designs. The emitter is assumed as a blackbody at 2000 K.

Table 4.8. Comparison of the absorbed radiation, useful radiation, and thermalization loss for Si cells matched with a blackbody emitter at 2000 K

Silicon Cell	Absorbed rad. (W cm ⁻²)	Useful rad. (W cm ⁻²)	Thermalization (W cm ⁻²)
Flat Si	5.487	4.493	0.994
Sai et. al. [21]	7.847	6.385	1.462
Pyramid	6.890	5.670	1.221
Square	7.098	5.861	1.237

It is seen that; compared to flat Si cell, the optimized pyramid and square structures increases the useful radiation by 26.2% and 30.4%, respectively. The amounts of increase in the thermalization are 22.8% and 24.4% for pyramid and square structured Si cells respectively. On the other hand, the pyramid structure of Sai [21] increases the useful radiation by 42.1% but also increases the thermalization by 47.1%. The square design increases useful radiation 24.56% more than it increases thermalization whereas the design of Sai [21] increases thermalization 11.9% more than increases useful radiation. It can be seen that, with narrowly absorbing square design, the cooling load due to thermalization can be lowered by 15.4% compared to the broadly absorbing design of Sai [21]. In conclusion, narrow band Si designs can be employed

in TPV systems instead of broadband Si solar cells to restrict thermalization in exchange for relatively lower power output. In addition to PV and TPV, the selective Si design presented in this chapter can find uses in light sensing and spectroscopy. For TPV and PV applications, the absorption enhancement should be polarization-independent, therefore 3D nanostructures are more desirable. On the other hand, 2D nanostructures can be preferred in light sensing applications if detection of polarization angle is required.

CHAPTER 5

CONCLUSIONS AND FUTURE WORK

5.1. Summary

Thermophotovoltaic devices require spectrally selective emitters and receivers in order to work efficiently. In an efficient TPV system, the emitter should mostly emit photons with energies higher than the bandgap of the TPV cell, and the cell should absorb strongly near its bandgap. However, naturally occurring materials rarely show spectral selectivity suitable for TPV systems. In this thesis the effect of nanostructures on thermal radiation and radiative properties is studied in order to propose high efficiency and power output designs for TPV systems. In order to attain spectral selectivity, nanostructured emitters and cells were designed by optimizing nanostructure parameters. In Chapter 3, selective emitter designs were proposed in order to work optimally with standard GaSb and Si TPV cells. The emitters are designed in such a way that it utilizes a metal-insulator-metal structure and further exhibits nanostructure induced novelties in their emissivity. In the first part of Chapter 3, MIM emitters with W base, SiO₂ dielectric layer and periodically spaced W resonator with shapes of disks, squares, cones and pyramids are designed to match GaSb cell. During the design of the MIM selective emitter, first, a *FOM* was designed to maximize the emissivity of emitter within the high external quantum efficiency region of the GaSb cell. By using this *FOM* with FDTD and the PSO algorithm, W-SiO₂-W emitters are optimized with four different resonator shapes. The optimized emitters were compared with each other, SiC emitter, blackbody and the ideal emitter, in terms of emitter efficiency, TPV system efficiency (simply referred as the efficiency) and electrical power output. In the second part of Chapter 3, a novel TPV emitter design is proposed with Ta base, HfO₂ dielectric layer, and periodically spaced Ta nanodisks. By using FDTD method and PSO algorithm, the emitter is optimized to have high emissivity matching the high quantum efficiency region of Si cell. For thermal stability at higher temperatures, a 25 nm HfO₂ coating is added to

the final design. The optimized emitter was compared to Yb_2O_3 , blackbody, and the ideal emitter. In Chapter 4, periodic nanostructures are optimized to increase the selective absorptivity of Si TPV cells, in order to increase useful absorption without cell heating. A simple Si cell was modeled as 300 μm thick crystalline Si slab with Ag back reflector. With FDTD and parameter sweep methods, 2D nanostructures (rectangular gratings, triangular gratings, and v-grooves) and 3D nanostructures (squares and pyramids) are optimized to have low reflectivity in a narrow band wavelength region that is close to the bandgap of Si. The performances of square and pyramid structured cells are compared to flat Si cell and a similar pyramid design from literature, in terms of absorbed, used, and thermalized radiation.

5.2. Conclusions

In this thesis, two MIM selective emitters and one nanostructured cell are optimized by adjusting nanostructure parameters. The promising numerical results are summarized in this paragraph. As presented in the first part of Chapter 3, TPV devices with the optimized W-SiO₂-W emitters paired with GaSb cells are estimated to have efficiencies between 19.95-22.73% and power outputs of 3.561-3.841 W cm^{-2} at 1700 K emitter temperature. It is observed with the *FOM* developed that efficient TPV systems with power outputs 91-98% that of blackbody emitter are possible. On average, between the MIM emitters with different resonator shapes, it is concluded that the disks do not have noticeable advantage over square ones, neither do cones over pyramids. However, MIM emitters with pointy resonators tend to have broader emissivity peaks compared to flat ones, which increases the power output, while causing a decrease in the efficiency. Among all the optimized W-SiO₂-W emitters, the highest efficiency (22.73%) was obtained with square resonators with the periodicity of 0.6 μm , which produces a power output of 3.622 W cm^{-2} when paired with GaSb cell. The designed emitter works 177% more efficiently and produces 9.7% more power than SiC emitter, which is frequently employed in TPV systems with GaSb cell. In the second part of Chapter 3, at the emitter temperature of 2000 K, the Ta-HfO₂-Ta emitter with thin film HfO₂ coating produces power output of 4.755 W cm^{-2} with an efficiency of 27.91% when paired with Si cell. The designed emitter is 53.3% more efficient and provides 87.4% more power than Yb_2O_3 emitter, which

is usually paired with Si cells. Development of selective emitters that has matching emissivity with Si cells is essential to utilizing Si based TPV systems, which are more economical and harmless compared to other TPV systems. In Chapter 4, the square nanostructures on Si cell showed better spectral selectivity than pyramids, however they are more sensitive to changes in the nanostructure parameters than the pyramid structures. When illuminated by a blackbody at 2000 K, the square structures increased useful radiation by 30.4% while limiting thermalization increase to 24.4%, compared to flat Si cell. In conclusion, it is seen that nanostructures can be used to create selective TPV emitters yielding both higher efficiency and power output than currently used emitters. In addition, TPV cells can be nanopatterned in such a way that power output can be increased without causing too much thermalization. The works in this thesis are expected to contribute to the development of efficient TPV systems.

5.3. Future Work

The studies presented in this thesis can be extended in several ways.

1. This thesis is based on numerical simulations. Experimental studies are necessary to test the predictions. For example, the designed TPV components can be fabricated and their optical properties measured. The fabricated TPV emitters can be bonded with readily available cells and operated at elevated temperatures to measure electrical power output and efficiency. Observing the effects of prolonged operation hours at high temperatures on the performance and mechanical stability of nanostructured TPV emitters would be essential to realization of practical TPV systems.
2. Throughout the thesis, TPV systems are assumed to work in the far field regime. Operating in the near field regime is expected to yield much higher power outputs than the far field regime. The effect of nanostructures on the performance TPV systems working in the near field regime can be studied.
3. Although different resonator shapes were optimized to obtain selective emissivity, the shape itself was not optimized. Shape optimizations subject to different constraints can be conducted.

REFERENCES

- [1] Y. Wang, H. Liu and J. Zhu, "Solar thermophotovoltaics: Progress, challenges, and opportunities," *APL Materials*, vol. 7, no. 8, 2019.
- [2] F. P. Incropera, A. S. Lavine, T. L. Bergman and D. P. DeWitt, *Fundamentals of heat and mass transfer*, Wiley, 2011.
- [3] S. Gasiorowicz, *Quantum Physics*, John Wiley and Sons, 2003.
- [4] M. F. Modest, *Radiative heat transfer*, Academic press, 2013.
- [5] "Industry Today," 5 November 2020. [Online]. Available: <https://industrytoday.com/wp-content/uploads/2020/11/electromagnetic-waves.jpg>. [Accessed 18 July 2021].
- [6] Z. M. Zhang, *Nano/microscale heat transfer*, Springer Nature Switzerland, 2020.
- [7] A. Taflove, S. C. Hagness and J. Simpson, "Introduction to Maxwell's equations and the Yee algorithm," in *Computational electrodynamics: the finite-difference time-domain method*, Artech house, 2005, pp. 51-105.
- [8] M. Fox, *Optical Properties of Solids*, 2 ed., Oxford University Press, 2010.
- [9] H. Wang and L. Wang, "Perfect selective metamaterial solar absorbers," *Optics express*, vol. 21, no. 106, pp. A1078-A1093, 2013.
- [10] D. G. Baranov, Y. Xiao, I. A. Nechepurenko, A. Krasnok, A. Alù and M. A. Kats, "Nanophotonic engineering of far-field thermal emitters," *Nature materials*, vol. 18, no. 9, pp. 920-930, 2019.
- [11] D. Chubb, *Fundamentals of thermophotovoltaic energy conversion*, Elsevier, 2007.

- [12] S. Adachi, *Optical Constants of Crystalline and Amorphous Semiconductors: Numerical Data and Graphical Information*, Springer Science & Business Media, 2013.
- [13] S. A. Boden and D. M. Bagnall, "Tunable reflection minima of nanostructured antireflective surfaces," *Applied Physics Letters*, vol. 93, 2008.
- [14] A. Deinega, I. Valuev, B. Potapkin and Y. Lozovik, "Minimizing light reflection from dielectric textured surfaces," *JOSA A*, vol. 28, no. 5, pp. 770-777, 2011.
- [15] T. Yagi, Y. Uraoka and T. Fuyuki, "Ray-trace simulation of light trapping in silicon solar cell with texture structures," *Solar Energy Materials & Solar Cells*, vol. 90, p. 2647–2656, 2006.
- [16] Y. Zhao, Y. Liua, Q. Chena, W. Chena, J. Wua, Y. Wang and X. Dua, "Broadband omnidirectional anti-reflection property of V-groove textured silicon," *Solar Energy*, vol. 193, pp. 132-138, 2019.
- [17] A. Heinzl, V. Boerner, A. Gombert, B. Bläsi, V. Wittwer and J. Luther, "Radiation filters and emitters for the NIR based on periodically structured metal surfaces," *Journal of Modern Optics*, vol. 47, no. 13, pp. 2399-2419, 2000.
- [18] H. Sai, H. Yugami, Y. Akiyama, Y. Kanamori and K. Hane, "Surface microstructured selective emitters for TPV systems," in *Conference Record of the Twenty-Eighth IEEE Photovoltaic Specialists Conference*, 2000.
- [19] H. Sai, Y. Kanamori and H. Yugami, "High-temperature resistive surface grating for spectral control of thermal radiation," *Applied Physics Letters*, vol. 82, no. 11, pp. 1685-1687, 2003.
- [20] H. Sai and H. Yugami, "Thermophotovoltaic generation with selective radiators based on tungsten surface gratings," *Appl. Phys. Lett.*, vol. 85, no. 16, 2004.

- [21] H. Sai, H. Fujii, K. Arafune, Y. Ohshita, M. Yamaguchi, Y. Kanamori and H. Yugami, "Antireflective subwavelength structures on crystalline Si fabricated using directly formed anodic porous alumina masks," *Applied physics letters*, vol. 88, no. 20, 2006.
- [22] Y. Chen and Z. Zhang, "Design of tungsten complex gratings for thermophotovoltaic radiators," *Optics communications*, vol. 269, no. 2, pp. 411-417, 2007.
- [23] I. Celanovic, N. Jovanovic and J. Kassakian, "Two-dimensional tungsten photonic crystals as selective thermal emitters," *Applied Physics Letters*, vol. 92, no. 15, 2008.
- [24] S. Bandiera, D. Jacob, T. Muller, F. Marquier, M. Laroche and J. J. Greffet, "Enhanced absorption by nanostructured silicon," *Applied Physics Letters*, vol. 93, no. 19, 2008.
- [25] A. Mavrokefalos, S. E. Han, S. Yerci, M. S. Branham and G. Chen, "Efficient Light Trapping in Inverted Nanopyramid Thin Crystalline Silicon Membranes for Solar Cell Applications," *Nano Letters*, no. 12, pp. 2792-2796, 2012.
- [26] N. Nguyen-Huu, Y.-B. Chen and Y.-L. Lo, "Development of a polarization-insensitive thermophotovoltaic emitter with a binary grating," *Optics express*, vol. 20, no. 6, pp. 5882-5890, 2012.
- [27] C. Arnold, F. Marquier, M. Garin, F. Pardo, S. Collin, N. Bardou, J.-L. Pelouard and J.-J. Greffet, "Coherent thermal infrared emission by two-dimensional silicon carbide gratings," *Physical Review B*, vol. 86, 2012.
- [28] V. Rinnerbauer, Y. X. Yeng, W. R. Chan, J. J. Senkevich, J. D. Joannopoulos, M. Soljačić and I. Celanovic, "High-temperature stability and selective thermal emission of polycrystalline tantalum photonic crystals," *Optics express*, vol. 21, no. 9, 2013.

- [29] B. Zhao, J. M. Zhao and Z. M. Zhang, "Enhancement of near-infrared absorption in graphene with metal gratings," *Applied Physics Letters*, vol. 105, no. 3, 2014.
- [30] A. Yüksel, A. Heltzel and J. R. Howell, "Design and optimization of thermal selective emitters for high-efficiency thermophotovoltaic (TPV) power generation," in *Proceedings of the ASME 2015 9th International Conference on Energy Sustainability*, San Diego, 2015.
- [31] R. H. Siddique, Y. J. Donie, G. Gomard, S. Yalamanchili, T. Merdzhanova, U. Lemmer and H. Hölscher, "Bioinspired phase-separated disordered nanostructures for thin photovoltaic absorbers," *Science Advances*, no. 3, 2017.
- [32] B. J. Lee, L. P. Wang and Z. M. Zhang, "Coherent thermal emission by excitation of magnetic polaritons between periodic strips and a metallic film," *Optics Express*, vol. 16, no. 15, pp. 11328-11336, 2008.
- [33] K. Aydin, V. E. Ferry, R. M. Briggs and H. A. Atwater, "Broadband polarization-independent resonant light absorption using ultrathin plasmonic super absorbers," *Nature communications*, vol. 2, no. 1, pp. 1-7, 2011.
- [34] L. P. Wang and Z. M. Zhang, "Wavelength-selective and diffuse emitter enhanced by magnetic polaritons for thermophotovoltaics," *Applied Physics Letters*, vol. 100, no. 6, p. 063902, 2012.
- [35] B. Zhao, L. Wang, Y. Shuai and Z. M. Zhang, "Thermophotovoltaic emitters based on a two-dimensional grating/thin-film nanostructure," *International Journal of Heat and Mass Transfer*, no. 67, pp. 637-645, 2013.
- [36] D. Woolf, J. Hensley, J. G. Cederberg, D. T. Bethke, A. D. Grine and E. A. Shaner, "Heterogeneous metasurface for high temperature selective emission," *Applied Physics Letters*, vol. 105, no. 8, p. 081110, 2014.

- [37] J. Song, H. Wu, Q. Cheng and J. Zhao, "1D trilayer films grating with W/SiO₂/W structure as a wavelength-selective emitter for thermophotovoltaic applications," *Journal of Quantitative Spectroscopy and Radiative Transfer*, no. 158, pp. 136-144, 2015.
- [38] C. Shemelya, D. DeMeo, N. P. Latham, X. Wu, C. Bingham, W. Padilla and T. E. Vandervelde, "Stable high temperature metamaterial emitters for thermophotovoltaic applications," *Applied Physics Letters*, vol. 104, no. 20, 2014.
- [39] H. Wang, V. P. Sivan, A. Mitchell, G. Rosengarten, P. Phelan and L. Wang, "Highly efficient selective metamaterial absorber for high-temperature solar thermal energy harvesting," *Solar Energy Materials and Solar Cells*, no. 137, pp. 235-242, 2015.
- [40] F. Ding, J. Dai, Y. Chen, J. Zhu, Y. Jin and S. I. Bozhevolnyi, "Broadband near-infrared metamaterial absorbers utilizing highly lossy metals," *Scientific reports*, vol. 6, no. 1, pp. 1-9, 2016.
- [41] T. Yokoyama, T. D. Dao, K. Chen, S. Ishii, R. P. Sugavaneshwar, M. Kitajima and T. Nagao, "Spectrally selective mid-infrared thermal emission from molybdenum plasmonic metamaterial operated up to 1000° C," *Advanced Optical Materials*, vol. 4, no. 12, pp. 1987-1992, 2016.
- [42] X. Han, K. He, Z. He and Z. Zhang, "Tungsten-based highly selective solar absorber using simple nanodisk array," *Optics express*, vol. 25, no. 24, pp. A1072-A1078, 2017.
- [43] Y. Matsuno and A. Sakurai, "Perfect infrared absorber and emitter based on a large-area metasurface," *Optical Materials Express*, vol. 7, no. 2, pp. 618-626, 2017.
- [44] G. Silva-Oelker, C. Jerez-Hanckes and P. Fay, "High-temperature tungsten-hafnia optimized selective thermal emitters for thermophotovoltaic

- applications," *Journal of Quantitative Spectroscopy and Radiative Transfer*, vol. 231, pp. 61-68, 2019.
- [45] M. Chen and Y. He, "Plasmonic nanostructures for broadband solar absorption based on the intrinsic absorption of metals," *Solar Energy Materials and Solar Cells*, vol. 188, pp. 156-163, 2018.
- [46] A. Sakurai and Y. Matsuno, "Design and fabrication of a wavelength-selective near-infrared metasurface emitter for a thermophotovoltaic system," *Micromachines*, vol. 10, no. 2, p. 157, 2019.
- [47] Y. Khorrami and D. Fathi, "Broadband thermophotovoltaic emitter using magnetic polaritons based on optimized one-and two-dimensional multilayer structures," *JOSA B*, vol. 36, no. 3, pp. 662-666, 2019.
- [48] P. Zheng, K. Sujan and W. Nianqiang, "Converting plasmonic light scattering to confined light absorption and creating plexcitons by coupling a gold nano-pyramid array onto a silica-gold film," *Nanoscale horizons*, vol. 4, no. 2, pp. 516-525, 2019.
- [49] K. Isobe and K. Hanamura, "Selective absorption of a thermophotovoltaic cell using a thin semiconductor and a top fishnet-structured electrode," *International Journal of Heat and Mass Transfer*, no. 134, pp. 807-814, 2019.
- [50] P. T. Dang, "Efficient broadband truncated-pyramid-based metamaterial absorber in the visible and near-infrared regions," *Crystals*, vol. 10, no. 9, p. 784, 2020.
- [51] K. Yee, "Numerical solution of initial boundary value problems involving Maxwell's equations in isotropic media," *IEEE Transactions on antennas and propagation*, vol. 14, no. 3, pp. 302-307, 1966.
- [52] Y. Xuan, "An overview of micro/nanoscaled thermal radiation," *Photonics and Nanostructures-Fundamentals and Applications*, vol. 12, no. 2, pp. 93-113, 2014.

- [53] R. C. Rumpf, "Review of electromagnetics and introduction to FDTD," 2 November 2020. [Online]. Available: <https://empossible.net/wp-content/uploads/2020/01/Lecture-Electromagnetics-FDTD.pdf>. [Accessed 18 July 2021].
- [54] W. W. Zhang, H. Qi, Y. M. Yin and Y. T. Ren, "Tailoring radiative properties of a complex trapezoidal grating solar absorber by coupling between SPP and multi-order MP for solar energy harvesting," *Optics Communications*, no. 479, 2021.
- [55] A. Didari and M. P. Mengüç, "Near-field thermal emission between corrugated surfaces separated by nano-gaps," *Journal of Quantitative Spectroscopy and Radiative Transfer*, no. 158, pp. 43-51, 2015.
- [56] A. Sakurai, B. Zhao and Z. M. Zhang, "Resonant frequency and bandwidth of metamaterial emitters and absorbers predicted by an RLC circuit model," *Journal of Quantitative Spectroscopy and Radiative Transfer*, vol. 149, pp. 33-40, 2014.
- [57] M. A. Green, "Self-consistent optical parameters of intrinsic silicon at 300 K including temperature coefficients," *Solar Energy Materials and Solar Cells*, vol. 92, no. 11, pp. 1305-1310, 2008.
- [58] E. D. Palik, Handbook of optical constants of solids, Academic press, 1998.
- [59] J. H. Kim, S. M. Jung and M. W. Shin, "High-temperature degradation of one-dimensional metallodielectric (W/SiO₂) photonic crystal as selective thermal emitter for thermophotovoltaic system," *Optical Materials*, no. 72, pp. 45-51, 2017.
- [60] A. R. Conn, K. Scheinberg and L. N. Vicente, Introduction to derivative-free optimization, Society for Industrial and Applied Mathematics, 2009.
- [61] J. Kennedy and R. Eberhart, "Particle swarm optimization," in *Proceedings of ICNN'95-international conference on neural networks. Vol. 4. IEEE*, 1995.

- [62] Y. Shi and R. Eberhart, "A modified particle swarm optimizer," in *IEEE international conference on evolutionary computation proceedings. IEEE world congress on computational intelligence (Cat. No. 98TH8360)*, 1998.
- [63] J. Robinson and Y. Rahmat-Samii, "Particle swarm optimization in electromagnetics," *IEEE transactions on antennas and propagation*, vol. 52, no. 2, pp. 397-407, 2004.
- [64] L. M. Fraas, J. E. Avery, H. X. Huang and R. U. Martinelli, "Thermophotovoltaic system configurations and spectral control," *Semiconductor Science and Technology*, vol. 18, no. 5, p. S165, 2003.
- [65] Q. Cai, P. Chen, S. Cao, Q. Ye and X. Wu, "Performance Analysis of GaSb Cell and Thermophotovoltaic System Under Near-Field Thermal Radiation.," *International Journal of Thermophysics* , vol. 41, no. 12, pp. 1-15, 2020.
- [66] P. A. Iles, C. Chu and E. Linder, "The influence of bandgap on TPV converter efficiency," *AIP Conference Proceedings*, vol. 358, no. 1, pp. 446-457, February 1996.
- [67] L. M. Fraas, J. E. Avery, P. E. Gruenbaum, V. S. Sundaram, K. Emery and R. Matson, "Fundamental characterization studies of GaSb solar cells," in *The Conference Record of the Twenty-Second IEEE Photovoltaic Specialists Conference-1991*, 1991.
- [68] K. Qiu, A. C. S. Hayden, M. G. Mauk and O. V. Sulima, "Generation of electricity using InGaAsSb and GaSb TPV cells in combustion-driven radiant sources," *Solar energy materials and solar cells*, vol. 90, no. 1, pp. 68-81, 2006.
- [69] L. Hu, A. Narayanaswamy, X. Chen and G. Chen, "Near-field thermal radiation between two closely spaced glass plates exceeding Planck's blackbody radiation law," *Applied Physics Letters*, vol. 92, no. 13, 2008.

- [70] L. M. Fraas, J. E. Avery and T. Nakamura, "Electricity from concentrated solar IR in solar lighting applications," in *Twenty-Ninth IEEE Photovoltaic Specialists Conference*, 2002.
- [71] J. J. Loferski, "Theoretical considerations governing the choice of the optimum semiconductor for photovoltaic solar energy conversion," *Journal of Applied Physics*, vol. 27, no. 7, pp. 777-784, 1956.
- [72] The National Renewable Energy Laboratory (NREL), "Reference Air Mass 1.5 Spectra," [Online]. Available: <https://www.nrel.gov/grid/solar-resource/spectra-am1.5.html>. [Accessed 24 June 2021].
- [73] J. Zhao, A. Wang, F. Yun, G. Zhang, D. M. Roche, S. R. Wenham and M. A. Green, "20 000 PERL silicon cells for the '1996 World Solar Challenge' solar car race," *Progress in Photovoltaics: Research and Applications*, vol. 5, no. 4, pp. 269-276, 1997.
- [74] E. E. Atak, E. B. Elçioğlu and T. Okutucu-Özyurt, "Nanostructured silicon design for effectively capturing infrared radiation for near-field TPV applications," in *NanoRad 2020*, Shanghai, 2022.
- [75] A. Sakurai, B. Zhao and Z. M. Zhang, "Effect of polarization on dual-band infrared metamaterial emitters or absorbers," *Journal of Quantitative Spectroscopy and Radiative Transfer*, no. 158, pp. 111-118, 2015.
- [76] E. E. Atak, E. B. Elçioğlu and T. Okutucu-Özyurt, "Tantalum-Hafnia based metal-insulator-metal selective thermophotovoltaic emitter design (work in progress)," 2021.
- [77] J. Song, M. Si, Q. Cheng and Z. Luo, "Two-dimensional trilayer grating with a metal/insulator/metal structure as a thermophotovoltaic emitter," *Applied optics*, vol. 55, no. 6, pp. 1284-1290, 2016.

- [78] E. E. Atak, E. B. Elçioğlu and T. Okutucu-Özyurt, "Numerical design and optimization of a Tungsten-Silicon Dioxide-Tungsten selective emitter matching GaSb thermophotovoltaic cell (work in progress)," 2021.
- [79] S. Han, J. Shin, P. Jung, H. Lee and B. J. Lee, "Broadband Solar Thermal Absorber Based on Optical Metamaterials for High-Temperature Applications," *Advanced Optical Materials*, vol. 4, no. 8, pp. 1265-1273, 2016.
- [80] C. Ferrari, F. Melino, M. Pinelli, P. R. Spina and M. Venturini, "Overview and status of thermophotovoltaic systems," *Energy Procedia*, vol. 45, pp. 160-169, 2014.
- [81] E. E. Atak, E. B. Elçioğlu and T. Okutucu-Özyurt, "Metal-Insulator-Metal selective emitter design with an emissivity matching with Gasb thermophotovoltaic cell," in *ICHMT International Symposium on Advances in Computational Heat Transfer*, Rio de Janeiro, 2021.
- [82] Y. S. Touloukian and D. P. DeWitt, Thermophysical properties of matter-the tprc data series. volume 7. thermal radiative properties-metallic elements and alloys, New York: Springer, 1970.
- [83] S. Roberts, "Optical properties of nickel and tungsten and their interpretation according to Drude's formula," *Physical Review*, vol. 114, no. 1, p. 104, 1959.
- [84] H. Sai, H. Yugami, Y. Akiyama, Y. Kanamori and K. Hane, "Spectral control of thermal emission by periodic microstructured surfaces in the near-infrared region," *Journal of the Optical Society of America A*, vol. 18, no. 7, pp. 1472-1476, 2001.
- [85] H. Daneshvar, R. Prinja and N. P. Kherani, "Thermophotovoltaics: Fundamentals, challenges and prospects," *Applied Energy*, vol. 159, pp. 560-575, 2015.

- [86] L. M. Fraas, J. E. Avery and H. X. Huang, "Thermophotovoltaic furnace–generator for the home using low bandgap GaSb cells," *Semiconductor Science and Technology*, vol. 18, no. 5, 2003.
- [87] V. Stelmakh, W. R. Chan, M. Ghebrebrhan, J. Senkevich, J. D. Joannopoulos, M. Soljačić and I. Celanović, "Sputtered tantalum photonic crystal coatings for high-temperature energy conversion applications," *IEEE Transactions on Nanotechnology*, vol. 15, no. 2, pp. 303-309, 2016.
- [88] S. Kar, High permittivity gate dielectric materials (Vol. 43), Heidelberg: Springer, 2013.
- [89] Y. S. Touloukian, R. K. Kirby, R. E. Taylor and P. D. Desai, Thermophysical properties of matter-the tprc data series. volume 12. thermal expansion metallic elements and alloys, 1975.
- [90] P. N. Dyachenko, S. Molesky, A. Y. Petrov, M. Störmer, T. Krekeler, S. Lang, M. Ritter, Z. Jacob and & M. Eich, "Controlling thermal emission with refractory epsilon-near-zero metamaterials via topological transitions," *Nature communications*, vol. 7, no. 1, pp. 1-8, 2016.
- [91] J. Wang, Y. Chen, X. Chen, J. Hao, M. Yan and M. & Qiu, "Photothermal reshaping of gold nanoparticles in a plasmonic absorber," *Optics express*, vol. 19, no. 15, pp. 14726-14734, 2011.
- [92] M. F. Al-Kuhaili, "Optical properties of hafnium oxide thin films and their application in energy-efficient windows," *Optical Materials*, vol. 27, no. 3, pp. 383-387, 2004.
- [93] M. A. Green, K. Emery, Y. Hishikawa and W. Warta, "Solar cell efficiency tables (version 36)," *Progress in photovoltaics: research and applications* , vol. 18, no. 5, pp. 346-352, 2010.

- [94] J. Song, S. Huang, Y. Ma, Q. Cheng, R. Hu and X. Luo, "Radiative metasurface for thermal camouflage, illusion and messaging," *Optics express*, vol. 28, no. 2, pp. 875-885, 2020.
- [95] C. Schlemmer, J. Aschaber, V. Boerner and J. Luther, "Thermal stability of micro-structured selective tungsten emitters," *AIP Conference Proceedings*, vol. 653, no. 1, pp. 164-173, 2003.
- [96] K. A. Arpin, M. D. Losego and P. V. & Braun, "Electrodeposited 3D tungsten photonic crystals with enhanced thermal stability," *Chemistry of Materials*, vol. 23, no. 21, pp. 4783-4788, 2011.
- [97] B. Bitnar, W. Durisch and R. Holzner, "Thermophotovoltaics on the move to applications," *Applied Energy*, vol. 105, pp. 430-438, 2013.
- [98] Y. Han, X. Yu, D. Wang and D. Yang, "Formation of various pyramidal structures on monocrystalline silicon surface and their influence on the solar cells," *Journal of Nanomaterials*, 2013.
- [99] S. Mokkaapati and K. R. Catchpole, "Nanophotonic light trapping in solar cells," *Journal of applied physics*, vol. 112, no. 10, 2012.
- [100] D. Z. Dimitrov and C. H. Du, "Crystalline silicon solar cells with micro/nano texture," *Applied Surface Science*, vol. 266, pp. 1-4, 2013.
- [101] S. E. Han and G. Chen, "Optical Absorption Enhancement in Silicon," *Nano Letters*, no. 10, pp. 1012-1015, 2010.
- [102] L. Hu and G. Chen, "Analysis of Optical Absorption in Silicon Nanowire Arrays for Photovoltaic Applications," *Nano Letters*, vol. 7, no. 11, pp. 3249-3252, 2007.
- [103] H. Sai, Y. Kanamori, K. Arafune, Y. Ohshita and M. Yamaguchi, "Light Trapping Effect of Submicron Surface Textures in Crystalline Si Solar Cells," *Prog. Photovolt: Res. Appl.*, vol. 15, pp. 415-423, 2007.

- [104] L. Escoubas, J. Simon, M. Loli, G. Berginc, F. Flory and H. Giovannini, "An antireflective silicon grating working in the resonance domain for the near infrared spectral region," *Optics Communications*, no. 226, pp. 81-88, 2003.
- [105] Y. Kanamoria, K. Hane, H. Sai and H. Yugami, "100 nm period silicon antireflection structures fabricated using a porous alumina membrane mask," *Applied Physics Letters*, vol. 78, no. 2, pp. 142-143, 2001.
- [106] A. A. Abouelsaood, S. A. El-Naggar and M. Y. Ghannam, "Shape and size dependence of the anti-reflective and light-trapping action of periodic grooves," *Progress in Photovoltaics: Research and Applications*, vol. 10, no. 8, pp. 513-526, 2002.
- [107] S. Bandiera, D. Jacob, T. Muller, F. Marquier, M. Laroche and J.-J. Greffet, "Enhanced absorption by nanostructured silicon," *Appl. Phys. Lett.*, vol. 93, 2008.
- [108] S. H. Zaidi, A.-S. Chu and S. R. J. Brueck, "Optical properties of nanoscale, one-dimensional silicon grating structures," *J. Appl. Phys.*, vol. 80, no. 12, pp. 6997-7008, 1996.
- [109] E. Garnett and P. Yang, "Light Trapping in Silicon Nanowire Solar Cells," *Nano Letters*, vol. 10, pp. 1082-1087, 2010.
- [110] H. U. Yang, J. D'Archangel, M. L. Sundheimer, E. Tucker, G. D. Boreman and M. B. Raschke, "Optical dielectric function of silver," *Physical Review B*, vol. 91, no. 23, 2015.
- [111] G. Palfinger, B. Bitnar, W. Durisch, J. C. Mayor, D. Grützmacher and J. Gobrecht, "Cost estimates of electricity from a TPV residential heating system," in *AIP Conference Proceedings*, 2003.
- [112] A. Gombert, "An overview of TPV emitter technologies," *AIP conference proceedings*, vol. 653, no. 1, pp. 123-131, 2003.

APPENDICES

A. Optical Constants of Tungsten (W) at Elevated Temperatures

The optical constants of W at high temperatures were estimated with the model presented by Roberts [83]. The Drude model is given in Eq. (62) with the convention $\tilde{\epsilon}_r = \epsilon_1 - i\epsilon_2$. The parameters used in the model for 1100 K, 1600 K, and 2000 K are presented in Table A.1. In Eq. (62), the unit of wavelengths is μm .

$$\tilde{\epsilon} = 1 + \sum_m \frac{K_{0m}\lambda^2}{\lambda^2 - \lambda_{sm}^2 + i\delta_m\lambda_{sm}\lambda} - \frac{\lambda^2}{2\pi c\epsilon_0} \sum_n \frac{\sigma_n}{\lambda_{rn} - i\lambda} \quad (62)$$

Table A.1. The parameters used in Eq. (62) to estimate dielectric constants at elevated temperatures

T (K)	1100	1600	2000
σ_1	3.5	2.14	1.58
σ_2	0.16	0.19	0.22
λ_{r1}	9.3	6.0	4.63
λ_{r2}	0.36	0.36	0.36
K_{01}	10.9	10.9	10.9
K_{02}	13.4	13.4	13.4
K_{03}	12.0	12.0	12.0
λ_{s1}	1.40	1.40	1.40
λ_{s2}	0.57	0.57	0.57
λ_{s3}	0.25	0.25	0.25
δ_1	1.0	1.0	1.0
δ_2	1.2	1.2	1.2
δ_3	1.0	1.0	1.0

B. Spectral Emissivity of Ytterbia (Yb_2O_3)

The emissivity spectrum between 0.6-1.4 μm is taken from Bitnar [97]. The emissivity from 1.4 to 8 μm were calculated by dividing the spectral emissive power of Yb_2O_3 at 1735 K to blackbody emissive power at the same temperature based on the data presented in Gombert [112] which is cited to be obtained via a private communication with Bitnar. Figure B.1. shows the emissivity of Yb_2O_3 . The peaks around 2.76 μm and 4.43 μm were reported to be due to flames [97].

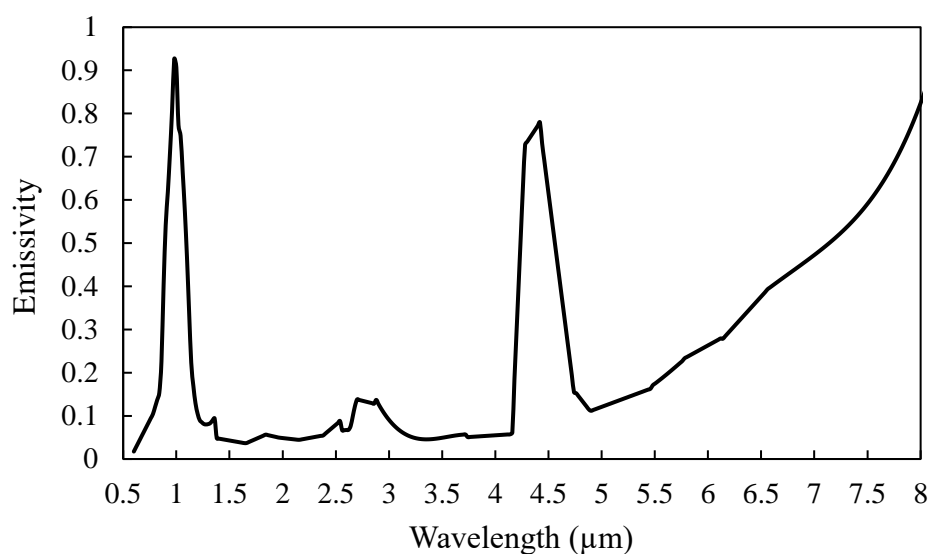


Figure B.1. Spectral emissivity of Yb_2O_3 mantle